Applications of Susceptibility-Based Brain Imaging using 7T MRI

Mobeen Ali, M.Sci
Sir Peter Mansfield Imaging Centre
School of Physics and Astronomy

Thesis submitted to the University of Nottingham for the degree of Doctor of Philosophy

August 24, 2018

Abstract

MRI is a powerful non-invasive technique for imaging soft tissues and for providing information on chemical composition. In this thesis, the effects of magnetic susceptibility from iron contained in ferritin and haemoglobin, and of myelinated tissue were studied. These effects were measured using a range of imaging techniques, including susceptibility weighted imaging (SWI) and quantitative susceptibility mapping (QSM).

Initially, simulations of static and defusing spins were performed to gain an understanding of the behaviour of different systems, which agreed well with comparison to the results from analytical models. For dipoles randomly placed in a spherical volume and in the x-y plane, the R_2* and $\Delta\omega$ values were approximately constant, but increased for dipoles restricted to a line parallel to the z axis and decreased for dipoles in a line in the x-y plane. The fitting of the phase variation of a simulated cylinder was then used to calculate the susceptibility values of a ferritin-doped cylindrical agar phantom, which correlated well between 3T and 7T, and increased with iron concentration.

Post-mortem imaging allows MR parameters to be studied in greater detail than in vivo imaging, but it is also confounded by fixation and storage conditions. An experimental setup was assembled to allow temperature-controlled scanning of a post-mortem brain. The R_1, R_2* and susceptibility values all decreased with increasing temperature, due to the reduction in the susceptibility of iron dominating the effect of the increased rate of diffusion of water. This was similar for a ferritin-doped cylindrical agar phantom, but the R_2* values increased, due to the uniformity of agar. A longitudinal imaging study of the post-mortem brain was performed with respect to fixation time. The volume of the tissue decreased. The R_2* and susceptibility values decreased and the R_1 values increased overall, but were also dependent on the location and depth within the tissue.

The thalamus relays information between different areas of the brain. In 1.5T and 3T MRI, the contrast between the thalamic nuclei is limited, thus motivating an evaluation of 7T post-mortem and in vivo MR imaging. A range of imaging sequences were optimised and the thalamic nuclei were manually delineated in the histology and corresponding post-mortem MR images, with a high degree of confidence, with reference to the Morel atlas. These were corroborated with the use of k-means clustering, Canny edge detection and hierarchical clustering. The nuclei in the in vivo images were also delineated with a reasonable degree of confidence, by comparing the boundaries across a range of imaging contrasts. For the groupings obtained from hierarchical clustering, the QSM clusters allowed the most nuclei to be identified on average, followed by the combined FLASH (fast low angle shot) magnitude and QSM clusters.

The brain has a high level of metabolic activity, which requires a significant supply of blood. Disruption to this can result in the loss of function, as cerebrovascular diseases. The cerebral blood vessels were imaged with optimised gradient echo and time of flight sequences, to calculate venous and arterial maps, overlap maps and a venous atlas. The distribution of vessels between subjects was similar, with little overlap between the venous and arterial maps. The venous atlas detailed the deep grey matter vessels better than the manually segmented Ward atlas. Finally, oximetry measurements were inferred from the susceptibility values, which were higher within grey matter compared to white matter, and were observed to increase up to a vein radius of 1mm and then decreased.

Acknowledgements

I would like to thank my supervisors, Professor Penny Gowland and Professor Richard Bowtell, all of my friends at the Sir Peter Mansfield Imaging Centre and my family, for their continuous support in helping me reach this milestone. I would also like to acknowledge the Medical Research Council for providing funding to enable these research project to be undertaken, the technical support from Alan Dorkes in building the phantoms and circulator, and the skills and expertise of Ian Scott and Denise Watson for obtaining and examining the post-mortem tissue samples.

Contents

Chapter 1

Introduction

1.1 Introduction

In magnetic resonance imaging (MRI), varies tissues and objects interact with the magnetic field. Large differences in magnetic susceptibility between air-tissue interfaces or around metallic implants can cause significant artefacts, as distortions or signal voids [1]. However, this effect can be exploited to measured subtle changes from a variety of biological sources of susceptibility, such as haeme, non-haeme iron and myelin [2]. Susceptibility effects are proportional to field strength, resulting in enhanced contrast in MRI [3], thus ultra-high field (7T) MRI is well suited for the projects in this thesis. The effects of susceptibility on imaging are explored and exploited to provide additional contrast and quantitative information in the brain. The iron in haemoglobin is used to map the cerebral blood vessels and calculate oxygen fractions. The leaching of non-haeme iron from ferritin in post-mortem tissue during fixation, and its temperature dependent susceptibility are investigated to assess the correlation of quantitative post-mortem MRI with in vivo values. The contrast from the myelin in the thalamus is used to delineate the thalamic nuclei manually and automatically, in histology, post-mortem and in vivo MRI. Therefore, the vascular, iron-deposition and thalamic components of neurodegenerative diseases could be better understood and pursued.

1.1.1 Role of iron in the brain

Iron is an essential element in the biology of nearly all living systems [4]. It is involved in many vital processes such as oxygen transport and respiration. The brain in particular is very metabolically active so iron has a large influence on its ability to function properly. Iron is known to accumulate in the brain with age, from many studies [5]. High iron levels are linked to many neurodegenerative diseases such as Alzheimer's disease, Parkinson's disease, Huntington's disease and multiple sclerosis [6, 7, 8, 9]. Similarly, iron overload affects other organs, such as the liver and the heart. The ability to detect abnormal distributions of iron would allow the progression of these diseases to be categorised and the effectiveness of drugs targeted at these diseases to be assessed. MRI measurements have the potential to provide relevant quantitative biomarkers as they are non-invasive and sensitive to iron. This thesis aims to develop imaging approaches and accompanying analysis for the quantitative mapping of in vivo tissue iron using high field (7T) MRI.

The majority of the iron in the human body is contained in haemoglobin where it facilitates the transport of oxygen in the blood. The remainder of the iron is generally stored in ferritin. The non-haeme iron mediates the regulation of electrons for chemical processes throughout the body as iron is able to change its oxidation state to accept or to donate electrons. However, if uncontrolled, free iron can be toxic as it is able to catalyse hydrogen peroxide and superoxide ($O_2^{\bullet -}$) radicals to form highly reactive hydroxyl ($OH^{\bullet}$) radicals. Therefore it is normally contained by proteins or bound in other compounds. The non-haeme iron mainly takes the form of ferritin for iron storage and transferrin for iron transport. It is also found as hemosiderin, ferric and ferrous irons. Only ferritin is thought to be in sufficient concentrations to affect nuclear magnetic resonance (NMR) signals [10, 11].

The ferritin molecule consists of a 12nm diameter spherical protein shell called apoferritin. The apoferritin shell is made up of 24 subunits of L-ferritin and H-ferritin. The ratio of L and H differs between species and tissues depending on the requirements of the particular cell. Ferritin with a higher proportion of H-subunits is more efficient at sequestering iron for cells with high iron usage. A higher proportion of L-subunits provides greater efficiency at storing iron. As the source of the ferritin can affect the structure of the apoferritin, the affinity to storing iron atoms and the number of iron atoms that it is able to store can vary for ferritin from different types of cells i.e. between brain, liver and spleen ferritin [4, 11]. The amount of iron stored inside the molecule is called the loading factor. Along with the concentration of ferritin, loading factor variation gives rise to tissues with different susceptibilities. Susceptibility effects arise primarily from the iron stored in the core of the ferritin, so MR measurements are of the ferritin-bound iron, regardless of loading factor and ferritin concentration [12], i.e. a low concentration of ferritin with high loading factor is equivalent to a high concentration of ferritin with low loading factor, as long as both yield the same amount of iron.

1.1.2 Magnetic Properties of Ferritin

As ferritin is the most abundant form of non-haeme iron, it should produce the dominant effect on the MR signal. Therefore understanding its magnetic properties is essential for being able to model its effect and to measure its distribution using MRI. Iron occupies the core of the apoferritin shell in the form of ferric oxyhydroxide crystals [13] and changes state from Fe^{2+} to Fe^{3+} when stored [10]. Magnetometry and Mössbauer-effect measurements have been used to construct a model to describe the magnetic behaviour of ferritin. The interior of the ferritin core is in the ordered antiferromagnetic state with a Neel temperature of greater than 37°C so that a portion of the core possesses a superparamagnetic moment (SPM). The surface of the core is a disordered paramagnetic region which results in an effective magnetic moment of about 3.78 Bohr magnetons per stored iron atom. This unusual arrangement is illustrated in Figure 1.1 and is thought to be the cause of the large T2 effect, as T2 is also dependent on the loading factor.

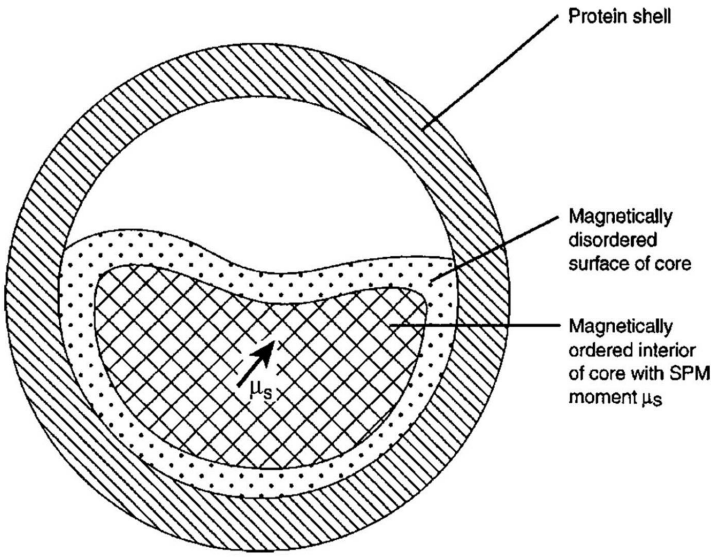

Figure 1.1: Model of ferritin core with magnetic states of each compartment [13].

1.1.3 Magnetic Properties of Haemoglobin

As haemoglobin contains the majority of the iron in the human body, it can provide a strong source of intrinsic contrast in the blood vessels. Haemoglobin consists of a protein structure with 4 subunits, each with an iron-containing haeme group. Each ferrous ion (Fe^{2+}) can bind an oxygen molecule, changing to a ferric ion (Fe^{3+}), for transportation around the body. The transition of the iron atoms in haemoglobin results in a dynamic magnetic state. Deoxyhaemoglobin is paramagnetic, similar to ferritin, due to there being an unpaired electron in each haeme group [14]. Binding of an oxygen molecule to the haeme group causes a change in the spin states of the oxygen molecule, freeing orbitals to accept electrons from the iron atom, making the overall molecule diamagnetic [15], as shown in Figure 1.2. Therefore it has an oxygenation dependent magnetic susceptibility which can be exploited.

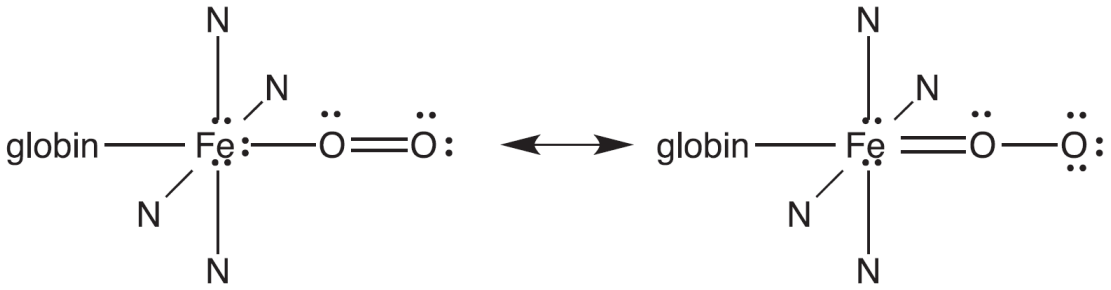

Figure 1.2: Binding of oxygen atom to iron in haem group. Bonds represented with lines and unpaired electrons with dots [16].

1.1.4 Magnetic Properties of Myelin

Myelin is abundant in white matter tissue where the concentration of iron is lower and due to the interesting magnetic properties of myelin, it can confound measurements of iron. The myelin sheath is an electrically insulating layer, which is part of the Schwann cells that wrap around the neuronal axons. Myelin consists of lipids ($\sim$70%) and proteins ($\sim$30%) [17] which form a phospholipid bilayer, wrapped around the axon multiple times to form a laminated structure. This generates microscopic field variations [18] giving rise to an anisotropic diamagnetic susceptibility, due to the highly ordered structure, most likely originating from the alkyl chains of the phospholipid bilayer [19]. A theoretical framework has been developed to model the anisotropic susceptibility of myelin. It consists of infinite hollow cylinders with three compartments, an axonal space, myelin and an extracellular space [20], as shown in Figure 1.3.

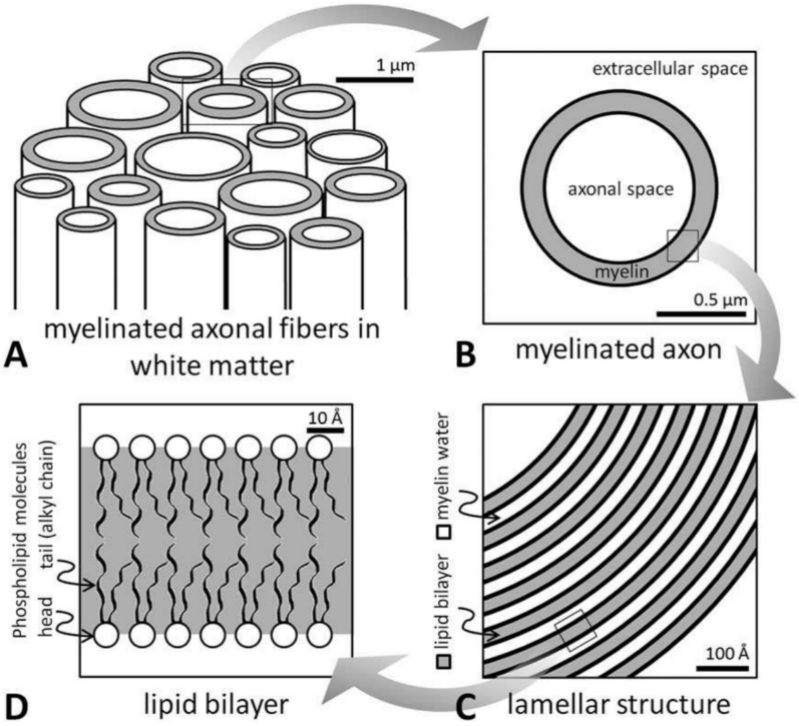

Figure 1.3: A and B: modelled structure of myelinated fibre bundle and myelin fibre. C and D: physical micro-structure of the myelin compartment and lipid bilayer [20].

1.2 Thesis Overview

Chapter 2 introduces the principles of nuclear magnetic resonance and magnetic resonance imaging, from polarisation to detection, including spatial information encoding and relaxation. Two susceptibility-based imaging techniques are described, susceptibility weighted imaging and quantitative susceptibility mapping.

Chapter 3 describes analytical and computational models of the effects of field inhomogeneities on static and diffusing spins, for a variety of system geometries. These results are used to validate the susceptibility measurements from a ferritin-doped agar phantom, the underlying principle explored throughout this thesis.

Chapter 4 details the design of an apparatus to enable temperature dependent scanning. A description of post-mortem tissue preparation and the measurement of relaxation times and susceptibility values across a range of temperatures, with comparison to a second ferritin-doped agar phantom, is given. Relaxation times and susceptibility values of the post-mortem tissue are also measured with respect to fixation time, from one to twelve months.

Chapter 5 explores the delineation and identification of the thalamic nuclei. A range of clustering techniques are assessed, to automatically segment the thalamic nuclei in histological images, which are compared with manual outlines. The optimisation of post-mortem and in vivo imaging are described. The automatic segmentation and manual outlines are then compared between the histology, post-mortem and in vivo data.

Chapter 6 describes the segmentation of the arteries and veins from time of flight and susceptibility weighted images, respectively. These are used to generate arterial and venous maps, an overlap map and a venous atlas. Additionally, oximetry measurements are made of the cerebral vessels.

Finally, Chapter 7 provides a summary of the results in this thesis. The limitations of each of the projects are discussed and some possible extensions are presented.

Bibliography

[1] Allen D Elster. Sellar susceptibility artifacts: theory and implications. *American Journal of Neuroradiology*, 14(1):129–136, 1993.

[2] John F Schenck. The role of magnetic susceptibility in magnetic resonance imaging: MRI magnetic compatibility of the first and second kinds. *Medical Physics*, 23(6):815–850, 1996.

[3] Antoine J Maubon, Jean-Michel Ferru, Vincent Berger, Marie Colette Soulage, Marc DeGraef, Pierre Aubas, Patrice Coupeau, Erik Dumont, and Jean-Pierre Rouanet. Effect of field strength on MR images: comparison of the same subject at 0.5, 1.0, and 1.5 T. *Radiographics*, 19(4):1057–1067, 1999.

[4] Dana Boyd, Ch Vecoli, DM Belcher, SK Jain, and JW Drysdale. Structural and functional relationships of human ferritin H and L chains deduced from CDNA clones. *Journal of Biological Chemistry*, 260(21):11755–11761, 1985.

[5] B Hallgren and P Sourander. The effect of age on the non-haem in iron in the human brain. *Journal of Neurochemistry*, 3(1):41–51, 1958.

[6] Luigi Zecca, Moussa BH Youdim, Peter Riederer, James R Connor, and Robert R Crichton. Iron, brain ageing and neurodegenerative disorders. *Nature Reviews Neuroscience*, 5(11):863–873, 2004.

[7] Ya Ke and Zhong Ming Qian. Iron misregulation in the brain: a primary cause of neurodegenerative disorders. *The Lancet Neurology*, 2(4):246–253, 2003.

[8] Ajay Vikram Singh and Paolo Zamboni. Anomalous venous blood flow and iron deposition in Multiple Sclerosis. *Journal of Cerebral Blood Flow & Metabolism*, 29(12):1867–1878, 2009.

[9] Kathryn E Hammond, Meredith Metcalf, Lucas Carvajal, Darin T Okuda, Radhika Srinivasan, Dan Vigneron, Sarah J Nelson, and Daniel Pelletier. Quantitative in vivo magnetic resonance imaging of Multiple Sclerosis at 7 Tesla with sensitivity to iron. *Annals of Neurology*, 64(6):707–713, 2008.

[10] John F Schenck and Earl A Zimmerman. High-field magnetic resonance imaging of brain iron: birth of a biomarker? *NMR in Biomedicine*, 17(7):433–445, 2004.

[11] E Mark Haacke, Norman YC Cheng, Michael J House, Qiang Liu, Jaladhar Neelavalli, Robert J Ogg, Asadullah Khan, Muhammad Ayaz, Wolff Kirsch, and Andre Obenaus. Imaging iron stores in the brain using magnetic resonance imaging. *Magnetic Resonance Imaging*, 23(1):1–25, 2005.

[12] Bing Yao, Tie-Qiang Li, Peter van Gelderen, Karin Shmueli, Jacco A de Zwart, and Jeff H Duyn. Susceptibility contrast in high field MRI of human brain as a function of tissue iron content. *Neuroimage*, 44(4):1259–1266, 2009.

[13] Rodney A. Brooks, Josef Vymazal, Ron B. Goldfarb, Jeff W. M. Bulte, and Phlip Aisen. Relaxometry and magnetometry of ferritin. *Magnetic Resonance in Medicine*, 40(2):227–235, 1998.

[14] Linus Pauling and Charles D Coryell. The magnetic properties and structure of the hemochromogens and related substances. *Proceedings of the National Academy of Sciences*, 22(3):159–163, 1936.

[15] Linus Pauling and Charles D Coryell. The magnetic properties and structure of hemoglobin, oxyhemoglobin and carbonmonoxyhemoglobin. *Proceedings of the National Academy of Sciences*, 22(4):210–216, 1936.

[16] Kara L Bren, Richard Eisenberg, and Harry B Gray. Discovery of the magnetic behavior of hemoglobin: A beginning of bioinorganic chemistry. *Proceedings of the National Academy of Sciences*, 112(43):13123–13127, 2015.

[17] Nicole Baumann and Danielle Pham-Dinh. Biology of oligodendrocyte and myelin in the mammalian central nervous system. *Physiological Reviews*, 81(2):871–927, 2001.

[18] Jongho Lee, Karin Shmueli, Byeong-Teck Kang, Bing Yao, Masaki Fukunaga, Peter Van Gelderen, Sara Palumbo, Francesca Bosetti, Afonso C Silva, and Jeff H Duyn. The contribution of myelin to magnetic susceptibility-weighted contrasts in high-field MRI of the brain. *Neuroimage*, 59(4):3967–3975, 2012.

[19] Wei Li, Bing Wu, Alexandru V Avram, and Chunlei Liu. Magnetic susceptibility anisotropy of human brain in vivo and its molecular underpinnings. *Neuroimage*, 59(3):2088–2097, 2012.

[20] Jongho Lee, Yoonho Nam, Joon Yul Choi, Eung Yeop Kim, Se-Hong Oh, and Dong-Hyun Kim. Mechanisms of T2* anisotropy and gradient echo myelin water imaging. *NMR in Biomedicine*, 30(4):e3513, 2017.

Chapter 2

NMR

2.1 Magnetisation

Polarisation

Nuclear magnetic resonance is a technique that exploits the magnetic properties of certain elements. Nuclei that contain an odd number of protons or neutrons such as ^{1}H, ^{13}C, ^{19}F and ^{31}P, possess intrinsic spin angular momentum, J. This results in a magnetic moment, $\boldsymbol{\mu} = \gamma \mathbf{J}$, which interacts with an applied uniform magnetic field, $\mathbf{B_0}$, conventionally defined as being along the z-axis. The magnetic moment experiences a torque, $\boldsymbol{\tau} = \boldsymbol{\mu} \times \mathbf{B}$, which due to the angular momentum causes the spin to precess at the Larmor frequency, $\omega = \gamma \mathrm{B}_0$.

The spin angular momentum is given by $J = \hbar\sqrt{I(I+1)}$, where I is the spin quantum number and each Cartesian component of the spin angular momentum has (2I+1) eigenstates, described by quantum number, m. This is the cause of the Zeeman effect. In biological tissue, the most abundant isotope is ^{1}H which has a spin quantum number of I=1/2 and eigenstates of m=1/2 and m=-1/2. The energy is given by $E = -\boldsymbol{\mu}.\mathbf{B}$ which results in two Zeeman energy levels, as shown in Figure 2.1.

The spins are distributed among the energy levels according to the Boltzmann distribution. Under thermal equilibrium, slightly more spins tend to occupy the lower energy state and are aligned with the magnetic field (shown in Figure 2.2), resulting in a net magnetisation,

$$M_0 = \frac{n(\gamma\hbar)^2}{4k_B T} B_0 \tag{2.1}$$

where n is the number of spins per unit volume, γ is the gyromagnetic ratio, $\hbar$ is Planck's constant over 2π, k_B is Boltzmann's constant and B_0 is the applied magnetic field.

Manipulation of the Magnetisation

To induce transitions of the spins between the energy states, photons are used with an energy corresponding to the energy difference between the two energy states, $\Delta E = hv = \hbar\omega = \gamma\hbar B$. For ^{1}H at 7T, this corresponds to a frequency of 298MHz, associated

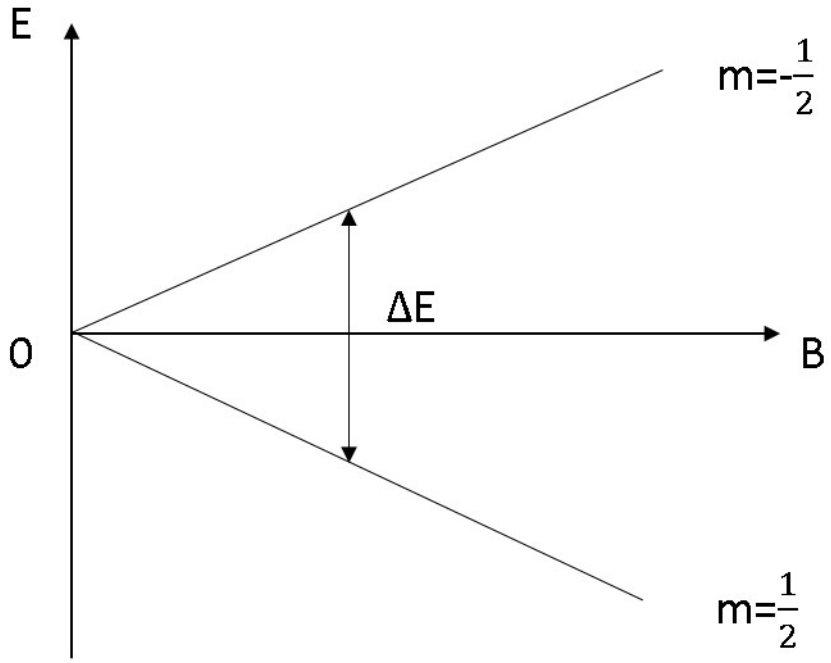

Figure 2.1: Zeeman splitting energy level diagram. E is the energy and B is the applied magnetic field.

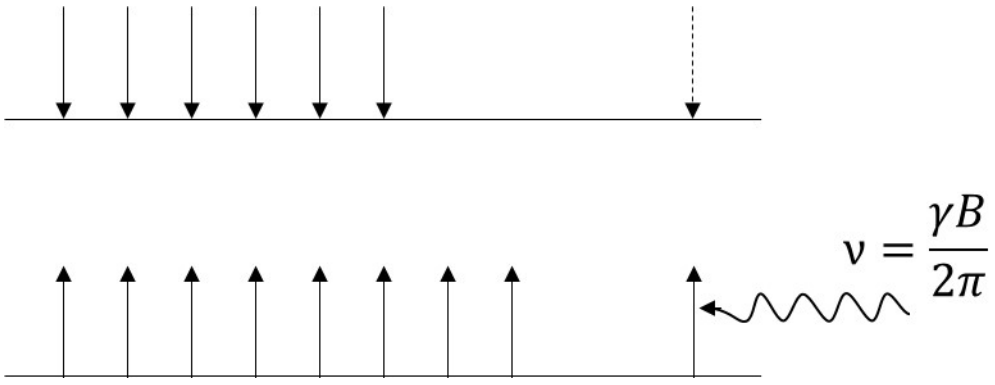

Figure 2.2: Spin population difference and excitation.

with an alternating magnetic (B_1) field. This falls in the radiofrequency (RF) range, so RF pulses are used to excite the spins from the lower energy state to the higher energy state.

It is easier to observe the behaviour of the magnetisation if we switch frames of reference, from the stationary (laboratory) frame to a rotating frame of reference, which rotates at the frequency of the RF pulse. In the rotating reference frame, the effect of an RF pulse along the x-axis is to cause the net magnetisation to precess about the y-z plane with a frequency of $\omega_1 = \gamma B_1$. The angle through which the magnetisation is tipped, is determined by the strength of the RF pulse (B_1) and the duration of the pulse (τ), as given by

$$\alpha = \gamma B_1 \tau. \tag{2.2}$$

Detection

The magnetisation can be flipped to varying degrees based on the length and amplitude of the RF pulse. After the pulse, the magnetisation precesses about B_0 and induces a voltage in an RF coil. In practice the voltage is measured via phase sensitive detection (PSD), where the detected signal is subtracted from a reference signal of frequency $\omega = \gamma B_0$, resulting in a signal that is usually in the audio spectrum. In quadrature PSD, two phase sensitive detectors are used, with a 90^o phase shift between the reference signals, to distinguish between a positive and negative phase difference of the detected signal. This results in detecting a complex NMR signal, $S = S_0.exp(i\omega t)$, which can be described by its magnitude and phase,

$$magnitude = \sqrt{Re^2 + Im^2} = S_0, \quad \phi = \arctan(Im/Re) = \omega t, \tag{2.3}$$

respectively and which can be illustrated using an Argand diagram in Figure 2.3. The magnitude describes the amplitude of detected signal and the phase is a measure of frequency offsets due to local variations in magnetic fields, usually caused by interactions with neighbouring atoms or molecules in the local environment.

Relaxation

An NMR signal is detected as a free induction decay (FID), as the precessing magnetisation returns to its equilibrium state, as shown in Figure 2.4, and evolves according to the Bloch equations,

$$\frac{d\mathbf{M}}{dt} = \gamma \mathbf{M} \times \mathbf{B} - \frac{M_x \hat{\mathbf{x}} + M_y \hat{\mathbf{y}}}{T_2} + \frac{M_0 - M_z}{T_1} \hat{\mathbf{z}} \tag{2.4}$$

where T_1 is the longitudinal relaxation time and T_2 is the transverse relaxation time. The evolution of the magnetisation with respect to relaxation times is shown in Figure 2.5. T_1 relaxation describes the recovery of the longitudinal magnetisation (M_z) as the excited spins transfer energy to the surrounding environment, through dipole-dipole interaction with neighbouring magnetic nuclei or unpaired electrons, in the case of contrast agents. T_2 relaxation describes the rate at which the spins in the transverse plane become out of phase with each other, which causes the decay of the transverse magnetisation (M_{xy}). The dephasing is often dominated by inhomogeneities in the local field

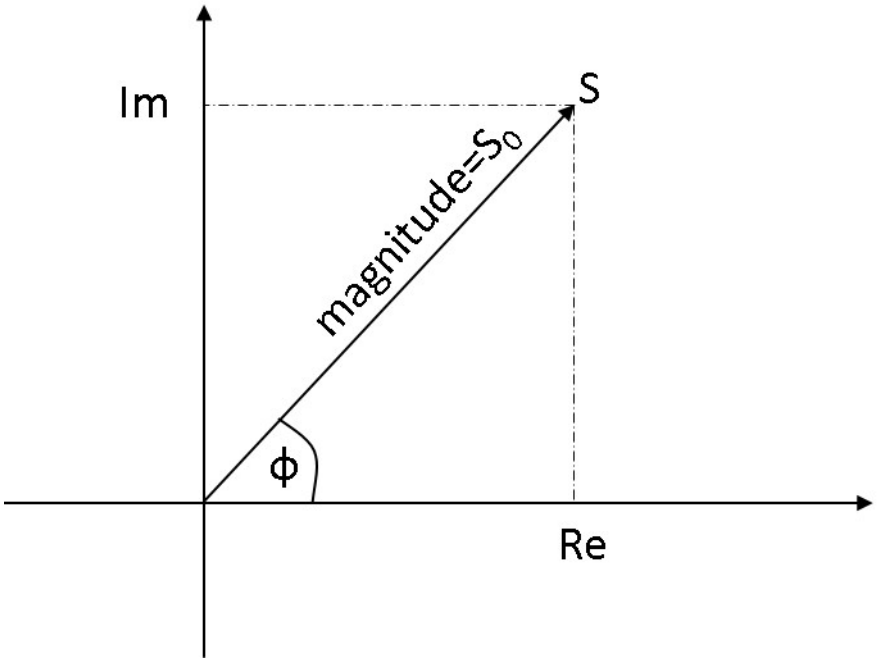

Figure 2.3: Argand diagram of complex signal obtained from quadrature phase detection.

experienced by the spins which causes them to precess at different frequencies. The effects of local time-varying field inhomogeneities (T_2) and time independent inhomogeneities (T_2'), such as in the B_0 field, are often observed together giving an effective transverse relaxation time of

$$\frac{1}{T_2*} = \frac{1}{T_2} + \frac{1}{T_2'} \tag{2.5}$$

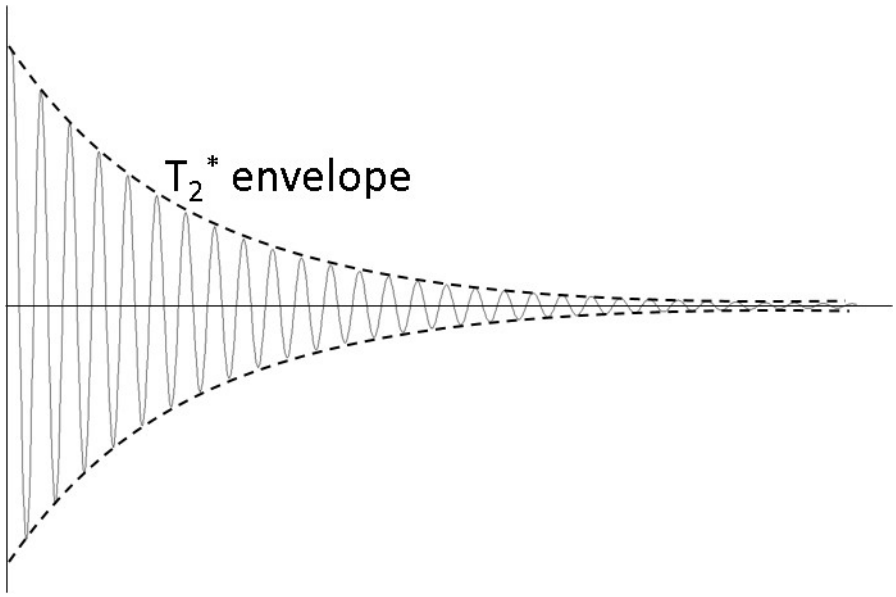

Figure 2.4: Free induction decay with T_2* envelope.

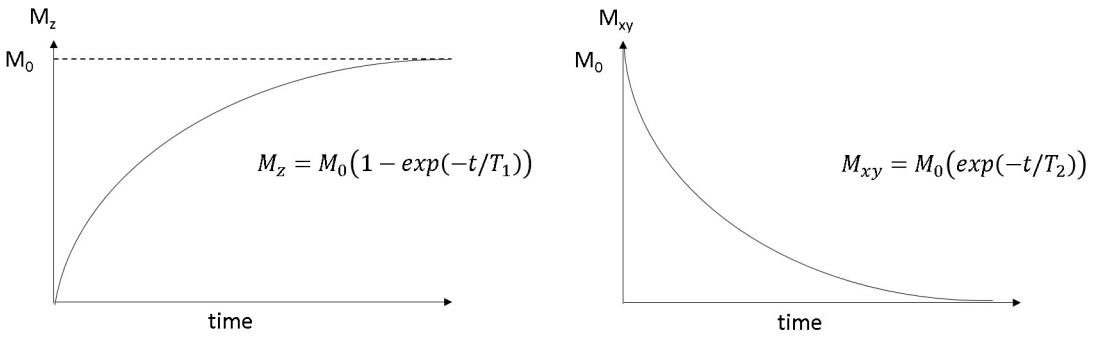

Figure 2.5: Recovery of longitudinal magnetisation with T_1 relaxation time and T_2 decay of transverse magnetisation, following a 90^o pulse.

2.2 Principles of Magnetic Resonance Imaging

In order to produce two or three dimensional images, the detected signal needs to be spatially discriminated. This is achieved by using magnetic field gradients to encode spatial information through the use of frequency, phase and selective excitation.

Slice selection

By applying a linear magnetic field gradient (along the z direction), the Larmor frequency varies linearly with position, $\omega = \gamma(B_0 + G_z z)$, as shown in Figure 2.6. Shaped RF pulses are used to selectively excite a slice for imaging. The RF carrier frequency is modulated by multiplying it with an audio frequency window that approximately takes the shape of a sinc function. In frequency space, this corresponds to convolving a delta function with a top-hat function to excite a range of frequencies. The frequency of the RF pulse is chosen to correspond to the required slice offset, and the bandwidth together with gradient amplitude determines the slice thickness, as shown in Figure 2.7.

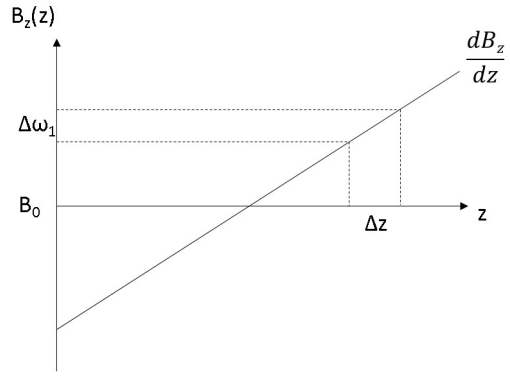

Figure 2.6: Dependence of field with position under a linear field gradient. Excitation of range of frequencies, $\Delta\omega_1$ and corresponding range of position, Δz.

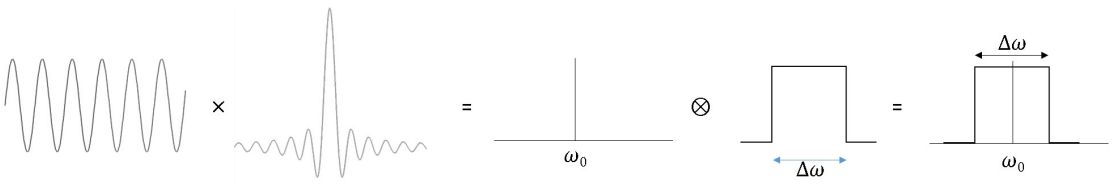

Figure 2.7: Multiplication of radio-frequency carrier wave and sinc function to produce shaped RF pulses. This corresponds to a convolution in the Fourier domain.

Frequency Encoding

After slice selection, encoding in the first dimension (along x) within the slice is done with another magnetic field gradient pulse, giving the excited spins a linear variation

of frequency with position. The sum of signal from all of the spins is detected and its magnitude is proportional to the number of spins. The signal is then Fourier transformed to obtain a frequency spectrum to distinguish the contributions of the different underlying frequencies, which are proportional to the projection of the object along the x axis. Originally, projections along multiple angles were combined to form an image by back-projection reconstruction.

Phase Encoding

More commonly, encoding in the second dimension (along y) is done via phase encoding. Additional magnetic field gradients pulses are applied in the second dimension, usually before the frequency encoding, to cause the signal to acquire a phase depending on its y-position, as shown in Figure 2.8. The phase-encoding gradient pulses are repeatedly applied with a series of different amplitudes to sample lines in k-space. K-space contains the spatial frequencies encoded in the measured complex signal. Low spatial frequencies correspond to broad structures in the image and high spatial frequencies correspond to finer details. The k-space signal is inverse Fourier transformed to distinguish the position of the sources. Additional refocusing lobes are used to reverse the dephasing caused by the slice selection and frequency encoding gradient pulses. This forms the basis of a gradient echo imaging sequence, as shown in Figure 2.9.

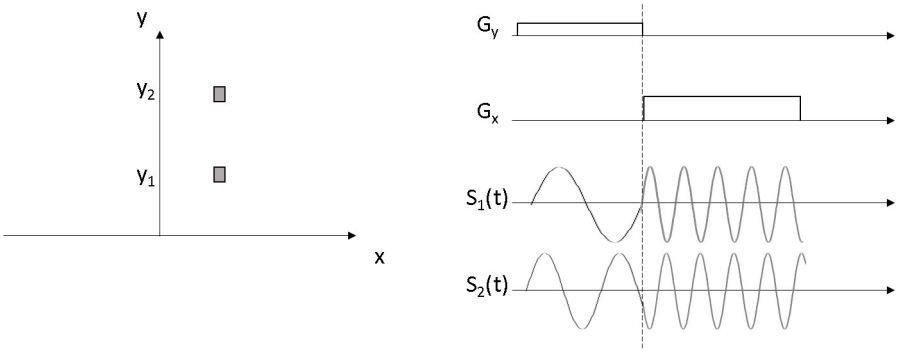

Figure 2.8: Object containing two samples separated along y. Gradients applied along x and y with resulting signal evolution showing phase and frequency encoding.

The frequency encoding, phase encoding and slice selection can be applied along any of the three perpendicular axes. For a 2D gradient echo (GE) imaging sequence, a thin volume of spins are excited via slice selection. The magnetisation is dephased under a gradient and after a short period of time, the gradient is reversed. After time TE, the area of the gradients cancel and an echo is formed from the magnetisation which has been refocused from non-time varying sources. Additionally, the GE sequence can be repeated for a range of echo times to map the decay of the transverse magnetisation and fitted to obtain values of the T_2* relaxation time.

In contrast, for a 2D spin echo (SE) sequence, the sign of the refocusing gradient is reversed and a 180^o pulse is used, as shown in Figure 2.10. In this case the spin dephasing caused by the magnetic field inhomogeneities is refocused, as well as that caused

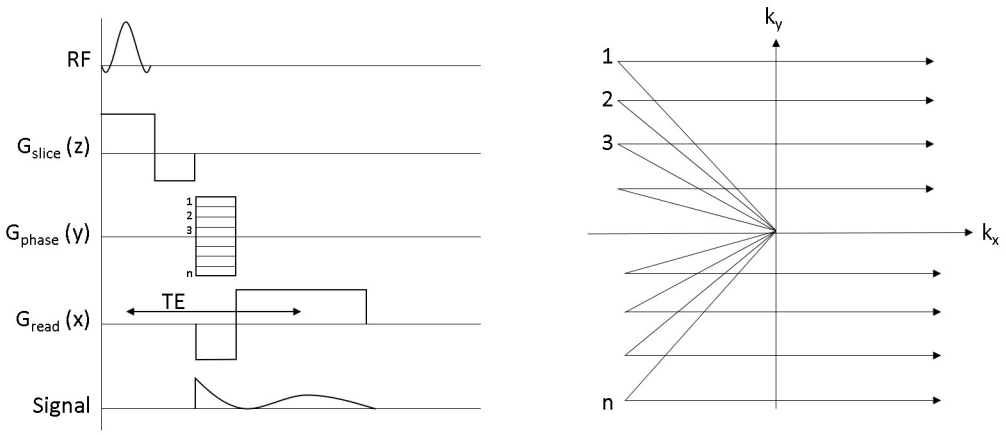

Figure 2.9: Sequence diagram of a 2D GE scan and the corresponding sampling of consecutive lines in k-space.

by the dephasing gradient in the read direction. In an inversion recovery sequence, an additional 180 degree pulse is used at the beginning of the SE sequence. The time between the initial 180 and 90 degree pulses corresponds to the inversion time. This can be varied to map the recovery of longitudinal magnetisation and fitted to calculate T_1 relaxation times.

2.2.1 Susceptibility Weighted Imaging

From the image contrasts possible using MRI, susceptibility weighted imaging (SWI) and quantitative susceptibility mapping (QSM) are used extensively in this project. The susceptibility of the iron in ferritin generates local field inhomogeneities, which produce phase shifts in the MR signal. An imaging technique that exploits this effect is susceptibility weighted imaging (SWI), which uses the phase data from gradient echo sequences to enhance the magnitude images. A mask is generated from high-pass filtered phase data, where the mask is scaled between 1 and 0 for phase values between 0 and π and the mask is set to a constant of 0 and 1 for phase values greater than π and less than 0, respectively. The mask may then be raised to the power of four, as shown in Figure 2.11 and multiplied by the magnitude image, to enhance the contrast in areas with greater susceptibility [1].

Areas with greater iron concentration acquire a more positive phase, which varies with field strength and echo time. Areas with greater phase accumulation should correspond to areas with greater iron concentration, but the phase is also affected by haeme iron and non-iron sources of susceptibility, such as myelin [2, 3]. SWI has the advantage of only requiring measurements to be made at one field strength, but SWI is a limited and semi-quantitative approach as it does not account for the dipolar nature of the source of the signal. Thus, SWI is mainly used for highlighting the venous vasculature in magnitude images, by means of the haeme iron.

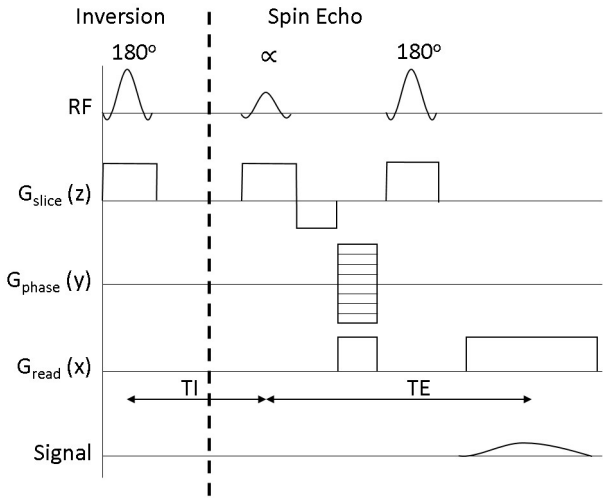

Figure 2.10: Timing diagram of an inversion recovery sequence, with a dashed line between the spin echo sequence and the additional pulses and gradients required for the inversion recovery.

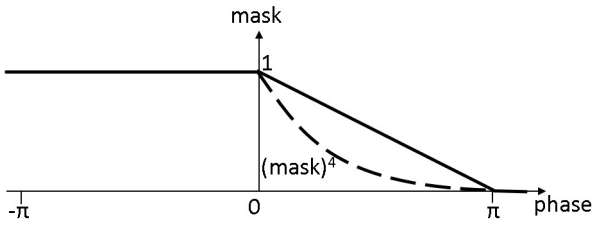

Figure 2.11: Scaling of phase values to produce phase mask (solid line) and raised to the power of four (dashed line) for SWI.

2.2.2 Quantitative Susceptibility Mapping

As interest in biological iron has increased, new methods have been developed to image iron in vivo. Quantitative susceptibility mapping (QSM) is one such technique that has gained popularity because of its ability to directly relate to intrinsic tissue properties and to provide more quantitative information. QSM builds upon the ideas of SWI as it also calculates the susceptibility from the phase and requires measurements at just one field strength. QSM is similarly affected by myelin like SWI. Unlike SWI, QSM accounts for the dipole nature of the susceptibility and can give a quantitative measurement of iron [4, 5, 6]. Therefore QSM has many features that motivate the use of this technique.

In MRI, the complex signal can provide both magnitude and phase images where the phase contains information about field perturbations. The fields outside of single structures such as spheres and cylinders have simple dipole solutions. However the field perturbations from more complex arrangements e.g. the human brain, can be masked by these dipolar field patterns, thus making it much harder to infer the underlying susceptibility distribution. In this case we must begin by integrating the effects of dipole moments over all positions, $\mathbf{r}$, to relate the induced field perturbation $\Delta\mathbf{B}$ to the mag-

netisation, $\mathbf{M}(\mathbf{r}')$,

$$\Delta\mathbf{B}(\mathbf{r}) = \frac{\mu_0}{4\pi}\iiint\left[\frac{3\mathbf{M}(\mathbf{r}')\times(\mathbf{r}-\mathbf{r}')}{|\mathbf{r}-\mathbf{r}'|^5}(\mathbf{r}-\mathbf{r}') - \frac{\mathbf{M}(\mathbf{r}')}{|\mathbf{r}-\mathbf{r}'|^3}\right]d^3\mathbf{r}' \tag{2.6}$$

where $\mathbf{r}'$ is the position of the source. This can be simplified as we are only interested in perturbations to the z-component of the field and the susceptibility is small and assumed to be independent of field, $\mu_0 M_z(\mathbf{r}') = \chi(\mathbf{r}')B_0$.

$$\Delta B_z(\mathbf{r}) \approx \frac{\mu_0}{4\pi}\iiint\left[\frac{3M_z(\mathbf{r}')\times(z-z')}{|\mathbf{r}-\mathbf{r}'|^5}(z-z') - \frac{M_z(\mathbf{r}')}{|\mathbf{r}-\mathbf{r}'|^3}\right]d^3\mathbf{r}' \tag{2.7}$$

Substituting for the magnetisation with the susceptibility, the field perturbation becomes [7, 8],

$$\Delta B_z(\mathbf{r}) = B_0\int\chi(\mathbf{r}')\times d_z(\mathbf{r}-\mathbf{r}')d^3\mathbf{r}' \tag{2.8}$$

where $d_z(\mathbf{r}) = \frac{1}{4\pi}\frac{3cos^2\theta-1}{|r|^3}$ is the unit dipole field and θ is the angle that r makes to the z-axis. This describes a convolution of the susceptibility distribution with the dipole kernel.

$$\frac{\Delta B_z(\mathbf{r})}{B_0} = \chi(\mathbf{r}')\otimes d_z(\mathbf{r}) \tag{2.9}$$

The convolution theorem states that a Fourier transform of a convolution in the physical domain is equal to the multiplication of the Fourier transforms of each component in the frequency domain. Therefore the unknown susceptibility distribution and the known dipole kernel can be treated separately.

$$\frac{\mathrm{FT}[\Delta B_z(\mathbf{r})]}{B_0} = \mathrm{FT}[\chi(\mathbf{r}')]\times\mathrm{FT}[d_z(\mathbf{r})] \tag{2.10}$$

where FT indicates a Fourier transform. This can be rearranged and inverse Fourier transformed to obtain the well posed forward problem. As the phase is related to the field perturbation, $\phi = -\Delta\omega TE = -\gamma\Delta B_z TE$, this becomes,

$$\phi = -\gamma\, B_0\, TE\, \mathrm{FT}^{-1}\left[\left(\frac{1}{3}-\frac{k_z^2}{K^2}\right)\mathrm{FT}\left(\chi(\mathbf{r}')\right)\right] \tag{2.11}$$

where k_z is the z component of k-space and $K^2 = k_x^2+k_y^2+k_z^2$. Using this relationship, the inverse problem can be obtained where the susceptibility distribution is calculated from the field perturbations [8, 9, 10] and is given by

$$\chi(\mathbf{r}') = \mathrm{FT}^{-1}\left[\mathrm{FT}\left(\frac{\phi}{-\gamma\, B_0\, TE}\right)\frac{1}{\frac{1}{3}-\frac{k_z^2}{K^2}}\right], \tag{2.12}$$

A limitation with this technique is that the denominator tends to zero under the conditions that $K^2 = 3k_z^2$. This corresponds to $cos\theta = \pm\frac{1}{\sqrt{3}}$ which occurs along the conical surfaces formed at the magic angle, 54.74°. A wide range of inversion methods have been developed to overcome this problem such as truncating values below a threshold, regularisation and using data from multiple angles of the sample relative to B_0 [11]. The latter requires less approximations, but isn't always feasible and can be more time consuming.

As QSM is mostly performed for a single orientation of the sample relative to B_0, one particularly robust technique for solving the inversion that has been developed, is an iterative least-squares (iLSQR) method [12]. In iLSQR, the streaking artefacts in the susceptibility map at the magic angle, χ_{SA}, are estimated using regularisation and prior information about ill-conditioned k-space regions, contained in the mask, M_{IC}. The streaking artefacts are then subtracted from the an initial estimation of the susceptibility, χ_0 and this is iterated a number of times to minimise the sum of the squares of the difference,

$$min_{\chi_{SA}(k)} \sum_i ||W_{Gi}.G_i\{\chi_0 - FT^{-1}[\chi_{SA}(k).M_{IC}]\}||^2 \tag{2.13}$$

where i=x, y and z, G_i are gradient operators and W_{Gi} are the corresponding weights. These are calculated more accurately from the susceptibility boundaries as estimated from the fast QSM method rather than the magnitude or phase. The weights, W_{Gi}, are set to 1 in regions where the gradient operator of the fast QSM is below a minimum threshold, to 0 in regions where the gradient operator of the fast QSM is above a maximum threshold and scaled in between [12].

Bibliography

[1] E Mark Haacke, Yingbiao Xu, Yu-Chung N Cheng, and Jürgen R Reichenbach. Susceptibility weighted imaging (SWI). *Magnetic Resonance in Medicine*, 52(3):612–618, 2004.

[2] Rodney A. Brooks, Josef Vymazal, Ron B. Goldfarb, Jeff W. M. Bulte, and Phlip Aisen. Relaxometry and magnetometry of ferritin. *Magnetic Resonance in Medicine*, 40(2):227–235, 1998.

[3] Adolf Pfefferbaum, Elfar Adalsteinsson, Torsten Rohlfing, and Edith V Sullivan. MRI estimates of brain iron concentration in normal aging: comparison of field-dependent (FDRI) and phase (SWI) methods. *Neuroimage*, 47(2):493–500, 2009.

[4] Ferdinand Schweser, Andreas Deistung, Berengar Wendel Lehr, and Jürgen Rainer Reichenbach. Quantitative imaging of intrinsic magnetic tissue properties using MRI signal phase: an approach to in vivo brain iron metabolism? *Neuroimage*, 54(4):2789–2807, 2011.

[5] Berkin Bilgic, Adolf Pfefferbaum, Torsten Rohlfing, Edith V Sullivan, and Elfar Adalsteinsson. MRI estimates of brain iron concentration in normal aging using quantitative susceptibility mapping. *Neuroimage*, 59(3):2625–2635, 2012.

[6] Wei Li, Bing Wu, and Chunlei Liu. Quantitative susceptibility mapping of human brain reflects spatial variation in tissue composition. *Neuroimage*, 55(4):1645–1656, 2011.

[7] Andreas Deistung, Ferdinand Schweser, and Jürgen R Reichenbach. Overview of quantitative susceptibility mapping. *NMR in Biomedicine*, 30(4):e3569, 2017.

[8] JP Marques and R Bowtell. Application of a Fourier-based method for rapid calculation of field inhomogeneity due to spatial variation of magnetic susceptibility. *Concepts in Magnetic Resonance Part B: Magnetic Resonance Engineering*, 25(1):65–78, 2005.

[9] E Mark Haacke, Norman YC Cheng, Michael J House, Qiang Liu, Jaladhar Neelavalli, Robert J Ogg, Asadullah Khan, Muhammad Ayaz, Wolff Kirsch, and Andre Obenaus. Imaging iron stores in the brain using magnetic resonance imaging. *Magnetic Resonance Imaging*, 23(1):1–25, 2005.

[10] Lin Li and John S Leigh. Quantifying arbitrary magnetic susceptibility distributions with MR. *Magnetic Resonance in Medicine*, 51(5):1077–1082, 2004.

[11] Sam Wharton, Andreas Schäfer, and Richard Bowtell. Susceptibility mapping in the human brain using threshold-based k-space division. *Magnetic Resonance in Medicine*, 63(5):1292–1304, 2010.

[12] Wei Li, Nian Wang, Fang Yu, Hui Han, Wei Cao, Rebecca Romero, Bundhit Tantiwongkosi, Timothy Q Duong, and Chunlei Liu. A method for estimating and removing streaking artifacts in quantitative susceptibility mapping. *Neuroimage*, 108:111–122, 2015.

Chapter 3

Simulations and Phantoms

3.1 Introduction

As described in Chapter 1, ferritin is important in the storage and supply of iron for metabolic processes. In the brain, ferritin is stored in large enough quantities to affect the signal in MR imaging. Understanding these effects is vital to enable the quantification of iron distributions in the brain. Therefore, the effect of ferritin has been modelled using a randomly arranged set of dipoles on the microscopic scale by Yablonskiy and Haacke [1], or macroscopically as a uniform susceptibility distribution (for instance contained within a sphere or cylinder) by Sukstanskii and Yablonskiy [2]. In contrast numerical simulations can be made of the effect of magnetic field inhomogeneity on a set of spin isochromats, small groups of nuclear spins processing at the same frequency. Weisskoff et al. [3] extended this using numerical Monte Carlo simulation of diffusion to estimate the attenuation of the signal by diffusion in field gradients, in spin echo and gradient echo imaging. The resulting field perturbations and the effects of diffusion on the phase accumulation of the MR signal are important as they may allow us to determine ferritin concentrations based on T_2* and susceptibility mapping.

Aims: To identify T_2*, T_1 and susceptibility characteristics of iron containing materials in spherical and cylindrical systems. To measure the susceptibility of ferritin-doped phantoms, using the known case of a cylinder in a magnetic field, with a view to identifying iron-related MR parameters in vivo.

In this chapter, analytical and computational models of the effects of field inhomogeneities on static and diffusing spins are described. Computational models of dipoles, spheres and cylinders are built to analyse the field perturbations from a simulated cylinder perpendicular to the field. The calculation of the susceptibility of the cylinder from the field perturbations inside and around the cylinder is detailed. The analysis was then applied to the phase maps from cylindrical agar phantoms containing varying ferritin concentrations, to calculate susceptibility values of each agar cylinder, at 3T and 7T. For a single dipole, the results of the field and phase, with varying volume radius are presented. The MR signal from a spherical region containing dipoles with varying volume densities is verified with the Yablonskiy analytical solution [1]. The MR signal in the presence of multiple dipoles in different arrangements are compared and the MR signal in different diffusion regimes are verified by comparison with the Sukstanskii analytical solution [2]. The simulated field perturbations from a cylinder perpendicular to

the magnetic field is shown. Finally, the results of the susceptibility calculations at 3T and 7T from fitting to the phase map inside and around the ferritin-cylinder phantoms are shown.

3.2 Theory

In magnetic resonance imaging (MRI), the signal is generated by the transverse magnetization of spins precessing at the Larmor frequency. The Larmor frequency is determined by the local magnetic field strength. However if the water molecules are not stationary, but diffusing, they will experience time-varying magnetic fields. This can cause additional attenuation of the MR signal and provides additional sensitivity to microscopic tissue structure. In the case of tissues with impermeable structures of different susceptibilities, such as myelinated fibres and blood vessels, diffusion can be restricted. We can create models of tissues which allow us to predict the signal and its behaviour for different types of tissue.

3.2.1 Analytical models of the effect of field inhomogeneities on static spins

Yablonskiy and Haacke [1] described an analytical model of the MR signal in biological tissue using dipoles, spheres and cylinders to simulate features such as blood cells and blood vessels. In the static dephasing regime, the signal from a sample containing a random distribution of dipoles is given by

$$S = \rho \, \mathrm{e}^{-i\Delta\omega t} \mathrm{e}^{-R_2|t|} \tag{3.1}$$

where ρ is a coefficient dependent on the system parameters,

$$\Delta\omega = \gamma\pi \, c \, \mu \frac{8}{9} \left(\frac{1}{\sqrt{3}} \ln \frac{\sqrt{3}+1}{\sqrt{3}-1} - 1 \right), \tag{3.2}$$

is the frequency offset and

$$R_2 = \gamma \, c \, \mu \frac{8\pi^2}{9\sqrt{3}} \tag{3.3}$$

is the relaxation rate, where $c = N/V$ is the number of dipoles per unit volume and μ is the strength of each dipole.

3.2.2 Analytical models of the effect of diffusion in inhomogeneous fields

An analytical model by Sukstanskii and Yablonskiy [2] includes the effects of diffusion on an FID and a spin echo signal, for the simple cases of impermeable cylinders and spheres composed of materials of different susceptibilities than that of the matrix in

which they are embedded. Focusing on randomly distributed spheres with radius r_s, embedded in a fixed spherical volume, the signal magnitude is given by

$$S = S_0 \exp(-\Gamma(t)) \tag{3.4}$$

where Γ is the signal attenuation function. This is dependent on the characteristic diffusion time which is given by

$$t_D = \frac{r_s^2}{D} \tag{3.5}$$

where *D* is the diffusion coefficient. The time, t, during the free induction decay (FID) is normalized to the diffusion time to give the dimensionless quantity

$$\tau = \frac{t}{t_D}. \tag{3.6}$$

The correlation function, G(t), at t=0 is given by

$$G_0 = \frac{4\zeta(\gamma\Delta\chi B_0)^2}{45} \tag{3.7}$$

where ζ is the volume fraction of spheres which is much less than one, $\Delta\chi$ is the susceptibility difference between the spheres and the surrounding matrix, and B_0 is the magnetic field strength. τ, t_D and G_0 can then be substituted into the signal attenuation function for the free induction decay (Γ_{FID}), which for the short time limit ($\tau \ll 1$ or $t \ll t_D$, i.e. when each diffusing spin has sampled only a small fraction of the field distribution around each sphere) is

$$\Gamma_{FID}(t) \simeq G_0 t_D^2 . \left[\frac{1}{2}\tau^2 - \frac{3}{2}\tau^3 + \frac{144}{35\pi^{1/2}}\tau^{7/2} + O(\tau^4)\right] \tag{3.8}$$

and in the long time limit ($\tau \gg 1$ or $t \gg t_D$, i.e. when each diffusing spin has on average sampled the whole field distribution) is

$$\Gamma_{FID}(t) = G_0 t_D^2 . \left[\frac{4}{9}\tau - \frac{2}{3}\left(\frac{\tau}{\pi}\right)^{1/2} + \frac{11}{81} - \frac{1}{27(\pi\tau)^{1/2}} + O(\tau^{-3/2})\right] \tag{3.9}$$

From the first term containing τ in these equations, the signal is expected to decrease quadratically for short times and linearly for long times.

The Sukstanskii model [2] uses a Gaussian phase distribution approximation which is valid under certain conditions. Firstly, in the short time limit, the diffusion time should be shorter than the characteristic dephasing time ($t_D < t_c$),

$$t_c = \left(\frac{\gamma\Delta\chi B_0}{d}\right)^{-1} \tag{3.10}$$

where, d=3 for spheres and d=2 for cylinders, to avoid the signal dephasing before the spins can diffuse. Only randomly distributed spheres will be considered here, as an approximation for ferritin molecules. Secondly, in the long time limit, the diffusion time should be much shorter than the characteristic dephasing time ($t_D \ll t_c$), so that the spins can sample all of the volume before the signal decays significantly [4].

3.3 Methods

A series of computational simulations were carried out to explore the expected behaviour of systems containing dipoles, cylinders and diffusing particles. These were validated with results from analytical models. The analysis of the field perturbations from a simulated cylinder were used to calculate the susceptibility values from the experimental data of a ferritin-doped agar phantom.

3.3.1 Computational models of static isochromats in inhomogeneous fields

Single Dipole

Initially, a system was constructed containing a single magnetic dipole to mimic a single ferritin molecule. The magnetic moment, μ, of such a molecule at 7T was estimated as $5.57 \times 10^{-15} Am^2$. The resultant magnetic field around the molecule was modelled as,

$$B_z(r) = \frac{\mu_0}{4\pi}\left(\frac{3\mathbf{r}(\boldsymbol{\mu}\cdot\mathbf{r})}{r^5} - \frac{\boldsymbol{\mu}}{r^3}\right)\cdot\hat{\mathbf{z}} \tag{3.11}$$

where **r** is the vector from the centre of the dipole to the position where the field is measured. The nuclear magnetic resonance (NMR) signal was then estimated as

$$S = \sum_{\mathrm{x=all\ isochromats}} S_0 e^{-i\omega_\mathrm{x} TE}. \tag{3.12}$$

where $\omega_\mathrm{x} = B_z^\mathrm{x}$ is the Larmor frequency which depends on the magnetic field strength experienced by the isochromat at x. Taking the absolute value of the complex signal gives the magnitude and the angle gives the phase of the net signal from the total volume of isochromats. The behaviour of this simulation was observed for a single dipole. The field perturbations and phase accumulation were plotted against volume fraction, for volumes of varying radii of 3×10^{-5}m to 6.7×10^{-5}m and TE=0-10ms.

Subsequently, the gradient of the logarithm of the signal magnitude and the gradient of the phase with respect to TE, were plotted against the volume fraction, to compare with the R_2* and $\Delta\omega$ values from the Yablonskiy's analytical model [1], as described in section 3.2.1. These were simulated and calculated for spheres of varying radii of (8-15)$\times10^{-5}$m and echo times TE=1-100ms. The R_2* and $\Delta\omega$ values from the analytical model were used to verify the simulated behaviour of a single dipole.

Multiple Dipoles

The initial simulation of the magnitude and phase of the signal from a single ferritin molecule in a 7T field was extended. An increasing number of dipoles, n=1 to 10, were seeded randomly in a spherical volume, with a specified minimum separation distance (15 μm) from each other and the edge of the volume. The radius of the volume was scaled to maintain a constant volume fraction of 6.4×10^{-3}. This was repeated 5 times and the magnitude and phase were obtained from the averaged signal across the runs.

The gradient of the logarithm of the magnitude signal (R_2*) and gradient of the phase variation with TE ($\Delta\omega$) were then plotted against the number of dipoles. In order to study the effect of varying degrees of ordering on the system, this whole process was then repeated for an increasing number of dipoles randomly seeded in different configurations, over a plane, a line parallel to the z axis and in a line randomly oriented in the x-y plane.

Cylindrical Perturber

Once the dipole simulations were validated, the dipoles were then replaced by a long cylinder of finite dimension and similar susceptibility, χ=0.2, 0.4 and 0.8ppm. The field perturbation from a cylinder perpendicular to the magnetic field including the effect of the sphere of Lorentz, is given by,

$$\Delta B = -\frac{\chi}{6} B_0 \tag{3.13}$$

inside the cylinder and

$$\Delta B = \frac{\chi a^2 B_0}{2r^2} \cos(2\phi) \tag{3.14}$$

outside the cylinder [5]. The resulting field perturbation map was then used to calculate ω across isochromats, on a grid of points, to form magnitude and phase images.

The resulting phase images were analysed using two methods. Firstly the susceptibility was calculated by taking the difference between the average phase inside and around the cylinder. This was fitted against TE and the field difference was then calculated using

$$\phi = -\gamma \, \Delta B \, TE. \tag{3.15}$$

The resulting value was then substituted into Equation 3.13 to allow the susceptibility to be calculated. Secondly, the susceptibility was calculated by taking the phase in an annulus around the cylinder, dividing by ΔTE, averaging across slices and fitting to an equation of the form

$$y = A\cos(2\phi + B) + C. \tag{3.16}$$

The amplitude (coefficient A) was then used to calculate the field difference which was substituted into Equation 3.14 to give a susceptibility value.

Initially the computational model was used to validate the calculation of susceptibility values from the phase of a simulated cylinder with known susceptibility. The analysis was then implemented on the experimental phase data measured for a ferritin-doped agar phantom to calculate unknown susceptibilities, as detailed in Section 3.3.3.

3.3.2 Computational models of isochromats diffusing in inhomogeneous fields

The MR signal from water molecules diffusing around a spherical perturber in a restricted volume was simulated. A single sphere with susceptibility χ and radius r_s,

was placed in the centre of a spherical volume. For a spherical perturber, the external magnetic field perturbation is given by

$$\Delta B(r) = \frac{\chi R^3 B_0}{3|\mathbf{r}|^3}(3\cos^2\theta - 1) \tag{3.17}$$

where $\mathbf{r}$ is the distance from the centre of the sphere and θ is the angle between $\mathbf{r}$ and the magnetic field, B_0=7T. The angular frequency was then calculated across the entire region by

$$\omega(\mathbf{r}) = \gamma \Delta B(r) \tag{3.18}$$

where γ is the gyromagnetic ratio of hydrogen. $\omega(\mathbf{r})$ was calculated once, across a three dimensional grid of voxels and stored as a reference, to increase the efficiency of the simulated molecules diffused around the volume. In principle this matrix could be replaced with the frequency offset for any complex arrangement of perturbers as long as the diffusion step size is equal to an integer number of voxels, otherwise the field would have to be recalculated at each position to which the particle steps.

A large number of water molecules were randomly seeded outside the spherical perturber and stepped randomly in the x, y and z directions, to simulate the random motion due to diffusion. The boundary conditions were set so that water molecules would bounce off the surface of the perturber and the edge of the spherical volume. A more realistic condition would be that the molecules could leave and reappear randomly on the edge of the volume, as they experience the field from different perturbers. This however makes it more difficult to calculate the root mean square displacement for the diffusion coefficient.

The number of diffusing molecules, N= 2×10^5, was chosen as a trade-off between speed and accuracy. The separation of points on the grid upon which the spins could diffuse (δx) was set to 10^{-6}m so the diffusion step size would correspond to an integer number of grid points (L $\times$ δx) and the total volume had a radius of, R= $80\times\delta x$. The diffusion step size (L $\times$ δx) and time step (Δt) were chosen to match the self-diffusion coefficient of water,

$$D = \frac{2(L \times \delta x)^2}{\Delta t} \tag{3.19}$$

which has been experimentally measured to be between 1.26-2.3$\times10^{-9}$ m^{2}s^{-1} from 4^{o}C to 25^{o}C, respectively [6].

The MR signal was calculated at the position of each water molecule over a series of time steps, Δt, by

$$S(t(n)) = S(t(n-1)) \times S_0 \cdot exp(i\omega(n)\Delta t) \tag{3.20}$$

where, t(n) is the time of the nth time step, t(n-1) is the time of the previous time step, S_0 is the signal magnitude and $\omega(n)$ is the angular frequency at the position of particle at the nth time step as recalled from the stored matrix.

The average magnitude and phase of the signal from all water molecules were taken to cover the entire volume and plotted against time. This was done for the short and long time limits.

Short and long time limits

In the diffusion regime, the diffusion time is shorter than the dephasing time ($t_D < t_c$). The simulation was performed in the short time limit, by setting the following parameters. The diffusion step size was (δx)= 10^{-6}m, radius of the perturber r_s= 17.5$\times\delta x$, susceptibility of the sphere = 10^{-8}, diffusion time step Δt= 0.4ms for total time extending from 0 to 12 ms.

For the long time limit, the total time investigated was increased to t= 0-1000ms, with Δt= 100ms, to make the time t longer than the diffusion time. The radius of the perturber was set to r_s= 1$\times\delta x$. The parameters of these simulations are summarised in Table 3.1 and the results were verified with analytical values from Sukstanskii [2], as described in Section 3.2.2. The numerical simulation of diffusion is very dependent on how the model is set up, for example, depending upon the number of spins considered and the diffusion step size used for a given diffusion coefficient.

	Short time Diffusion Regime	Long time Diffusion Regime
radius of perturber, r_s	17.5$\times\delta x$	1$\times\delta x$
susceptibility	10^{-8}	10^{-8}
time range	0-12ms	0-1000ms
time step, Δt	0.4ms	100ms
diffusion step size	δx	δx
Volume radius, R	80 $\times\delta x$	80 $\times\delta x$
B_0field	7T	7T

Table 3.1: Diffusion simulation parameters

3.3.3 Experimental Data from the Ferritin Phantom

Four test tubes of agar were doped with equestrian spleen ferritin at different concentrations (solution concentration of 53mg/ml ferritin, equivalent to 6.92mg/ml iron, Sigma-Aldrich, St. Louis, Missouri, United States). The range of ferritin concentrations were 0, 0.98, 1.93 and 2.84mg/ml (corresponding to an iron concentration range of 0, 0.13, 0.25 and 0.37mg/ml), which covered typical concentrations found in the brain. Ferritin from different organs have a similar structure [7] so different types of ferritin can be used in making phantoms, as long as the iron concentration is known.

The agar-filled test tubes were placed one at a time inside a spherical flask filled with water and scanned with the tube oriented perpendicular to the B_0 field (vertically). The phantom was scanned with a multi gradient echo sequence at 7T, with echo times ranging from 4ms to 40 ms and a echo step (ΔTE) of 4ms, resolution of 2mm with a FOV covering the phantom (192x192x64mm^3) and 32 slices cutting though the tube. For the 3T scans, a similar imaging sequence was used, with echo times ranging from 5ms to 60ms and a ΔTE of 5ms. These images had a resolution of 1.5mm with a FOV covering the phantom (168x168x48mm^3) and 32 slices cutting though the tube.

An algorithm was written to detect the edges and centre of the tube in each slice. This was used to define a rectangular region inside the tube and an annulus around the tube. The susceptibility value of the tube was calculated by linearly fitting to the phase difference between the inside and outside of the tube and by fitting to the cos(2ϕ) profile of the phase in the annulus around the tube, as described in section 3.3.1.

The calculated susceptibility values were then compared to the values expected from the linear fits of susceptibility against iron concentration,

$$Y = 1.10 \times X - 15.91 \tag{3.21}$$

where Y is the susceptibility in ppb and X is the iron concentration in μg iron/g wet tissue, as obtained by Zheng et al. [8] from x-ray fluorescence (XRF) measurements.

3.4 Results and Discussion

The results from the simulations of dipoles, cylinders and diffusing particles are shown with validation by comparison with the analytical models. The simulated and experimental field perturbations from a cylinder in a magnetic field are presented, with susceptibility values calculated from the phase difference and fitting of the phase at 3T and 7T.

3.4.1 Single Dipole

In Figure 3.1, the magnetic field plots show the dipolar pattern from a single dipole in the centre of a spherical volume, across three orthogonal planes through the centre of the sphere. The magnitude from the single voxel shown is constant, but decreases linearly when averaged across a grid of voxels inside the sphere. The phase for a single voxel decreases linearly and wraps between -π and π, but increases linearly when averaged across a grid of voxels inside the sphere. As the radius of the volume containing the single dipole was decreased, also increasing the volume fraction, the maximum and minimum phase at the edge of the sphere linearly increase and decrease, respectively, as shown in Figure 3.1.

For a dipole in a spherical volume with varying radius, the gradient of the logarithm of the magnitude and the gradient of the phase variation against volume fraction are shown in Figure 3.2, for the computational (simulated) and analytical models. The logarithm of the magnitude and the phase variation against time are also shown for the smallest volume radius (R=8×10^{-5}m). The simulated values obtained for the gradient of these with varying volume radius were $(-1.815\pm0.004)\times10^{5}s^{-1}$ and $(2.50\pm0.02)\times10^{4}s^{-1}$, respectively. The gradients of the coefficients R_2 and $\Delta\omega$ with 1/R^3 from the Yablonskiy simulation [1] were calculated to be $-1.80\times10^{5}s^{-1}$ and $2.38\times10^{4}s^{-1}$ respectively for a magnetic moment of $7\times10^{-21}/\mu_0$. The plots of the analytical R_2 and $\Delta\omega$ values are linear with the volume fraction. These are on the same order of magnitude as the predicted values, where the small discrepancies are due to the dipole occupying a voxel rather than a single point. This is more noticeable at smaller radii. This verified the numerical simulation and the linear behaviour of the phase from a dipole as the magnitude of the values agreed and followed a similar relationship to the initial simulation.

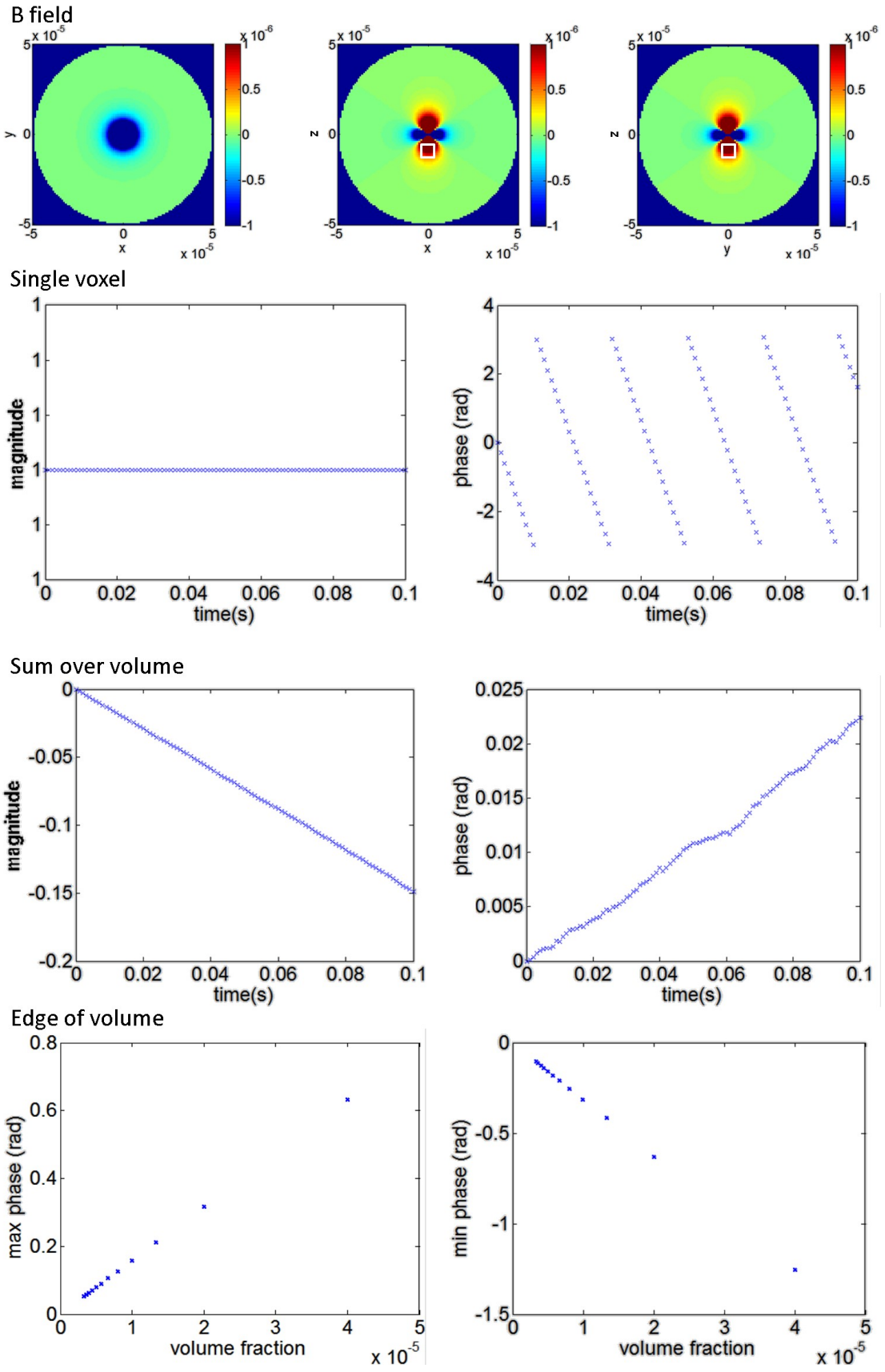

Figure 3.1: Top left to right: magnetic field from single dipole ($\mu = 7 \times 10^{-21}/\mu_0$) in the x-y, x-z and y-z planes. Middle: magnitude and phase against time from voxel marked with white square, and from a summation across the whole volume. Bottom: maximum and minimum phase values from spherical volume against inverse of radius cubed.

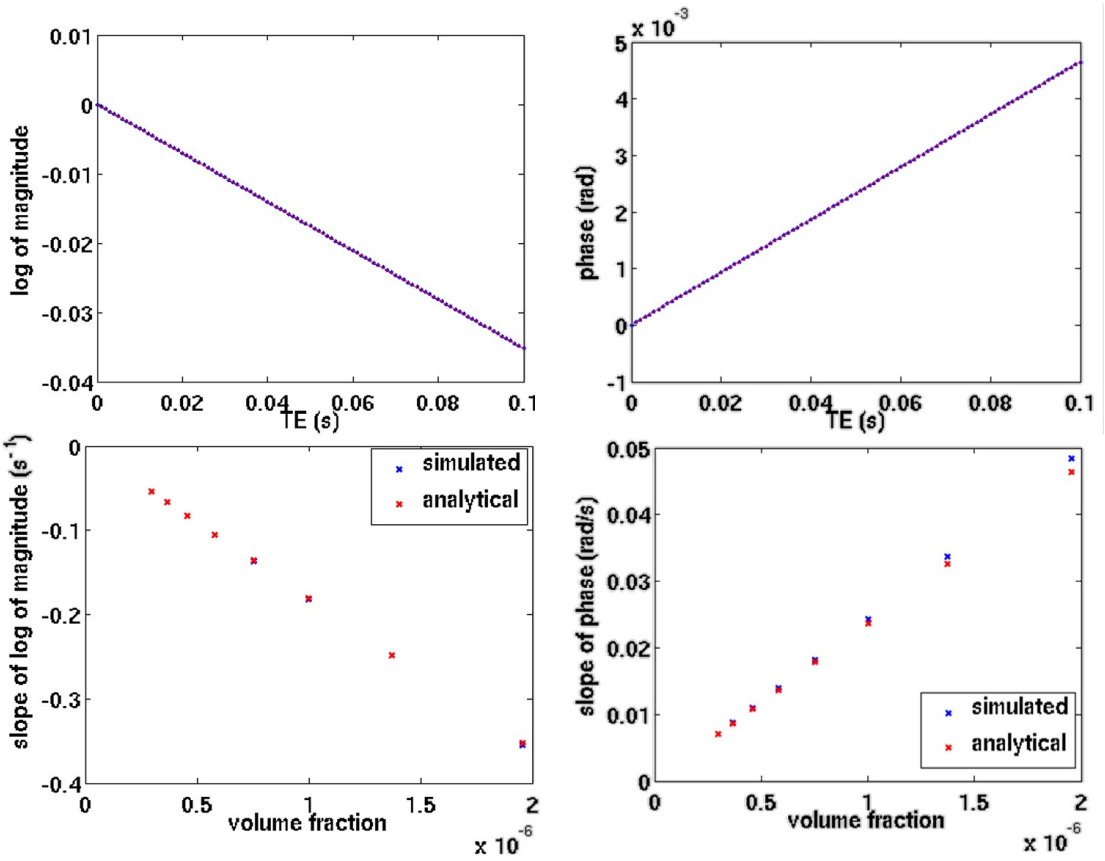

Figure 3.2: Top: the logarithm of magnitude and the phase against time, for a single dipole in the smallest volume with radius, R=8e-5m. Bottom: gradient of logarithm of magnitude and gradient of phase with varying volume radius, with corresponding R_2 and $\Delta\omega$ coefficients from Yablonskiy analytical model [1] against volume fraction.

3.4.2 Multiple Dipoles

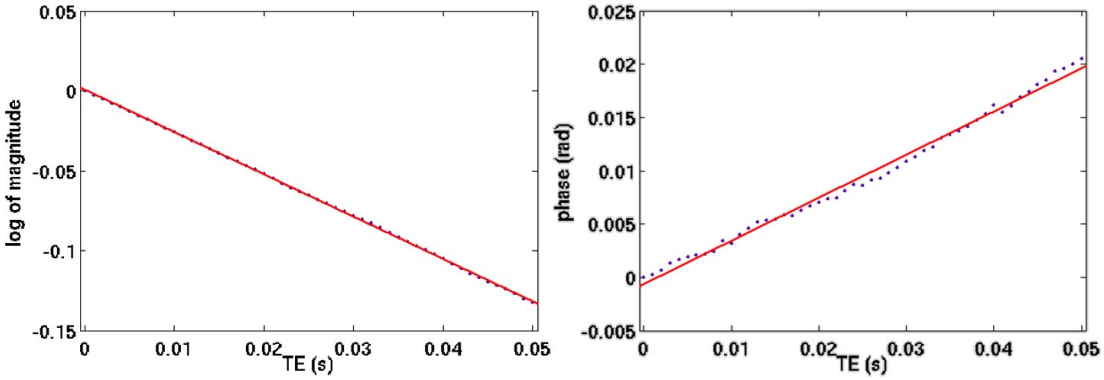

Figure 3.3: Logarithm of magnitude and the phase against time for 6 randomly positioned dipoles in a spherical volume.

In Figure 3.3, the logarithm of the magnitude decreases and the phase increases linearly with time, for a single run of 6 dipoles randomly positioned in a spherical volume. The gradients of these are approximately an order of magnitude larger than for the single dipole in Figure 3.2. Both R_2* and the gradient of the phase change each time the simulation is run as the random positioning of the dipoles changes the magnetic field inhomogeneities.

Figure 3.4 shows the gradient of the logarithm of the magnitude and the gradient of the phase for 1 to 10 dipoles randomly placed in four different arrangements, including plots of position and field perturbation maps. For dipoles distributed randomly across a spherical volume, the gradient of the logarithm of the magnitude and the gradient of the phase are approximately constant at -0.4 and 0.08, respectively. The gradients of the phase and logarithm of the magnitude for the dipoles distributed in the x-y plane are similar to those in the volume, but for small and large numbers of dipoles, are higher and lower respectively. For dipoles distributed across the volume or x-y plane, the dipoles are much further spread so the overlap is not significant.

For dipoles restricted to one dimension, a line in the x-y plane, the gradient of the phase and logarithm of the magnitude are lower than for any of the other arrangements and decreases approximately linearly with an increasing number of dipoles. This arrangement appears to cause the most dephasing of the signal, due to the negative in the exponential of the signal. For dipoles in a line in the z axis, the positive components of the field sum up whereas in a line in the x-y plane, the negative components add up. As the number of dimensions in which the dipoles can freely be placed is reduced, the dipoles are forced together resulting in a much greater overlap of the dipole fields. Overall, these gradients are consistently higher compared to the gradients for dipoles in a volume and x-y plane.

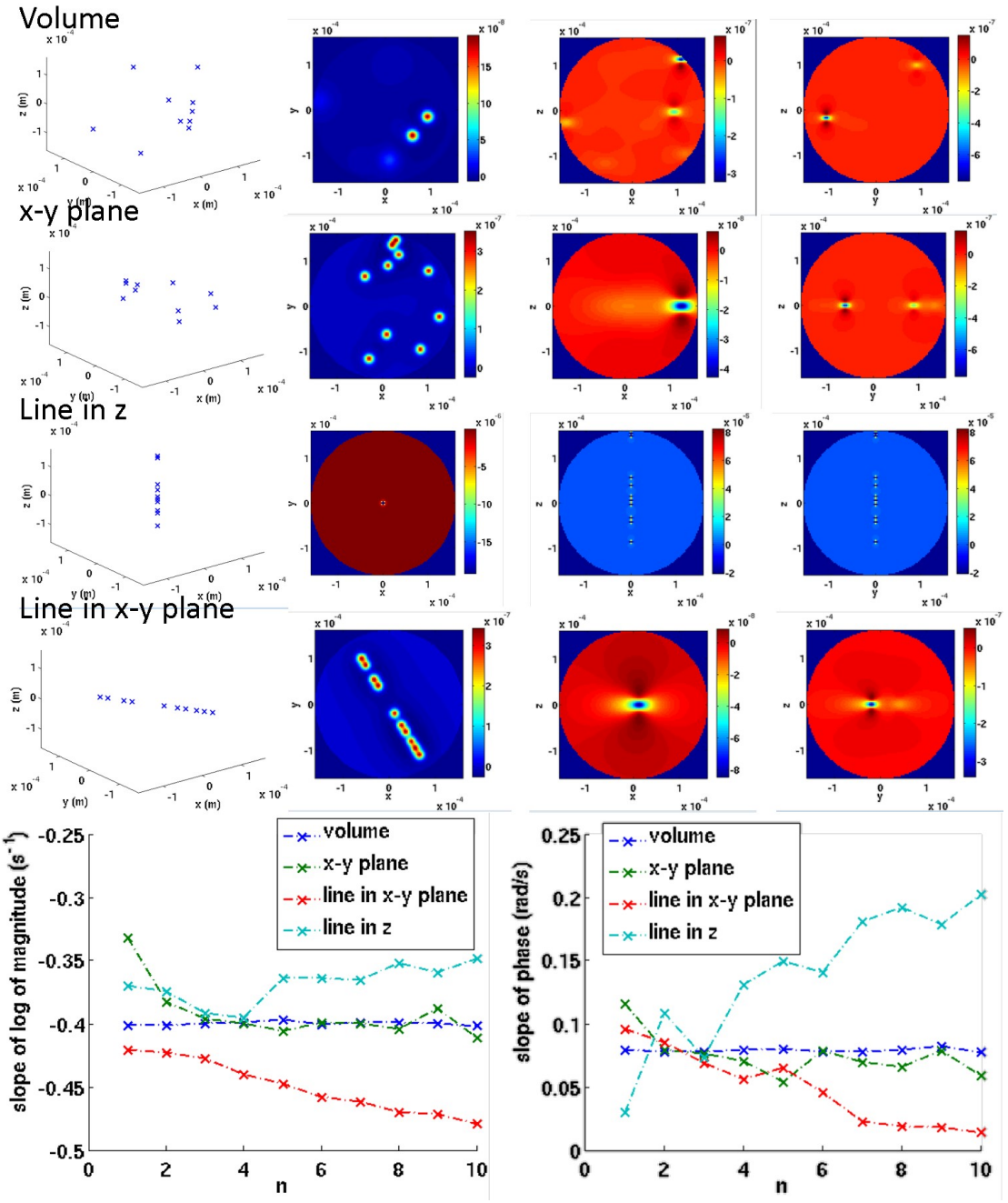

Figure 3.4: Top to bottom: plot of dipole position with resultant field perturbation maps from the last run of 10 dipoles randomly placed in the volume, x-y plane, a line parallel to the z axis and a line randomly oriented in the x-y plane. Plot of gradient of logarithm of magnitude and phase for 1 to 10 dipoles, for each arrangement.

3.4.3 Diffusion

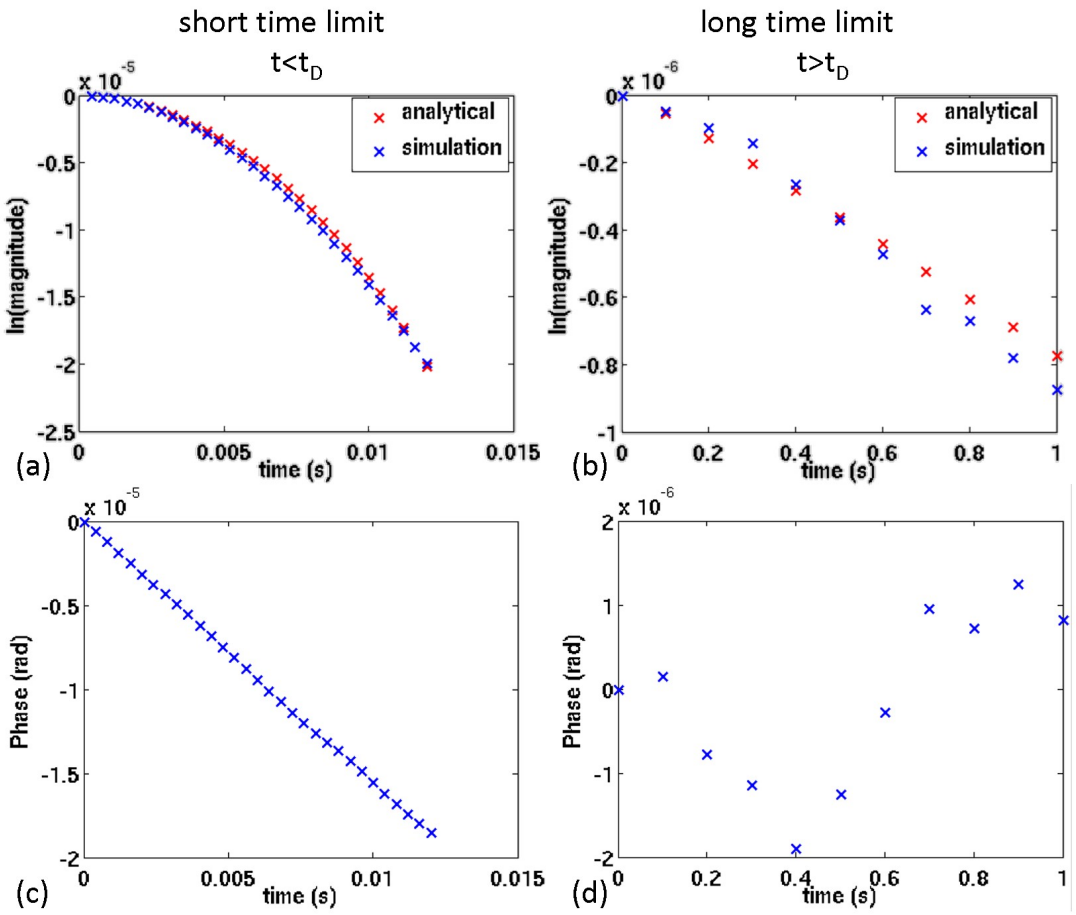

Figure 3.5: Plots showing the variation of (a) logarithm of signal magnitude and (c) phase against time for short time limit with $t_D < t_c$. (b) Logarithm of signal magnitude and (d) phase against time for long time limit with $t_D < t_c$.

In Figure 3.5a, the logarithm of the signal magnitude for the diffusion simulation and the analytical solution, in the short time limit, show good agreement. However, the analytical solution does not provide an expression for the expected phase variation. The parameters as detailed in Section 3.3.2, resulted in diffusion times and correlation times of t_D=0.041s and t_c=0.160s, respectively. Figure 3.5a shows a quadratic variation of the logarithm of the signal magnitude with time, as expected. In Figure 3.5c, the simulated phase varies smoothly with time. This is likely due to the diffusing spins only sampling a small fraction of the field.

In the long time limit, shown in Figure 3.5b, the simulation and the model [2] match well, with a linear relationship as expected. Here t_D=0.033s and t_c=0.160s, similar to the short time limit. The effects of diffusion on the phase can be seen in Figure 3.5d, which is more undulating as the water molecules have had the chance to randomly experience different fields.

In Figure 3.6a, the fractional error increases as the maximum time range of the short

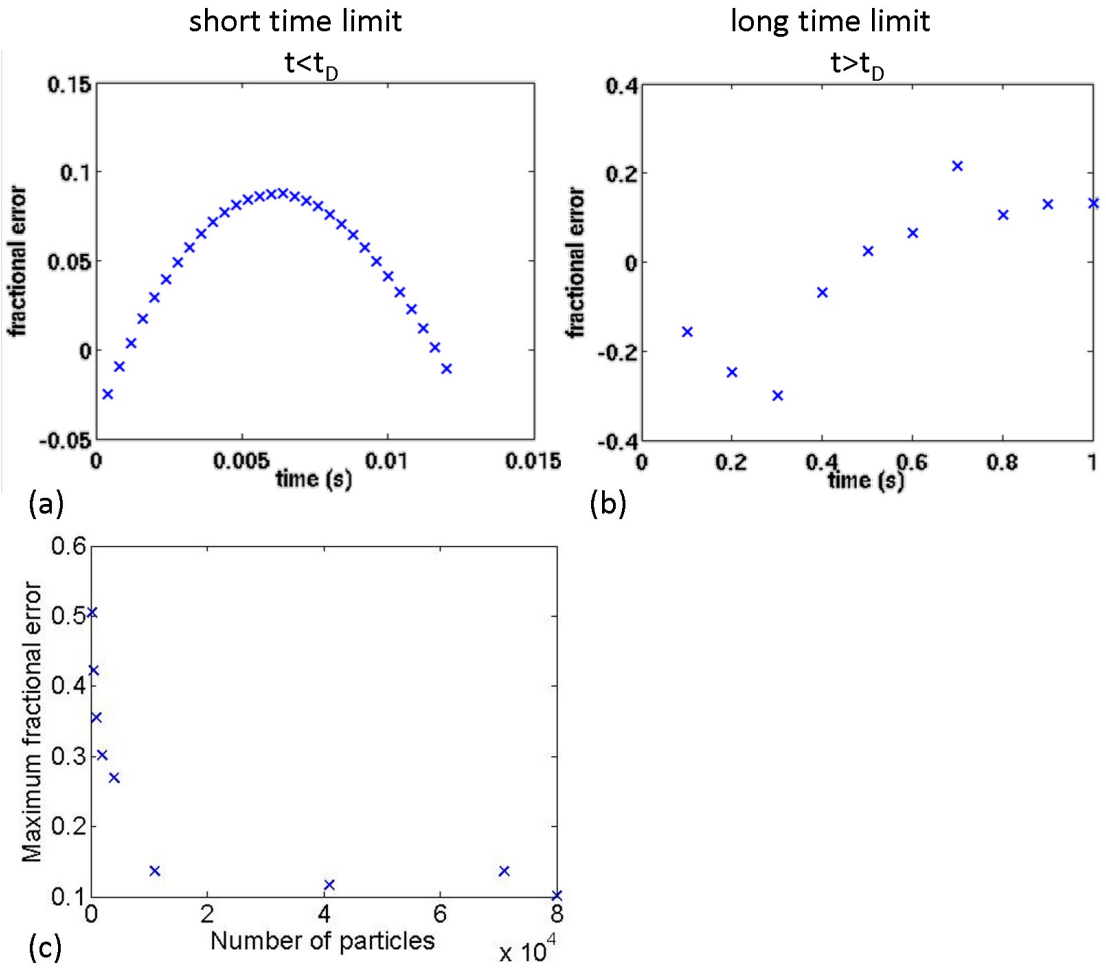

Figure 3.6: Fractional error of the signal magnitude between the analytical solution and simulation for (a) short time limit and (b) long time limit, with $t_D < t_c$. (c) Maximum fractional error against number of particles for long time limit.

time limit is approached. In Figure 3.6b, the fractional error becomes negative as initially the value of the simulation is greater than the analytical solution. As the time increases, the analytic long time limit expression is satisfied more strongly and the fractional error decreases. Also there were random errors resulting from using a relatively small amount of water molecules in the simulations. The amount of under sampling in the simulation is reduced as the number of particles is increased and then plateaus, as shown in Figure 3.6c. The number of particles should be chosen as a compromise between speed and accuracy in future work involving similar simulations.

There were small errors due to the use of approximations in the analytical solution, in Equation 3.9, as the addition of the fourth non-constant term would be expected to reduce the value of the analytical solution, due to the inverse exponential. Overall, the simulations matched well with the analytical solution under the appropriate conditions.

3.4.4 Simulated Cylindrical Perturber and Experimental Ferritin Phantoms

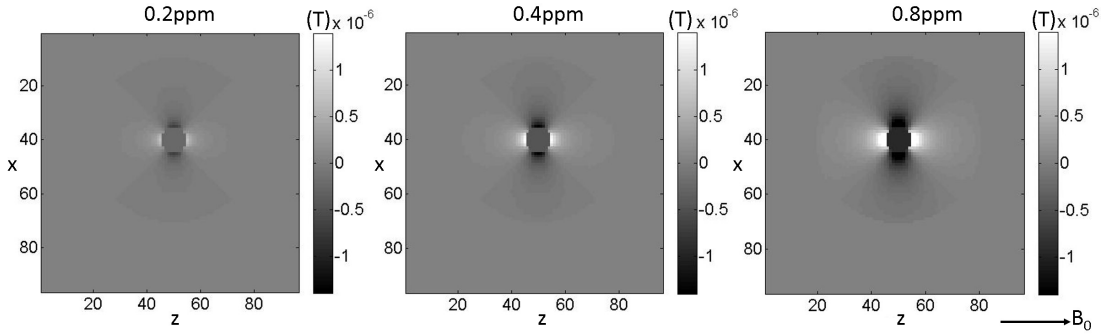

Figure 3.7: Maps of magnetic field perturbations produced by a cylinder with a simulated susceptibility difference from its surroundings of 0.2ppm, 0.4ppm and 0.8ppm in a spherical volume (left to right). The cylinder is oriented perpendicularly with respect to the 7T applied field.

Figure 3.7 shows the field perturbations produced by a cylinder perpendicular to the magnetic field, with a simulated susceptibility of 0.2ppm, 0.4ppm and 0.8ppm in a spherical volume of material of zero susceptibility. It has a dipolar pattern which becomes stronger with increasing susceptibility. The phase variation around the cylinder has a $\cos(2\phi)$ form, which can be fitted to calculate the susceptibility of the cylinder. However, taking the phase difference between the inside and outside of the cylinder produced the most accurate results for susceptibility. This is due to the phase inside the cylinder being constant.

A magnitude image of the ferritin phantom is shown in Figure 3.8 with a rectangular region marked in red inside the tube and an annulus around the tube marked in blue. The centre of the tube was determined automatically. This worked well even as the centre drifted between slices if the tube was not exactly perpendicular to the field. Also shown are phase images of the echoes. The phase accumulates with echo time and the dipolar pattern due to the cylindrical sample can be seen.

Figure 3.9 shows how the calculated susceptibility values vary with iron concentration for the ferritin samples scanned at 3T and 7T. The susceptibility increases with ferritin and hence iron concentration, as expected. A reason for the discrepancy between the two sets of points could be that the ferritin samples were scanned at the two field strengths approximately a week apart. The samples could have deteriorated slightly in this time therefore changing the composition of the samples.

The expected susceptibilities values for the range of iron concentrations used are -16, 125, 261 and 392 ppb using the XRF fit (Eq 3.21) [8]. The gradient of the measured values appears to be greater than the predicted values which may be due to the fact that the phantoms were made using agar rather than gelatine, as Zheng et al. did, which would change the reference susceptibility.

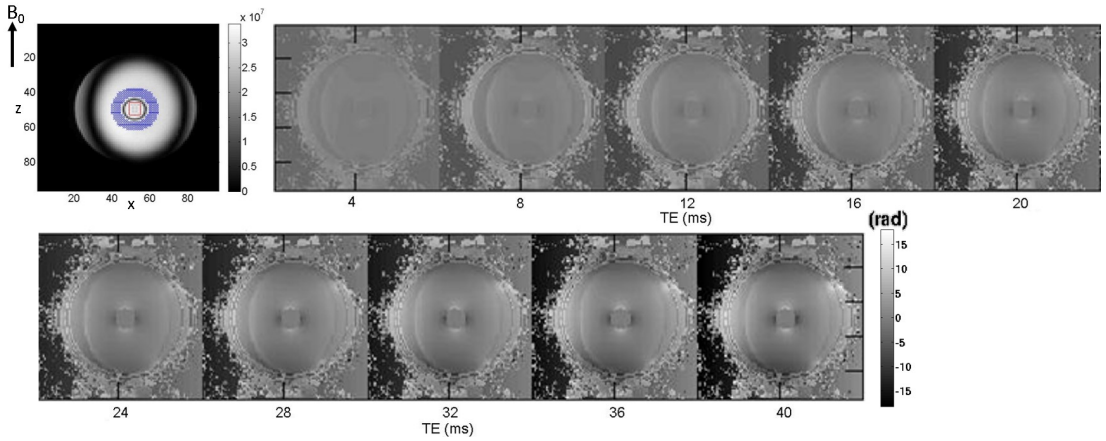

Figure 3.8: Magnitude image of ferritin phantom aligned perpendicular to B_0, with rectangular ROI inside tube and annulus around tube (top left). Phase images produced from gradient echo images acquired at echo times ranging from 4ms to 40 ms (top right and bottom).

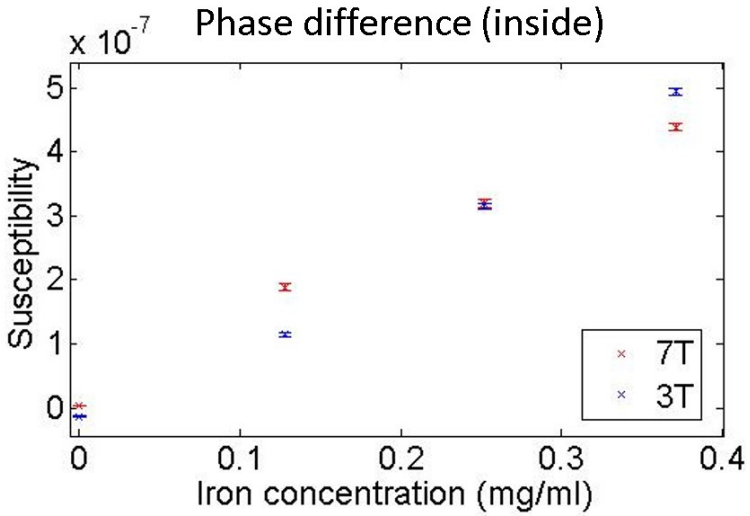

Figure 3.9: Susceptibility against concentration of iron, calculated from the phase difference at 3T and 7T.

3.5 Conclusion

In this project, the field and phase variation produced by different arrangements of dipoles and a cylindrical perturber oriented perpendicular to the field, were investigated. The observed behaviour for a single dipole was that the phase variation with TE showed a negative slope, as expected. The signal magnitude decreased and the phase variation with echo time increased when averaged across a spherical volume. R_2* and the gradient of the phase varied linearly with the volume fraction, as predicted by Yablonskiy [1].

For multiple dipoles, the gradient of the logarithm of the magnitude and the gradient of the phase with TE increased with increasing number of dipoles, for a fixed volume radius. For the different arrangement of dipoles and fixed volume fraction, the slope of the logarithm of the magnitude and the slope of the phase were approximately constant for dipoles randomly placed in the volume and was similar for dipoles randomly placed in the x-y plane. Both the slope of the logarithm of the magnitude and the slope of the phase increased, as the dipoles were restricted to a line parallel to the z axis and decreased for dipoles restricted to a line in the x-y plane, due to the overlap of the dipolar fields.

The effect of diffusion on the signal evolution was simulated for a single spherical perturber in a spherical volume. The parameters were varied to probe both the short and long time regimes. The variation of logarithm of the signal magnitude agreed well with the Sukstanskii analytical solution [2], for both the short and long time limits.

The simulated data from a cylinder oriented perpendicular to the applied magnetic field was used to test the fitting of the internal phase variation, to calculate the susceptibility of the cylinder. The phase images were observed to contain a dipolar field pattern around the cylinder.

Finally, the susceptibility measurements of the ferritin phantoms increased with the concentration of ferritin and correlated well between 3T and 7T measurements. The gradient of the 3T measurements was higher, possibly indicating that the samples had deteriorated slightly between the scanning sessions. The measured values agreed well with those reported in previous work [8].

Bibliography

[1] Dmitriy A Yablonskiy and E Mark Haacke. Theory of NMR signal behavior in magnetically inhomogeneous tissues: the static dephasing regime. *Magnetic Resonance in Medicine*, 32(6):749–763, 1994.

[2] Alexander L Sukstanskii and Dmitriy A Yablonskiy. Gaussian approximation in the theory of MR signal formation in the presence of structure-specific magnetic field inhomogeneities. effects of impermeable susceptibility inclusions. *Journal of Magnetic Resonance*, 167(1):56–67, 2004.

[3] Robert Weisskoff, Chun S Zuo, Jerrold L Boxerman, and Bruce R Rosen. Micro-

scopic susceptibility variation and transverse relaxation: theory and experiment. *Magnetic Resonance in Medicine*, 31(6):601–610, 1994.

[4] Alexander L Sukstanskii and Dmitriy A Yablonskiy. Effects of restricted diffusion on MR signal formation. *Journal of Magnetic Resonance*, 157(1):92–105, 2002.

[5] Ksimon Chu, Yan Xu, James A Balschi, Charles S Springer, et al. Bulk magnetic susceptibility shifts in NMR studies of compartmentalized samples: use of paramagnetic reagents. *Magnetic Resonance in Medicine*, 13(2):239–262, 1990.

[6] Manfred Holz, Stefan R Heil, and Antonio Sacco. Temperature-dependent self-diffusion coefficients of water and six selected molecular liquids for calibration in accurate 1H NMR pfg measurements. *Physical Chemistry Chemical Physics*, 2(20):4740–4742, 2000.

[7] YT Konttinen, V Bergroth, K Käyhkö, and S Reitamo. Human ferritin: effects of antigen source and fixation on leucocyte staining by immunoperoxidase technique. *Histochemistry*, 75(4):585–589, 1982.

[8] Weili Zheng, Helen Nichol, Saifeng Liu, Yu-Chung N Cheng, and E Mark Haacke. Measuring iron in the brain using quantitative susceptibility mapping and x-ray fluorescence imaging. *Neuroimage*, 78:68–74, 2013.

Chapter 4

Effects of temperature and fixation time on the MR parameters of ferritin in agar and post-mortem brains

4.1 Introduction

Post-mortem imaging provides a means of studying variation in MR parameters at very high spatial resolutions to improve interpretation of in vivo imaging results, particularly in disease. The susceptibility of the iron in ferritin generates local field inhomogeneities which produce phase shifts in the MR signal. MR measurements of cerebral iron concentrations can be performed using recently developed QSM techniques [1] or inferred from T_2* [2] or T_2 [3] maps, or by measuring the Field Dependent Relaxation Increase (FDRI), in which the R_2 ($1/T_2$) is calculated at multiple field strengths and the difference in relaxation rate is scaled by the difference in field strength [4]. However, these are not direct measurements as the effects of iron on the susceptibility can be masked by the negative susceptibility of myelin and the effects of iron on T_2 and T_2* depend on its distribution [5]. However in deep grey matter where there is little myelination, measurements of magnetic susceptibility in QSM are expected to be proportional to iron concentration [6], although this needs to be verified to ensure the validity of this technique for in vivo studies. This is made possible by comparing ex vivo MR scanning of post-mortem brain samples to iron content analysed histochemically, e.g. via Perls' staining or biochemically, by using X-ray fluorescence imaging (XRF) or inductively coupled plasma mass spectrometry (ICPMS) [7, 8].

However, tissue properties and tissue iron contents are sensitive to the way in which tissues are handled and stored post-mortem. In this chapter, the effects of formaldehyde fixation on tissue MR parameters, including T_1, T_2 and susceptibility values and the effects of formaldehyde fixation on imaging techniques and histology, are reviewed. From the literature, variables were identified that might influence the susceptibility of paramagnetic and diamagnetic components within the post-mortem samples. Based on this review of the literature, a study was designed that aimed to investigate the effects of variations in temperature and fixation time on the MR parameters of post-mortem tissue, in order to assess the compatibility of post-mortem MRI with in vivo imaging.

In this chapter, a set of equipment for temperature dependent scanning was designed

and evaluated. An agar phantom containing four cylinders doped with different concentrations of ferritin, was constructed and scanned across a range of temperatures. A sample holder for scanning post-mortem samples was also constructed. The variation in R_1, R_2* and susceptibility values of the phantom with temperature, are compared to temperature dependent measurements in a post-mortem brain. The MR parameters of post-mortem tissue were also investigated with respect to fixation time, over a period of a year. Variations in the ferritin phantom susceptibility, R_2* and R_1 with concentration and temperature was measured and the corresponding relaxivity values were calculated. Maps and plots of post-mortem MR parameters including volume against fixation time and temperature, were also obtained across a range of brain regions and compared to the ferritin phantom results.

4.1.1 Limitations of Post-mortem MRI compatibility with in vivo

Post-mortem tissue is normally fixed in order to halt decomposition. This process has been shown to affect the MR signal [9, 10, 11] and effects of fixation need to be taken into account when considering comparisons with in vivo scanning. The factors which may affect fixation include time after death, duration of fixation and method of fixation. Therefore samples need to be fixed and processed consistently to reduce variability. Understanding the factors that affect the MR properties of post-mortem samples will improve interpretation of comparisons of in vivo and post-mortem MR data. This will make post-mortem results more relevant to in vivo imaging.

Formaldehyde (Formalin)

One of the most commonly used fixation agents is formaldehyde. This is a colourless gas with the chemical formula CH_2O. It delays the breakdown of tissue by forming cross-links between proteins, which also immobilise water. This alters tissue composition in a way that produces different effects on different MR images. Formaldehyde is dissolved in water to make a solution which is usually referred to as formalin. The percentage of formaldehyde in the solution can be varied depending on how the tissue is going to be analysed.

In a study by Schmierer et al. [9], the effect of formalin fixation on the MR indices of post-mortem cortical grey matter from subjects with multiple sclerosis was investigated. Formalin fixation caused T_1 and the magnetisation transfer ratio to decrease, and the macromolecular proton fraction to increase.

The effect of the length of fixation was investigated by Dawe et al [10]. Five brain hemispheres were fixed in formaldehyde, then scanned weekly for three months and subsequently at six months post-mortem. T_2 decreased quickly in tissue near the edges of the sample, whereas T_2 of deep tissues decreased more slowly, as it takes longer for the formaldehyde to diffuse and reach the deep tissues. T_2 decreased to a minimum and then increased to a plateau. This later increase is thought to be due to tissue decomposition as this releases water and increases T_2 [10]. Therefore fixation would affect whole brains and sectioned brains differently as the deep tissues are more easily acces-

sible in sectioned samples. This is important when comparing fixed, whole samples to sectioned samples over a short fixation period. Otherwise a minimum of three months is required for fixation to stabilise in a whole brain [10].

Thelwall et al. [11] tested a range of fixation agents on an erythrocyte tissue model and agarose. Formaldehyde, Karnovsky's solution and glutaraldehyde all produced changes to the MR and biophysical properties. Again, fixation caused a significant decrease in T_2 as well as a decrease in the membrane permeability to water and a smaller decrease of the extracellular apparent diffusion coefficient ($\mathrm{ADC_{ex}}$) of water. However these quantities mostly returned to pre-fixation levels after the free fixative was washed away, with the T_2 actually then being greater than the pre-fixation value due to the effect of fixation on the agarose. The effects of temperature were also studied between 10°C and 37°C with the aim being to compare room temperature measurements to in vivo conditions. $\mathrm{ADC_{ex}}$ increased and T_2 decreased with increasing temperature. This is important as post-mortem samples are normally scanned at room temperature or lower.

Paraformaldehyde is a polymerised form of formaldehyde which can be broken down to formalin by heating or adding a base. It can then be used in tissue fixation. In a previous study, the ratio of cartilage T_1 with and without Gadolinium contrast, was largely unchanged for delayed Gadolinium-Enhanced MRI of Cartilage (dGEMRIC). However after fixation, the T_1 values with Gadolinium were consistently slightly higher [12]. In other studies of noncartilaginous tissues, paraformaldehyde fixation resulted in a decrease in both T_1 and T_2 in the brain, liver and spleen [13, 14, 15].

Manganese Enhanced MRI (MEMRI) has previously been used to compare formaldehyde fixation to the physical fixation method of focused beam microwave irradiation (FBMI). In FBMI, short, high power pulses of microwave radiation rapidly heat the tissue and partially denature the proteins. This appeared to be more destructive compared to chemical fixation, as T_1 was more comparable between formaldehyde fixed and unfixed mouse brains, than for FBMI fixation [16].

Iron leaching

During fixation of iron-loaded human spleen tissue in formalin, iron was found to be slowly leached over 60 days until levels become constant at a loss of 3% iron [17]. Also there was no evidence of chemical transformation using short-term Mössbauer spectroscopy after 200 days between freeze-dried tissue and fixed tissue which was then freeze-dried [17]. This is similar for the liver [18] but this does not hold true for tissue stored for longer than a year. This was shown with control and Parkinson's disease brains, where the extent of the chemical transformation of the ferritin correlated with the storage time in formalin [19].

Post-mortem Histology

Iron is distributed heterogeneously in the brain. The deep gray matter structures contain the highest concentration of iron (213 μg/g wet weight in the globus pallidus [21]), whereas areas with the lowest concentration include the spinal cord and deep white

matter (15 μg/g wet weight in the corpus callosum [20]). This expected distribution can be compared to MR measurements of iron in post-mortem tissue and verified with histochemical or biochemical measurements.

Immunohistochemical staining involves using a staining agent that has antibodies specific to a certain target e.g. cells or proteins. As Konttinen et al. [22] shown, spleen anti-ferritin stained cells with lobed nuclei and the spleen lining cells of a human spleen section. However heart anti-ferritin only stained the lobed cells. This was consistent for a range of fixatives including formalin, Bouin's fixative and Baker's fixative. However samples fixed with Carnoy's fixative, formol sucrose and glutaraldehyde didn't show any staining. Both spleen and heart anti-ferritin produced similar staining in human heart sections. Additionally the fixative affected the intensity of the histological staining. In spleen tissue, formalin, Baker's and Bouin's fixative produced the greatest intensity of staining, followed by Karnovsky's fixative, glutaraldehyde and formol sucrose. Carnoy's fixative stained negatively. The degree of staining is affected by the fixation agent as it has the possibility to change the chemical structure. Ferritin from different organs should have similar structure. Different types of ferritin could be used in making phantoms, as long as the iron concentration is known, as described in Chapter 3.

During the analysis of post-mortem images, the effect of iron on the susceptibility and T_2 of different systems must be understood. In order to do this, simulations were carried out, as described in Chapter 3.

4.1.2 Temperature Dependence

Imaging of iron in the brain using susceptibility measurements, can be confounded by components with different magnetic states. Iron is primarily stored in the core of ferritin molecules, which consist of a spherical protein shell. The interior of the core is in the ordered antiferromagnetic state with a Neel temperature of greater than 37°C so that a portion of the core possesses a superparamagnetic moment (SPM). The surface of the core is a disordered paramagnetic region which results in an effective superparamagnetic moment of about 3.78 Bohr magnetons per stored iron atom [23]. The susceptibility of iron-containing tissues has a temperature dependence as it obeys Curie's law,

$$\chi_{tissue} = \chi_{para} + \chi_{dia} = \frac{C}{T - \Theta} + \chi_{dia} \tag{4.1}$$

where C is the material-specific Curie constant, T is the temperature and Θ is the paramagnetic Curie temperature [6]. Myelin on the other hand consists of multiple bi-layers of phospholipids and is diamagnetic, with a negative anisotropic susceptibility. Diamagnetism is caused by electrons responding to an applied field and is largely temperature independent. The temperature dependence of different tissue components could be exploited to distinguish between these two opposing susceptibility effects, to make measurements of iron concentrations, which is usually difficult in white matter.

The R_1 and R_2 relaxation rates of water are influenced by temperature via intramolecular dipole-dipole coupling. These can be related using the Bloembergen-Purcell-Pound

(BPP) theory [24],

$$R_1 = \frac{1}{T_1} = \frac{K}{5}\left[\frac{\tau'}{1+\omega_0^2\tau'^2} + \frac{4\tau'}{1+4\omega_0^2\tau'^2}\right] \tag{4.2}$$

$$R_2 = \frac{1}{T_2} = \frac{K}{10}\left[3\tau' + \frac{5\tau'}{1+\omega_0^2\tau'^2} + \frac{2\tau'}{1+4\omega_0^2\tau'^2}\right] \tag{4.3}$$

where K is a constant, ω_0 is the Larmor frequency and τ' is the correlation time. This has a temperature dependence given by the Arrhenius law,

$$\tau' = \tau_0 exp\left(-\frac{E}{k_B T}\right) \tag{4.4}$$

where, τ_0 is a constant, E is the activation energy and k_B is the Boltzmann constant [25].

Post-mortem scanning is usually performed chilled or at room temperature, not at body temperature. Temperature is known to affect the MR parameters such as T_1, T_2* and susceptibility. The magnitude of the affect of temperature and fixation on the MR parameters will be independently determined to assess comparability of post-mortem results with in vivo scanning.

4.2 Method

A circulator was designed and built to enable temperature-controlled MR imaging. An agar phantom containing 4 ferritin-doped agar cylinders was scanned at a range of temperatures to allow comparison with the temperature controlled post-mortem data. An additional post-mortem brain was scanned at a series of fixation times and the volume, susceptibility, R_1 and R_2* values were measured.

4.2.1 Temperature Controlled Scanning

Circulator

An apparatus was designed and built to allow temperature-controlled scanning of samples. This consisted of a sample holder which was built to fit in the 32 channel receiver head RF coil. It included a port for a fibre-optic thermometer (Figure 4.1). The sample holder was placed inside the MRI scanner and was connected to a Tamson Instruments (Bleijswijk, the Netherlands) low-temperature circulator, via insulated plastic tubes, which was located in the scanner control room. The Tamson Instruments circulator was capable of cooling and heating water to -15°C and 60°C respectively, in 0.01°C increments. It contained a pump which circulated the water around the tubing and sample holder.

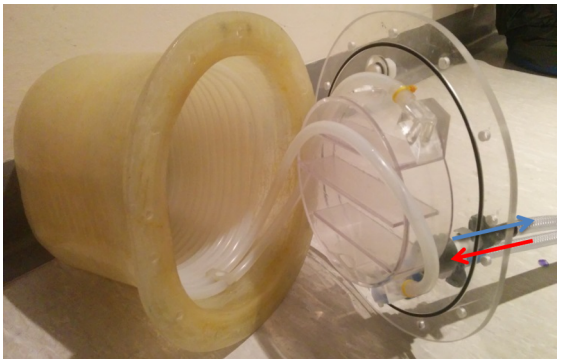

Figure 4.1: A sample holder into which water was directly pumped for temperature-controlled imaging, was built to fit inside the RF head coil.

Initially, the efficiency of the circulator was assessed, to develop an operating procedure to reliably increment the temperature of a sample. Cold water was initially pumped into the sample holder using a Tamson Instruments circulator, to achieve a temperature of ~5°C. The sample was then warmed in approximately 5°C increments to ~30°C, allowing the temperature to stabilize after each temperature increment, which took about 1 hour each time. This was achieved by heating the water around the sample to 15°C higher than the desired temperature for 25 minutes and then decreasing the temperature by 10°C for a further 35 minutes. The sample and surrounding tank were placed in a Philips 7T MRI scanner (Figure 4.2). The pump was turned off for approximately 30 minutes during scanning at each temperature to minimise flow artefacts.

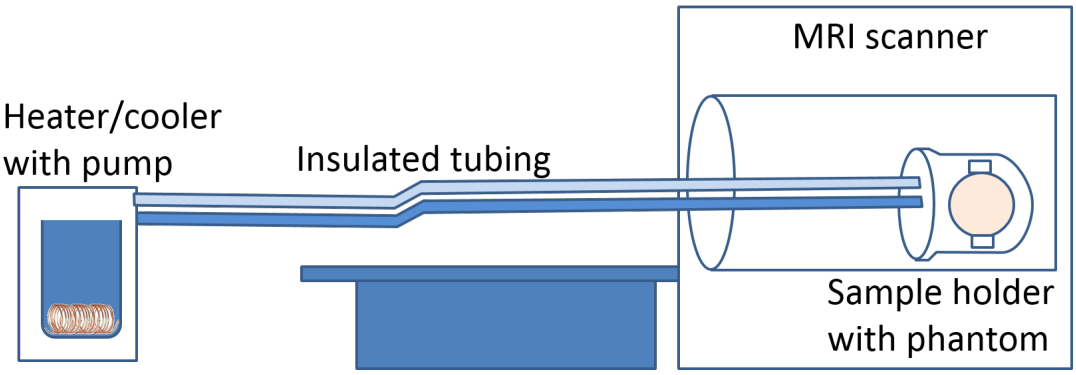

Figure 4.2: Experimental setup showing a circulating water bath with heating and cooling elements attached to the sample holder which was placed inside the scanner.

Ferritin Phantom

Four cylinders of agar were doped with ferritin (solution concentration of 53mg/ml, Sigma-Aldrich, St. Louis, Missouri, United States) at concentrations ranging from 0.5 to 3mg/ml (corresponding to an iron concentration of 6.92mg/ml in the original ferritin solution and an iron concentration range of 65 to 392μg/ml in the agar). These cylinders were embedded in a spherical agar phantom of 12cm diameter, as shown in Figure 4.3. A fibre-optic thermometer was inserted into the edge of the phantom which was then placed inside the circulator sample holder. The phantom and surrounding tank were placed in a Philips 7T MRI scanner (Figure 4.2) with the ferritin-doped cylinders oriented parallel to the field. The pump was turned off for approximately 30 minutes during scanning at each temperature. T_1 was measured using a varying inversion time, inversion recovery gradient echo sequence (1.25x1.125x1.25mm^3 voxel, FOV=200x180x72.5mm^3, with 7 TI values in the range 162-2102ms) while frequency offsets and T_2* values were measured using a multi-echo gradient echo (GE) sequence (1.25x1.25x1.25mm^3 voxel, FOV=200x180x71.25mm^3, TE1= 5.1ms, ΔTE=5.1ms, 10 echoes).

For each temperature measurement, the T_1 and T_2* values of each cylinder were calculated by fitting the variation of T_1 with temperature to the following non-linear function

$$y = A(1 - 2e^{-t/T_1}) \tag{4.5}$$

and linearly fitting for T_2*, to the logarithm of the average signal from a rectangular ROI inside each cylinder. The susceptibility of each cylinder was calculated by fitting the average phase inside the cylinder relative to the phase ($\phi = \gamma \Delta B_{int} TE$) in the surrounding agar, to the equation for the field perturbation from an infinitely long cylinder,

$$\Delta B_{int} = \frac{B_0 \Delta\chi}{2}\left(cos^2\theta - \frac{1}{3}\right) \tag{4.6}$$

where θ is the angle between the axis of the cylinder with respect to the magnetic field, estimated from the image data. The relaxivities were calculated by taking the inverse of T_1 and T_2* and fitting with respect to the iron concentration. A similar procedure was

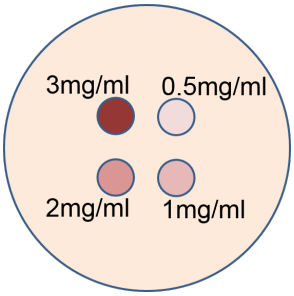

Figure 4.3: Schematic of agar phantom containing four ferritin-doped agar cylinders in a 2x2 arrangement.

carried out for the susceptibility values.

4.2.2 Temperature Dependence of Ferritin: Post-mortem

Post-mortem Tissue Preparation

Post-mortem brains were obtained from the Histopathology Department at the Queen's Medical Centre after consent was given by the coroner and the family of the deceased. This was done to allow the brains to be received whole, as the brains normally have to be dissected for the coroner's report. After the brains were extracted, one brain was fixed in formalin for 12 months to study the effect of fixation. Another brain was in fixation for 15 months before the temperature-dependent scans were performed and a further set of brains were fixed for the shortest possible period of between 1 to 5 months to investigate the contrast within the thalamus, as described in Chapter 5.

In preparation for scanning, the brains were removed from the formalin and the frontal cortex was cut off so that the brains fitted inside a 16cm spherical plastic shell. This shell was then sealed and filled with Fomblin (Solvay Solexis, Brussels, Belgium), which is a dense and inert mineral-oil-like substance containing no ^{1}H atoms. This caused any remaining formalin or blood to float to the top and this was then removed. Fomblin was used instead of agar since Fomblin does not produce an MR signal so the brain image can easily be extracted. Another disadvantage of agar is that once it has set, any air bubbles trapped in the middle of the brain generate susceptibility artefacts. With Fomblin, the air bubbles can be removed by inverting the brain and allowing the bubbles to float up through the ventricles. However, Fomblin does not mechanically stabilize the sample so sponge blocks were inserted around the brain in order to fix it in position.

Temperature-controlled Scanning

After tissue preparation (Brain 2, Table 4.1), the sphere was placed in a refrigerator overnight to cool to 5^{o}C. The circulator was used to heat and cool the water surrounding the sphere to stabilise the temperature of the tissue in 5^{o}C increments, up to about 30^{o}C. The brains were scanned in the circulator with low-resolution multi GE (1.7x1.7x1.7mm^3 voxel, TE_1= 4ms, ΔTE=4ms, 10 echoes) and T_1 inversion recovery

	Brain 1	Brain 2
ID	15D44378	15D21736
Period between death and PM	2-3 days	1 day
Date of postmortem	25/08/15	14/05/15
Age at death	41	56
Sex	M	M
Diagnosis	Epilepsy	Trauma
Section scanned	whole	whole
Fixation Period (months)		
3	20/11/15 (high res) 23/11/15 (high res in circulator)	
7		7/12/15 (high res)
11	27/7/16 (6 temps)	
15		6/8/16 (6 temps) 7/8/16 (high res)

Table 4.1: Properties of brains used for temperature-dependent scanning.

(1.25x1.125x1.25mm^3 voxel, with 7 TI values in the range 153-1652ms) sequences at a range of temperatures from 5°C to 31°C. A fibre optic thermometer was inserted into the sample with the tip approximately 1cm from the edge of the brain.

The voxel intensities of the multi GE images were fitted to produce R_2* maps and QSM was performed using the STI Suite package (Brain Imaging and Analysis Center, Duke University). 2D ROIs were selected on chosen slices across a range of brain regions and the R_2* and QSM values within the ROIs were averaged.

In order to calculate the susceptibility maps, the phase was first unwrapped and then filtered using the V-SHARP (variable Sophisticated Harmonic Artefact Reduction for Phase data) filter [26] to remove phase variation due to background sources, such as air-tissue boundaries. The V-SHARP filter works by using the fact that the fields from external sources are harmonic, whereas those from internal sources are not. This means that the background fields are unchanged after convolution with a radially symmetric function and can consequently be subtracted [26]. The resulting difference maps are deconvolved to leave the internal fields. The unwrapped and filtered phase was used to calculate the field perturbations. Finally, the data was inverted using the iLSQR method, to obtain the quantitative susceptibility maps.

The R_1 values were calculated by fitting to the intensity levels per voxel only within the ROI. These values were then plotted as a function of temperature. Areas of high iron concentration, grey matter and white matter were compared with each other and with the ferritin phantom.

4.2.3 Longitudinal Effects of Fixation

	Brain 3
ID	16D37005
Period between death and PM	9 days
Date of postmortem	17/08/16 (1 year consent)
Age at death	82
Sex	F
Diagnosis	dementia -pulmonary embolism
Section scanned	right
Fixation Period (months)	
1	09/09/16 (scan 1)
3	16/11/16 (scan 2)
6	25/02/16 (scan 3)
12	16/08/16 (scan 4)

Table 4.2: Properties of brain used in longitudinal fixation study.

To investigate the effects of fixation on iron content and distribution, Brain 3 (Table 4.2) was obtained with consent by the family and coroner for use in research for 1 year, as consent is normally limited to 6 months. The brain was placed in formalin and was divided into halves after 1 month. One half was then placed on a flat agar surface in a spherical container and surrounded with Fomblin. This was scanned using a 7T Philips MRI scanner, 1, 3, 6 and 12 months after fixation with high resolution gradient echo (GE) (FOV= 192x160x80mm^3, 0.33x0.33x0.33mm^3, TE_1= 20ms, FA= 17, NSA= 4, scan time= 5 hours), multi-echo GE (FOV= 192x161x80mm^3, 0.6x0.6x0.6mm^3, TE= 9.1ms, ΔTE= TE_1, 5 echoes, FA= 25, scan time= 2 hours, NSA= 4) and inversion recovery sequences (FOV= 200x181x80mm^3, 0.6x0.6x0.6mm^3, TI= [250, 350, 530, 700, 900, 1600, 2100]ms, FA= 8, scan time= 4 hours, NSA= 4).

The multi gradient echo images where all registered to the 1 month scan, using FMRIB's Linear Image Registration Tool (FLIRT) [27, 28] from the FMRIB Software Library (FSL- Oxford centre for Functional MRI of the Brain, University of Oxford). R_2* maps were then calculated in Matlab. The high resolution gradient echo image data was used to calculate susceptibility maps using STI Suite and the inversion recovery images were fitted to calculate R_1 maps using NeuRoi (Clinical Neurology, School of Medicine, The University of Nottingham) which were then registered to the 1 month scan. ROIs were selected across a range of regions and the MR parameters were averaged and compared between iron-rich, grey matter and white matter regions.

During registration of the images between fixation periods, it was noticed that the final image appeared smaller than in the previous scans. A threshold was applied to the unregistered images to obtain a mask of the brain tissue. The images were manually masked to exclude the agar and droplets of formalin as they were included in the threshold mask as they had voxel intensities greater than the tissue. The tissue volume was calculated by summing the number of voxels within the mask.

4.3 Results and Discussion

The behaviour of the R_1, R_2* and susceptibility values are presented for a range of ferritin concentrations in an agar phantom. These are then compared to the temperature-controlled scanning of a post-mortem brain. Finally, the effects of fixation time on the MR imaging of post-mortem tissue are described.

4.3.1 Temperature Dependence

Circulator Efficiency

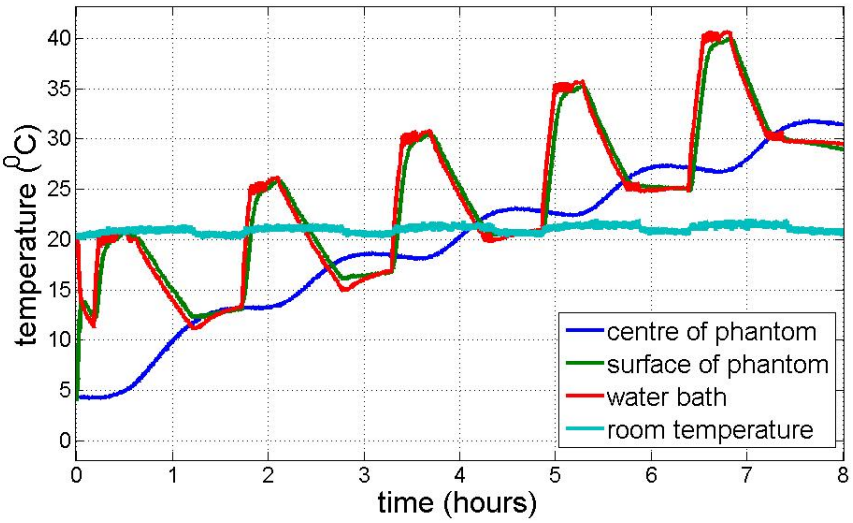

Figure 4.4: Heating curves used to calibrate temperature for warming phantom in 5° steps, for a 12cm-diameter agar phantom in a perspex sphere.

Figure 4.4 shows that the circulator took approximately an hour to increase and stabilise the temperature for 5°C increments, for a 12cm-diameter agar phantom in a perspex sphere. The temperature measurements from four fibre-optic probes are shown, which were placed in the centre and the surface of the phantom, and placed in the water bath and in the scanner room, to measure the temperature gradients across the different interfaces. The rate of cooling was lower below room temperature and lowest for the first temperature step. Similarly, the rate of heating was lower above room temperature and lowest for the last temperature step. This is partially due to heat being exchanged with the surroundings and also due to the larger amount of power required to achieve the same rate of thermal exchange between the compressor and surrounding air. Overall the rate of heating was greater than the rate of cooling. For this reason the temperature was incremented rather than decremented in our study. To further improve efficiency, the sample and sample holder were left in the fridge over night to cool down to approximately 5°C for the initial temperature measurement.

Figure 4.4 also shows a small lag between the temperature of the water bath and the surface of the phantom, but a much larger lag of approximately an hour between the water bath and the centre of the phantom. In subsequent work, the heated water from

the water bath was therefore pumped directly into the holder to reduce the number of layers and to increase the rate of heat transfer. Transitioning between temperature steps produced a temperature gradient across the phantom dependent on the distance from the surface. For this reason, additional time is required for the temperature to equilibrate, which was not always feasible in the time given.

Factors affecting the rate of heat exchange were considered, such as the surface area to volume ratio, since a smaller sphere would have a larger surface area to volume ratio to transfer heat. The phantom medium would also dictate the process of heat transfer. In a solid, the heat would be transferred via conduction whereas it would be transferred by convection in a liquid medium. However the rate would also be affected by the thermal conductivity of the medium.

Ferritin Phantom

With respect to increasing iron concentration, Figure 4.5a shows susceptibility values increase linearly, with a constant of proportionality of 0.45$\pm$0.07ppm per mg Fe per gram agar at 22^{o}C. R_2* (Figure 4.5b) and R_1 (Figure 4.5c) values also increased with increasing iron concentration. The susceptibility and R_1 values at each iron concentration are highest for the 4.9^{o}C measurements and descend in order with increasing temperature. On the other hand, the R_2* values at each iron concentration are lowest for the 4.9^{o}C measurements and ascend in order, with some overlap, with increasing temperature. These were linearly fitted to calculate the gradient of the susceptibility with iron concentration and R_1 and R_2* relaxivities, which were plotted against inverse temperature, in Figure 4.6.

Figure 4.5d shows that the susceptibility of each cylinder decreased with increasing temperature, with the susceptibility of the sample containing the highest concentration of ferritin changing by 12$\%$ over the temperature range. Figure 4.5e shows that R_2* increased more significantly with temperature for lower concentrations, due to the effect of diffusion on R_2* dominating the reduction in R_2* caused by the susceptibility change. The susceptibility decreases more for higher concentrations, resulting in a smaller change in R_2* over the temperature range. Figure 4.5f shows that R_1 for the ferritin samples decreased systematically with increasing temperature. In ferritin-doped agar, R_1 and R_2* are both sensitive to the magnetic susceptibility effects of iron.

In Figure 4.5e, the R_2* of the undoped agar (shown with purple crosses) around the tubes was found to increase with temperature at a rate of 0.15$\pm$0.03 $s^{-1}K^{-1}$, with a similar increase found over multiple ROIs. R_1 for the undoped agar (shown with purple crosses) decreased systematically with increasing temperature, at a rate of -0.009 $\pm$0.002 $s^{-1}K^{-1}$, as shown in Figure 4.5f. Phantoms and support platforms for post-mortem samples are usually made from agar and this study confirms previous work that showed that the R_1 of the agar decreases with temperature [29] and showed that the R_2* of the agar increased with temperature [11].

Figure 4.6a shows that the gradient of the susceptibility variation with iron concentration, increased approximately linearly with the inverse of the temperature [6], with a

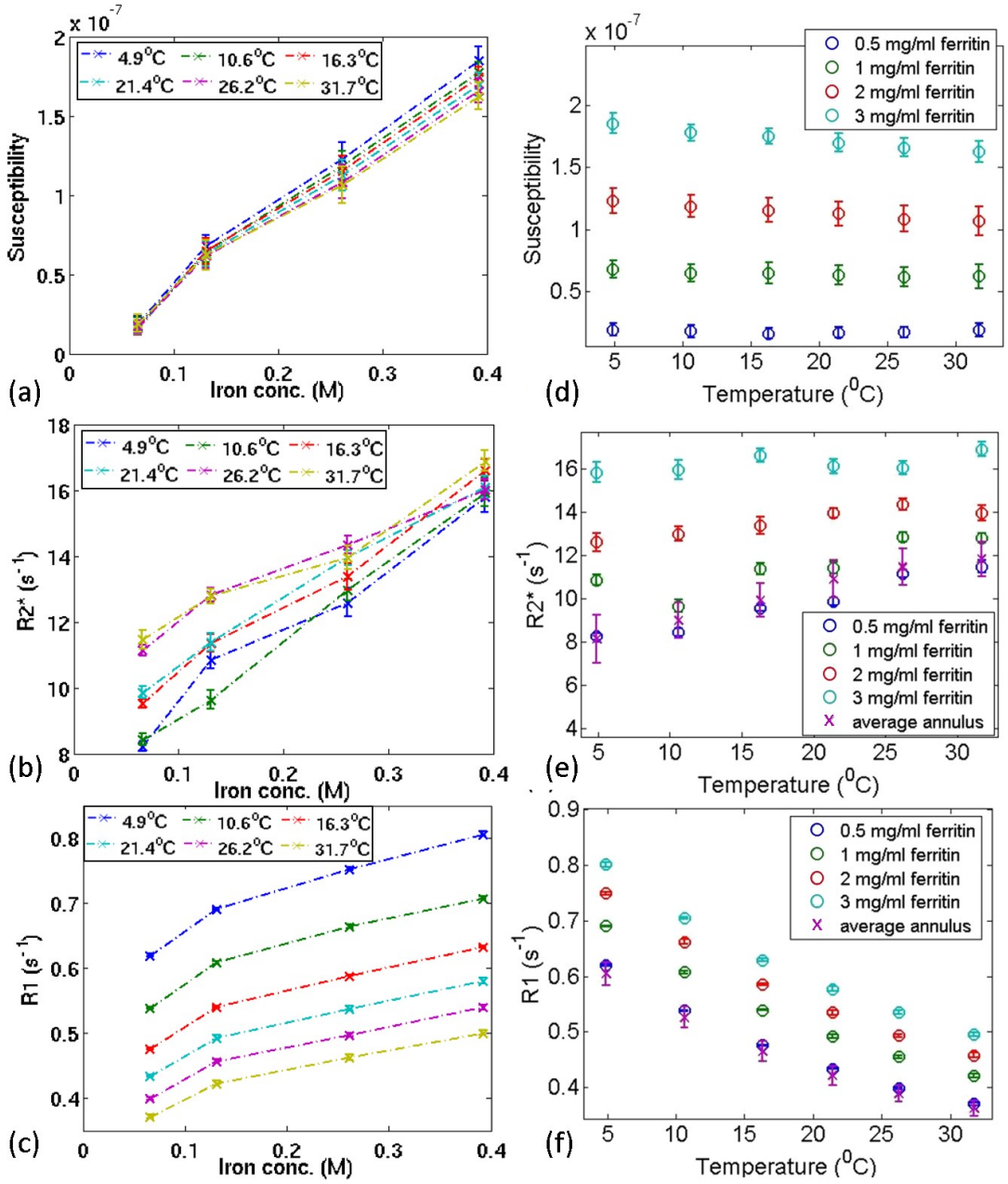

Figure 4.5: (a) Susceptibility, (b) R_2* and (c) R_1 variation with iron concentration, across the temperature range 4.9-31.7^{o}C. (d) Susceptibility, (e) R_2* and (f) R_1 variation with temperature in cylinders doped with different ferritin concentrations, and in surrounding agar.

correlation coefficient of 0.012$\pm$0.002 K M^{-1}. Ferritin contains a superparamagnetic core whose average magnetization has a linear dependence on inverse temperature over the temperature range studied here [23], as confirmed by the results in Figure 4.6a. In Figure 4.6b, the R_2* relaxivity increases with inverse temperature, nearly doubling as the temperature decreased from 32 to 5^{o}C, with a correlation coefficient of $(1\pm1)\times10^6$ K M^{-1}s^{-1}. This significant increase may be explained by the additional temperature sensitivity of water diffusion rates, caused by the increase in the correlation time of the samples, as the temperature increased. Ferritin-induced R_1 relaxivity clearly in-

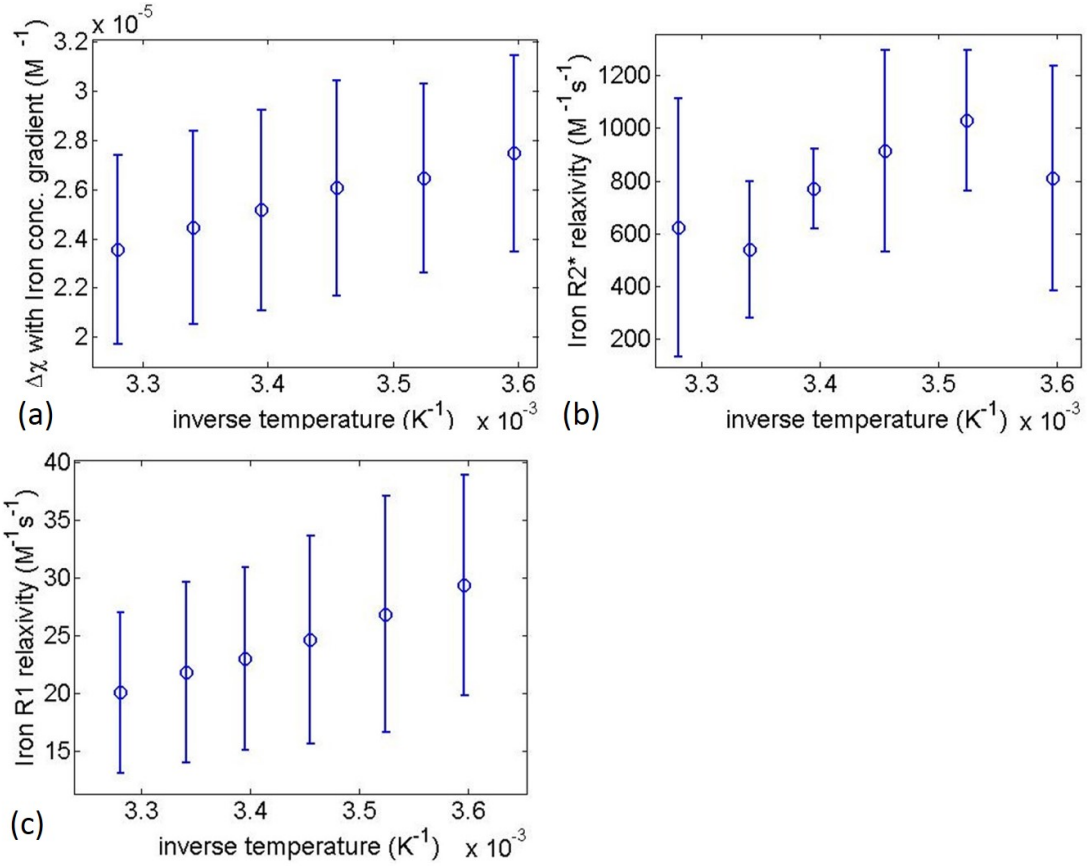

Figure 4.6: Gradients of (a) susceptibility (b) R_2* and (c) R_1 values from Figure 4.5 against ferritin concentration, resulting in plots of relaxivity against inverse of temperature.

creased with the inverse of the temperature (Figure 4.6c), with a correlation coefficient of $(2.9\pm0.3)\times10^4$ K $M^{-1}s^{-1}$, but there were significant errors in the fitting of the susceptibility, R_1 and R_2* with iron concentration, in part due to the small number of different concentrations considered and temperature variation across the phantom. Furthermore, the relaxation rates and susceptibility do not follow a clear linear variation with iron concentration (Figure 4.5a-c). However all of the fits showed a clear increasing trend with inverse temperature.

The main limitation of the temperature-controlled scanning is that a temperature gradient is produced across the ferritin phantom as the edges are heated and cooled to warm the centre of the sample. A significant amount of time was required to increment and equilibrate the temperature of the phantom, to reduce the uncertainty in the measured difference of R_1, R_2* and susceptibility values with temperature.

Post-mortem brain samples

Figure 4.7 shows T_2*-weighted gradient echo images for Brain 2. This brain was subjected to trauma before death, and haemorrhages can be seen in the lateral and posterior sections of the cortex. The ROIs used to calculate the average R_1, R_2* and suscep-

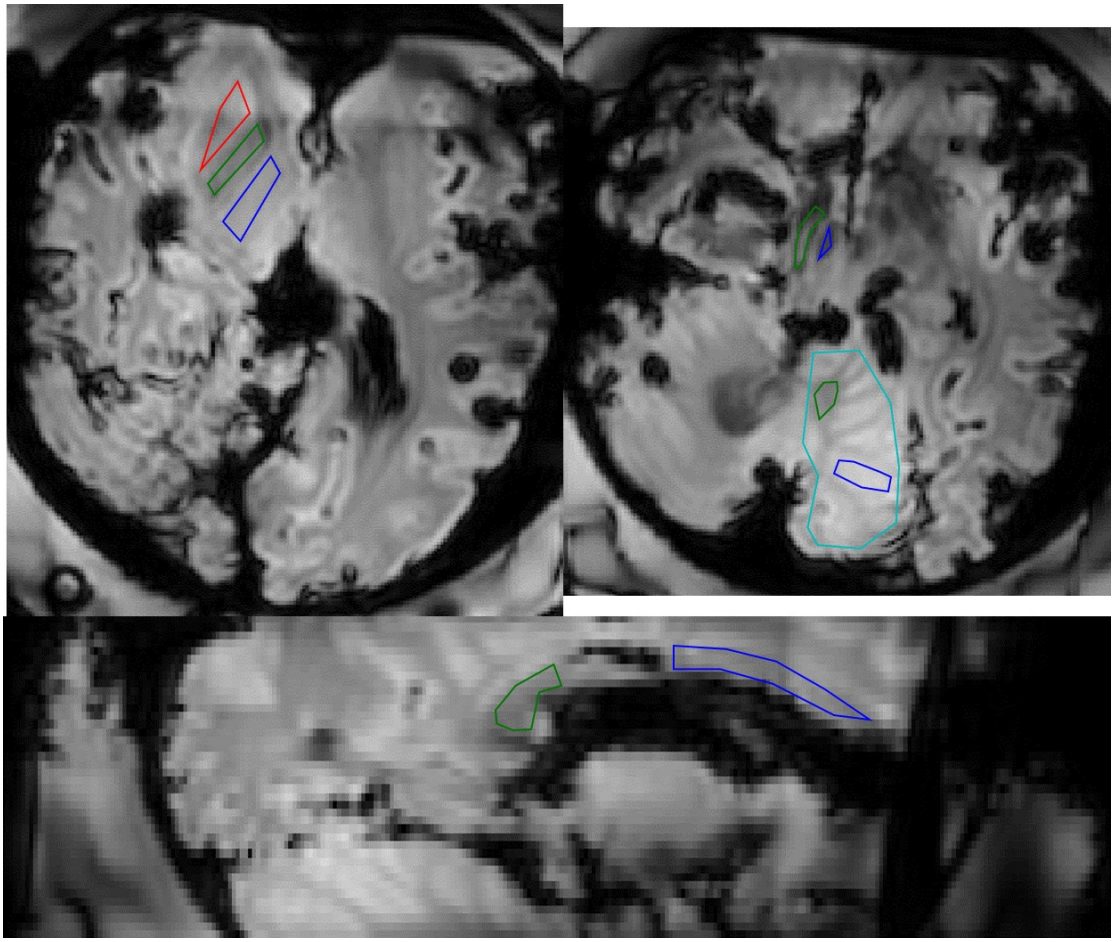

Figure 4.7: T_2*-weighted GE magnitude images with (top left) ROIs for thalamus (blue), globus pallidus (green) and putamen (red). Top right: ROIs for red nucleus (blue), substantia nigra (green), white matter (blue) and grey matter (green) in cerebellum and whole cerebellum (turquoise). Bottom: ROIs for intermediate (blue) and posterior (green) sections of corpus callosum.

tibility values across the basal ganglia, cerebellum and corpus callosum, are indicated with the colours that were then used for plotting variations. These regions were selected manually each time so the average values calculated would vary slightly from run to run.

Figure 4.8 shows QSM maps of the post-mortem brain acquired at different temperatures. The susceptibility values across the ROIs are plotted in Figure 4.9. These decrease with increasing temperature in the globus pallidus, cerebellum, thalamus, red nuclei and substantia nigra. The susceptibility values in ROIs in the putamen, cerebellum and corpus callosum remain approximately constant. This behaviour is due to the temperature dependence of the susceptibility of paramagnetic ferritin following Curie's law, where the susceptibility decreases with increasing temperature and the diamagnetic susceptibility of the myelin being independent of temperature. Unexpectedly, the susceptibility of the white matter of the cerebellum and corpus callosum increased with temperature. This may be due to the way in which the effective zero value of susceptibility is set in QSM, by taking the average of the whole image as a reference, so if the average of the image decreases, then the susceptibility values of the predominantly

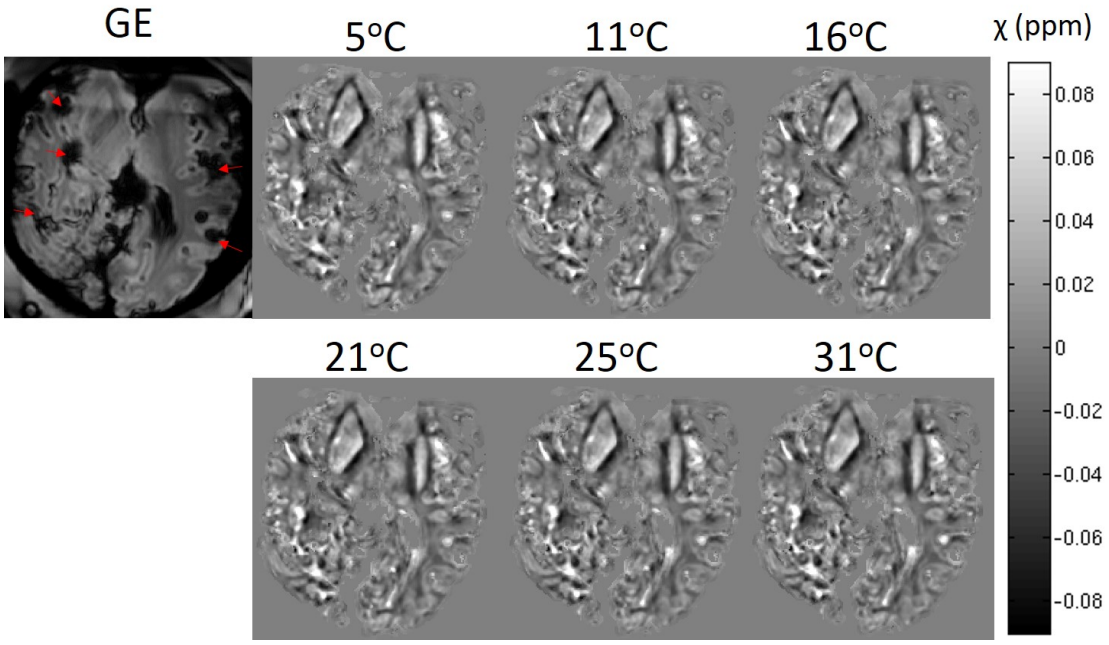

Figure 4.8: T_2*-weighted GE of Brain 2 which suffered trauma, indicated with red arrows. QSM maps of Brain 2 acquired at different temperatures.

white matter regions would increase relatively. Ideally, a region with known susceptibility should be used as the reference, such as CSF. The globus pallidus has the highest susceptibility values, as expected as it has the highest iron concentration (213 μg/g wet weight [21]), followed by the red nuclei, substantia nigra (185 μg/g wet weight [21]), putamen (130 μg/g wet weight [21]), cerebellum (whole), thalamus and corpus callosum (15 μg/g wet weight [20]).

Compared to the ferritin phantom in which the susceptibility values of each cylinder decreased with increasing temperature, changing by 12% for the highest concentration, the susceptibility values of the globus pallidus also decreased by 11% with increasing temperature. The iron concentration of the globus pallidus was expected to be slightly lower than that of the phantom (213μg/g wet weight compared to 392μg/ml agar) but the susceptibility values were an order of magnitude smaller, possibly due to the use of the different references for calculating the susceptibility difference. This is a major limitation of the susceptibility value measurement, as it is a difference rather than an absolute value.

Figure 4.10 shows a gradient echo image and R_2* maps acquired at different temperatures with the brain in the plastic sphere within the circulator. The temperature variation of the R_2* values measured in the basal ganglia, cerebellum and corpus callosum are plotted in Figure 4.11. The R_2* values of the globus pallidus, putamen and grey matter in the cerebellum decrease significantly with increasing temperature, whereas the R_2* values of the predominantly white matter regions of the cerebellum and corpus callosum along with the thalamus remain approximately constant. Again, this is due to the susceptibility of the paramagnetic ferritin following Curie's law and the diamagnetic susceptibility of the myelin being independent of temperature. Therefore, since the de-

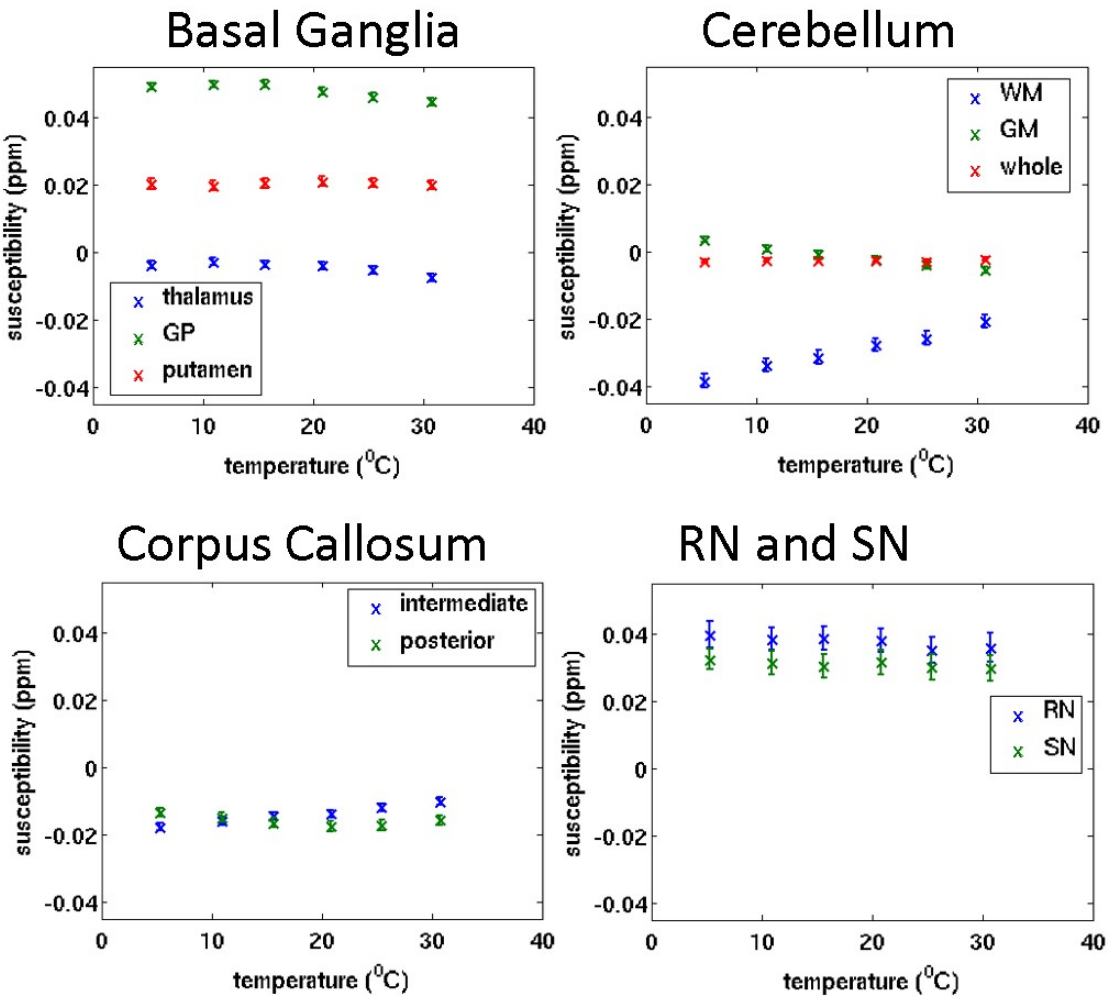

Figure 4.9: Average susceptibility value in ROIs across the basal ganglia, cerebellum and corpus callosum against temperature.

phasing decreases, R_2* also decreases with increasing temperature.

The substantia nigra has the highest R_2* values (shortest T_2*), followed by the globus pallidus, putamen and white matter structures. The R_2* values of the posterior and intermediate body of the corpus callosum are greater and less than the thalamus, respectively. The R_2* values of the red nuclei and the substantia nigra are similar, as expected. The R_2* values of the substantia nigra are higher than the globus pallidus, even though the globus pallidus is expected to have the highest iron concentration of 213μg/g ww compared to 185μg/g ww), as shown in Figure 4.11. This is possibly due to additional dephasing around small structure such as the substantia nigra, rather than iron concentration

In contrast to the ferritin phantom, which contained iron concentrations of up to 392μg/ml, for which the R_2* values increased with temperature for lower iron concentrations, the R_2* values in the post-mortem brain decreased with temperature, particularly in regions with higher iron concentration. In agar, this is most likely due to the increase in dif-

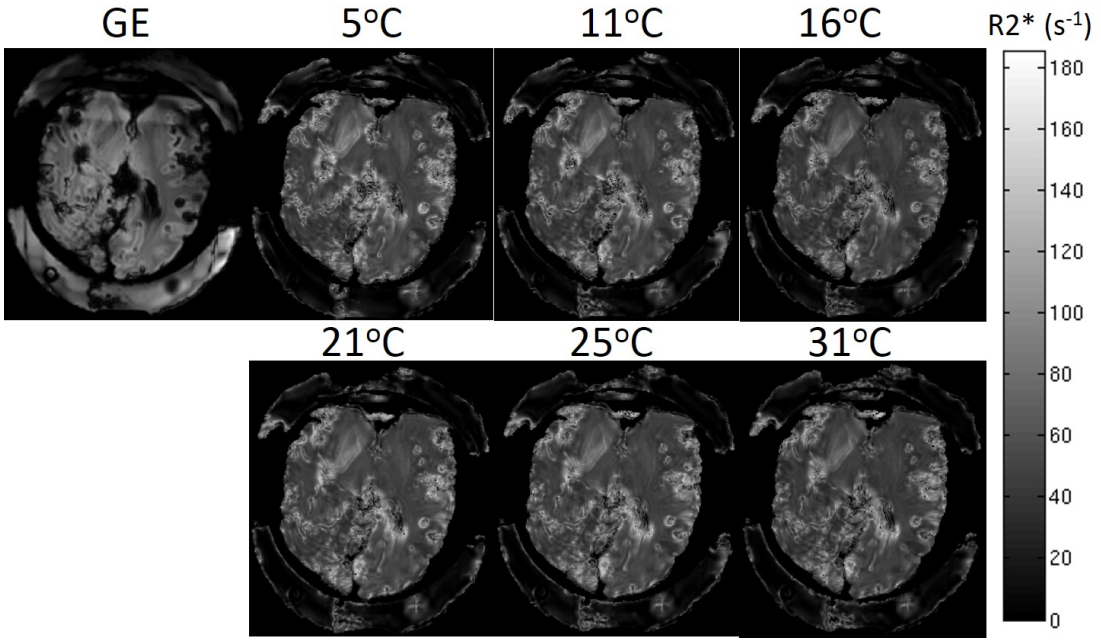

Figure 4.10: T_2* weighted image and R_2* maps acquired at different temperatures, for Brain 2, which suffered trauma.

fusion rate dominating the reduction in susceptibility, with increasing temperature. On the other hand, diffusion in the post-mortem tissue is restricted by the cellular structure, thus the change in susceptibility dominates the change in diffusion rate. Also, the R_2* values were approximately an order of magnitude greater in the post-mortem brain than in the ferritin phantom, as expected.

Figure 4.12 shows an inversion recovery (TI=527ms) image of Brain 2 inside the circulator. This image shows the effects of B_1 field inhomogeneities due to the large volume of water surrounding the brain. Also shown are R_1 maps of the post-mortem brain, acquired at different temperatures. The temperature variation of the R_1 values measured in the basal ganglia, cerebellum and corpus callosum are plotted in Figure 4.13. The R_1 values of the thalamus, globus pallidus, putamen, grey matter of the cerebellum and the substantia nigra decreased with increasing temperature. The R_1 values of the red nuclei remained approximately constant, but the R_1 values of the white matter regions increased with temperature possibly due to degradation of the tissue or poor ROI selection.

The thalamus showed the largest change in R_1 values and the largest R_1 values, followed by the globus pallidus, putamen, substantia nigra and cerebellum. The R_1 values of the intermediate and posterior body of the corpus callosum are similar to values measured in the cerebellum, as they have similar compositions and distances to the edge of the tissue. Additionally, the large R_1 values of the regions close to the edge of the tissue are likely due to the strong effect of fixation, as cross-links between proteins are formed.

Compared to the ferritin phantom, where the R_1 values of the doped cylinders and surrounding agar decreased with increasing temperature, the post-mortem R_1 values also

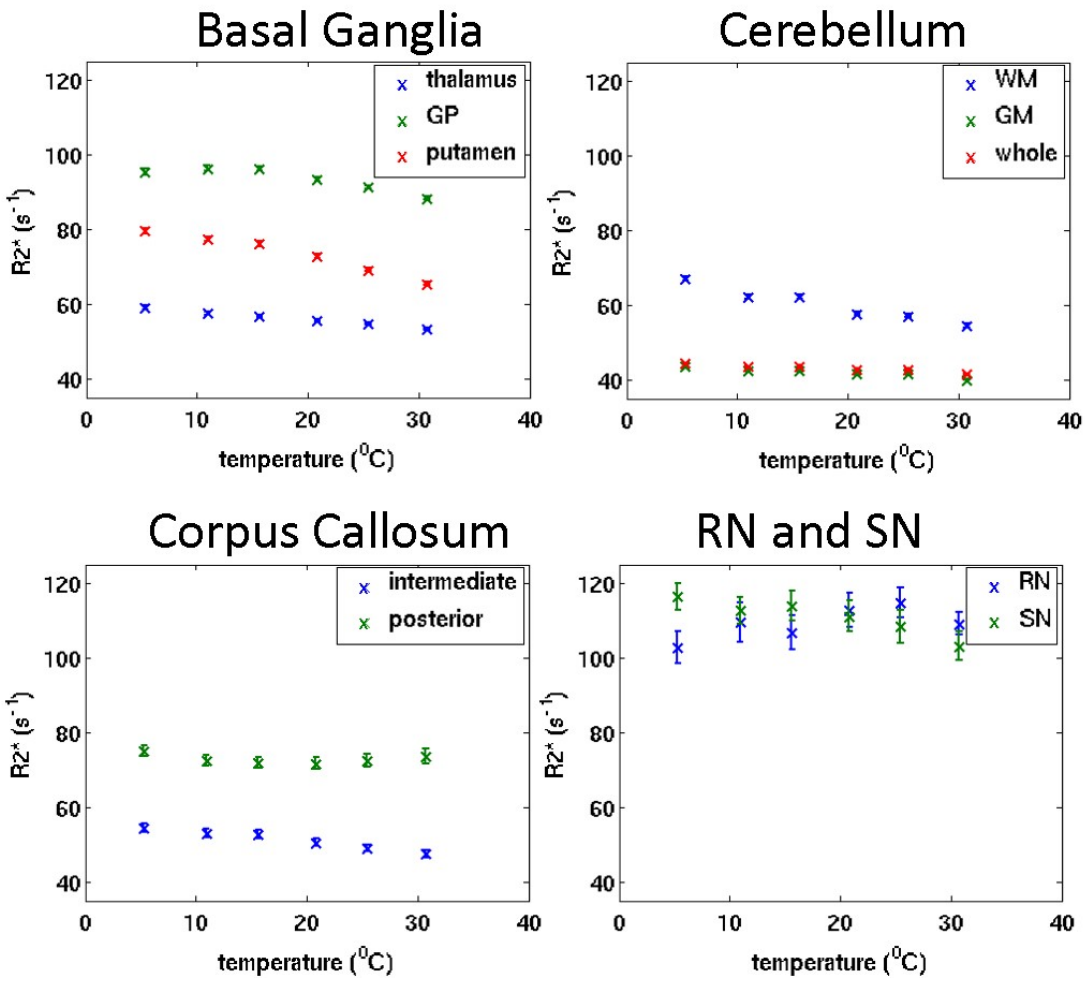

Figure 4.11: Average R_2* value in ROIs across the basal ganglia, cerebellum and corpus callosum against temperature.

decreased with temperature, but are approximately an order of magnitude larger in the post-mortem brain than in the agar phantom. This is due to the restrictive structure of tissue shortening the T_1 time, i.e. increasing the R_1 time of water.

Similar problems arose for the post-mortem brain as for the ferritin phantom. The time taken for the temperature to equilibrate was longer for the post-mortem brain as the sphere that the brain was contained in was bigger than the sphere for the ferritin phantom. This also resulted in larger inaccuracies in the estimation of the temperature in different ROIs as they were different distances from the surface. Also, the effects of temperature change are in addition to the effects of fixation, for 15 months, although this was kept constant. Due to the low resolution of the images, the boundaries between regions are not clear, which made the placement of ROIs more variable. Finally, the thermal expansion of water was considered, but the volume increases by 0.6% from 4 to 30°C. This could affect the volume susceptibility, but is a small change compared to the range over which the susceptibility changes as a function of temperature.

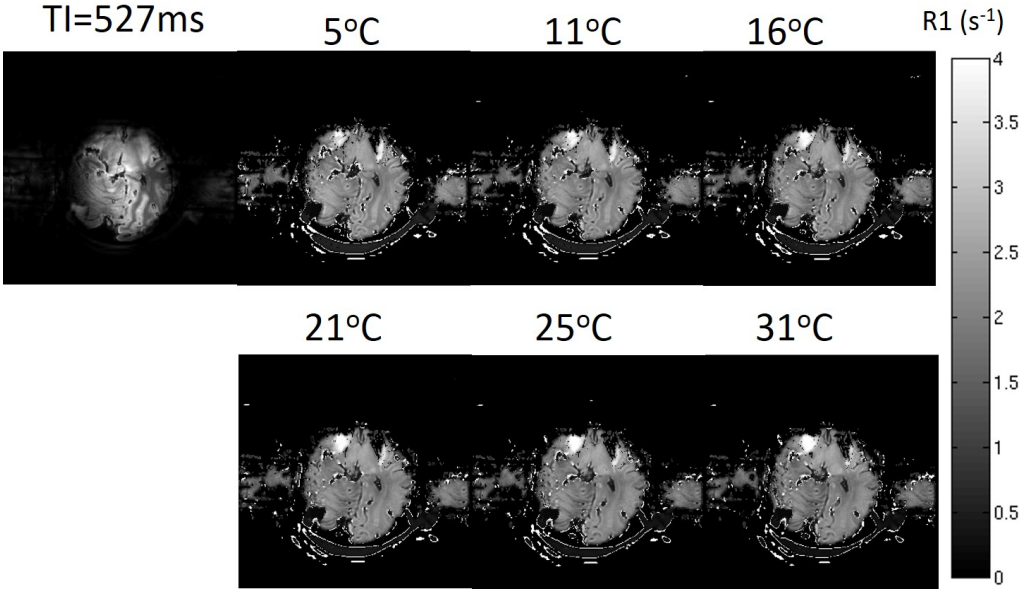

Figure 4.12: Magnitude inversion recovery image acquired with an inversion time of 527ms, of Brain 2 which suffered trauma. R_1 maps of Brain 2 with varying temperature.

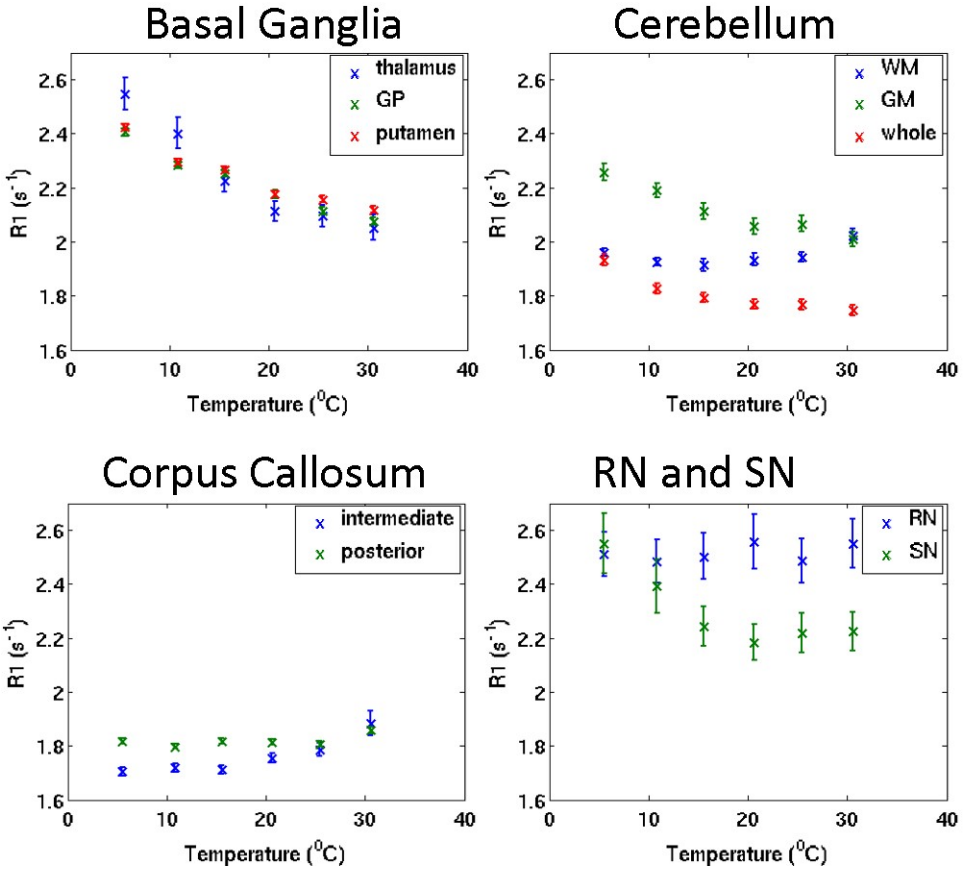

Figure 4.13: Average R_1 value in ROIs across the basal ganglia, cerebellum and corpus callosum against temperature.

4.3.2 Longitudinal Effects of Fixation

Figure 4.14 shows that the volume of brain tissue decreased linearly over 12 months of fixation at a rate of 2.9±1.6 cm^3/month. This is likely to be caused by the cross-linkage of proteins that is driven by the formaldehyde, but may also be due to the loss of water as iron and other solutes are leached into the formalin. The decrease in tissue volume is significant and its effect on the R_1, R_2* and susceptibility values will be considered.

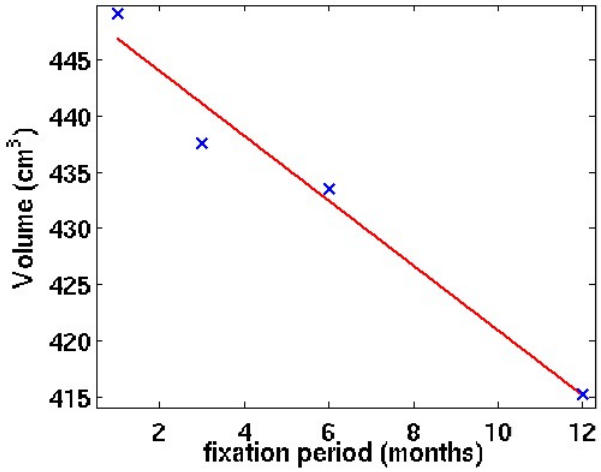

Figure 4.14: Volume of brain mask against fixation time.

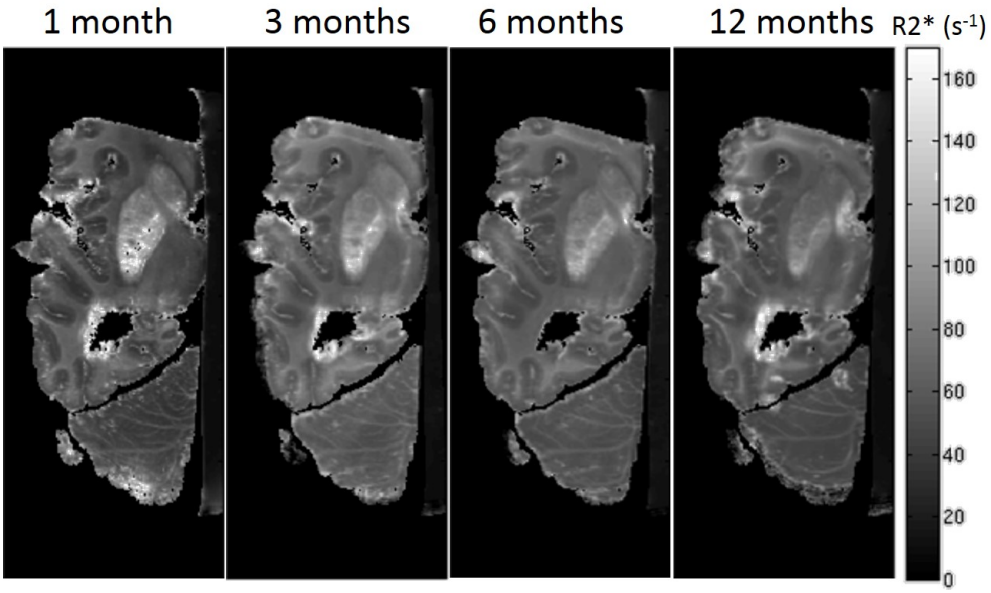

Figure 4.15: (Left to right) R_2* maps at 1, 3, 6 and 12 months of fixation.

Figure 4.15 shows R_2* maps acquired after 1, 3, 6 and 12 months of fixation. Areas of high iron content such as the globus pallidus and putamen become darker and regions of white matter become brighter with time. Figure 4.16 shows the ROIs used across the basal ganglia, cerebellum and corpus callosum. The variation of R_2* with fixation time

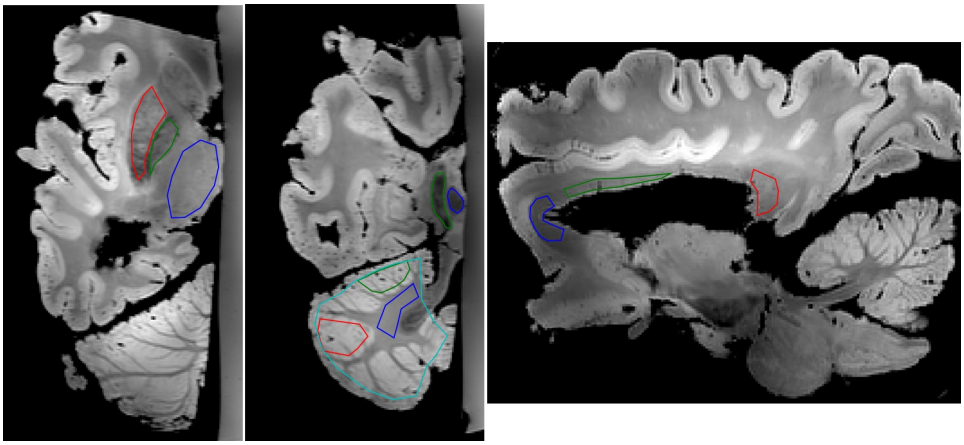

Figure 4.16: GE magnitude images with (left) ROIs for thalamus (blue), globus pallidus (red) and putamen(green). Centre: ROIs for red nucleus (blue), substantia nigra (green), white matter in cerebellum (blue), lateral (red) and central (green) grey matter regions in cerebellum and whole cerebellum (turquoise). Left: ROIs for anterior (blue), intermediate (green) and posterior (red) sections of corpus callosum.

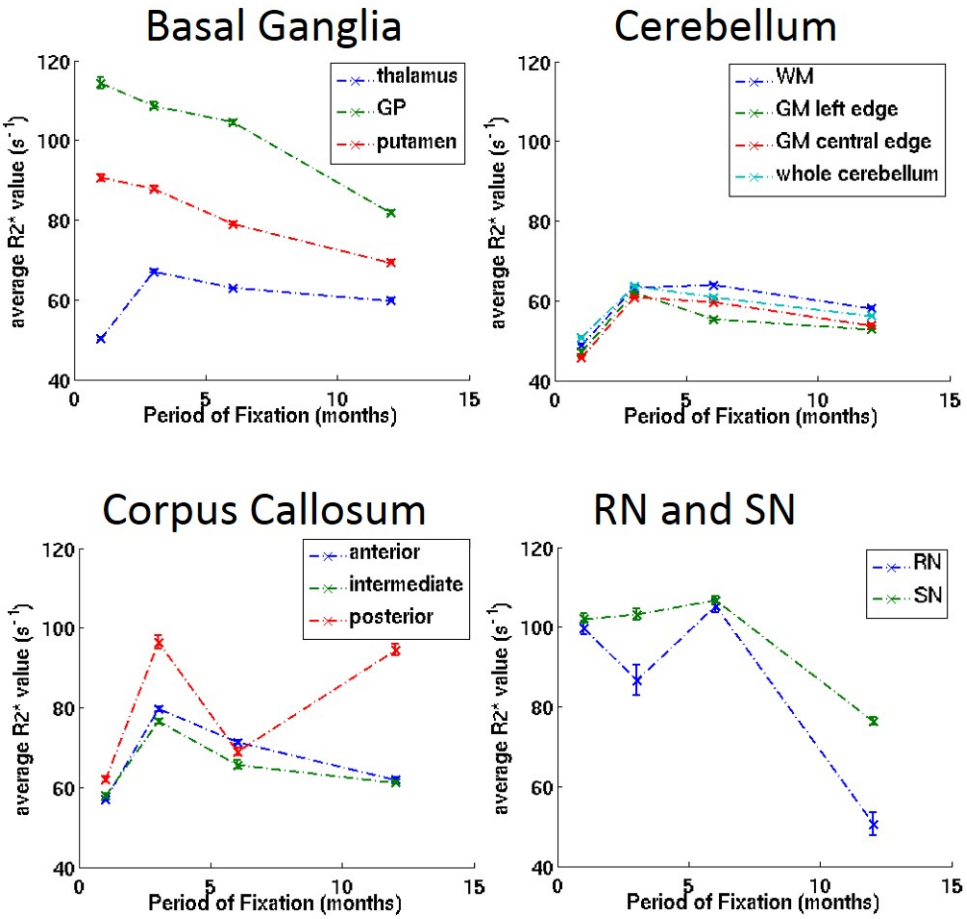

Figure 4.17: Average R_2* value in ROIs across basal ganglia, cerebellum and corpus callosum against fixation time.

in these ROIs is shown in Figure 4.17. Some regions increase in R_2* before decreasing, including the thalamus, cerebellum, corpus callosum, red nuclei and substantia nigra. These regions are very close to the edge of the brain, which is in direct contact with the formalin. Therefore, the R_2* change with time is also dependent on the distance to the edge of the tissue, as the formalin takes time to diffuse through the tissue.

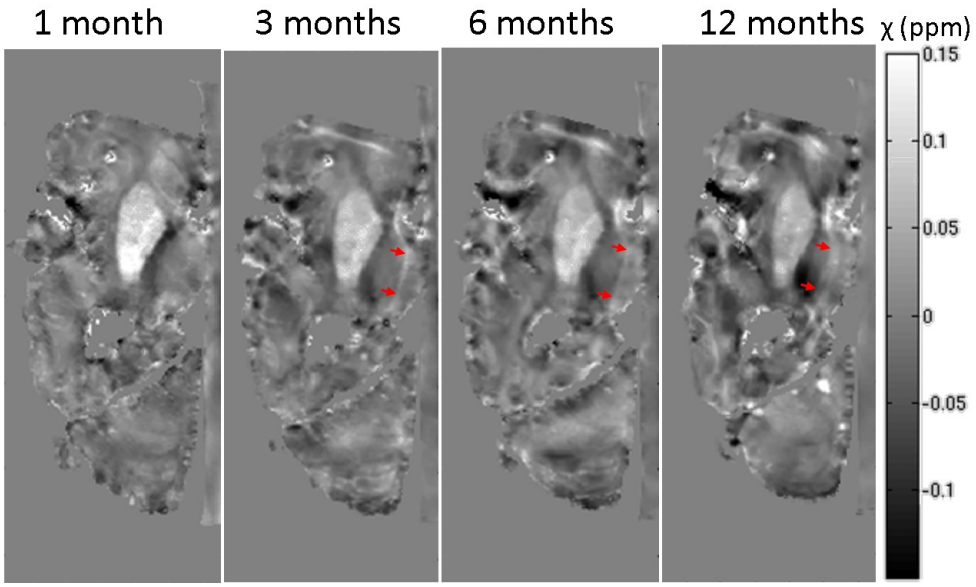

Figure 4.18: (Left to right) QSM maps at 1, 3, 6 and 12 months of fixation.

Figure 4.18 shows QSM data acquired over 1 to 12 months of fixation. Again the globus pallidus and putamen become darker with time as the iron is leached from these regions. The diffusion front of the formalin is visible as it moves through the thalamus (red arrows). Figure 4.19 shows a similar trend to the R_2* values. There is a smaller increase in susceptibility values of the white matter, but there is a large decrease in the grey matter of the cerebellum at 6 months as the formalin diffusion front passes. The decrease of the susceptibility values is likely dominated by leaching of iron into the formalin, as the decrease in brain volume would have the opposite effect.

Figure 4.20 shows the R_1 maps acquired over 1 to 12 months of fixation. These become noticeably brighter with time. The diffusion front of the formalin is clear around all of the edges of the tissue. It takes approximately the whole 12 months for the diffusion front to reach the centre of the brain hemisphere. Figure 4.21 also shows that the R_1 values increased consistently across the basal ganglia, cerebellum, red nuclei and substantia nigra. The R_1 values of the intermediate section of the corpus callosum decrease at 6 months and then continue to increase. The increase in R_1 is caused by the cross-linking of proteins in the tissue as the mobility of the water molecules is reduced.

Effective fixation time is dependent on the distance from the surface of the tissue. It is known that fresh tissue undergoes a colour change after a few days of fixation in formalin, but the R_1, R_2* and QSM maps clearly show that tissue which visually appears to be fixed is still undergoing chemical changes and the fixation process takes much more

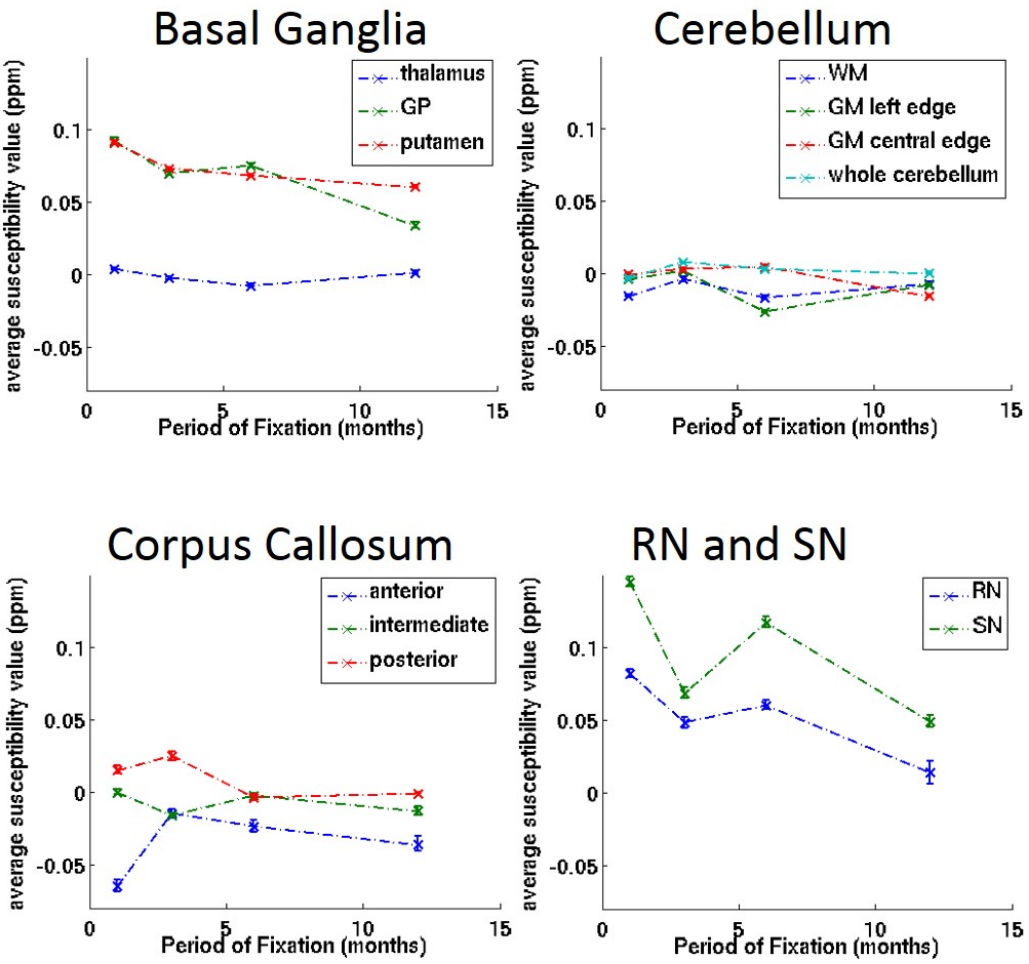

Figure 4.19: Average susceptibility value in ROIs across basal ganglia, cerebellum and corpus callosum against fixation time.

than a few days to complete, around 6 to 12 months depending on the size of the sample [10]. In support of these results, the R_1, R_2* and susceptibility values of Brain 2 (15 months fixation) with temperature controlled imaging, in Figures 4.8-4.13, are consistent with the values measured at 12 months of fixation for Brain 3, in Figures 4.15-4.21.

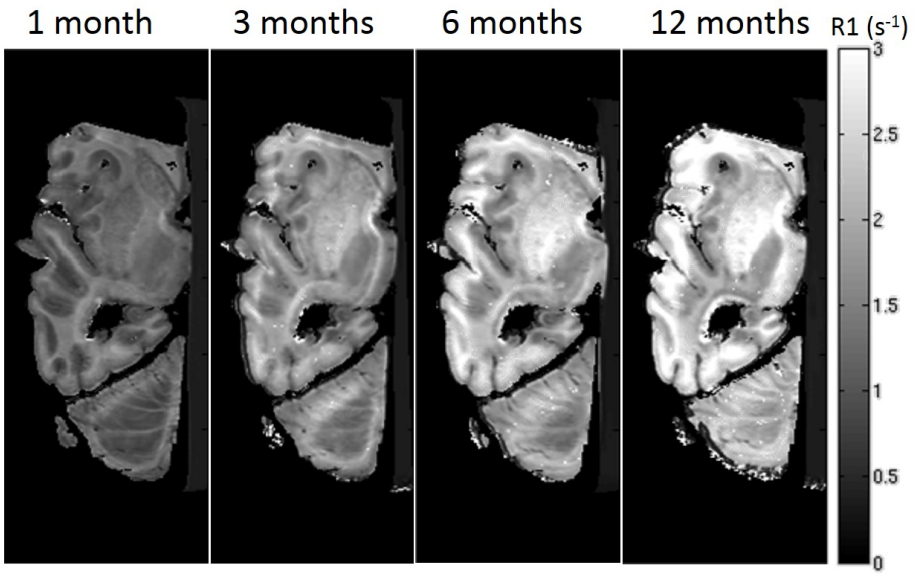

Figure 4.20: (Left to right) R_1 maps at 1, 3, 6 and 12 months of fixation.

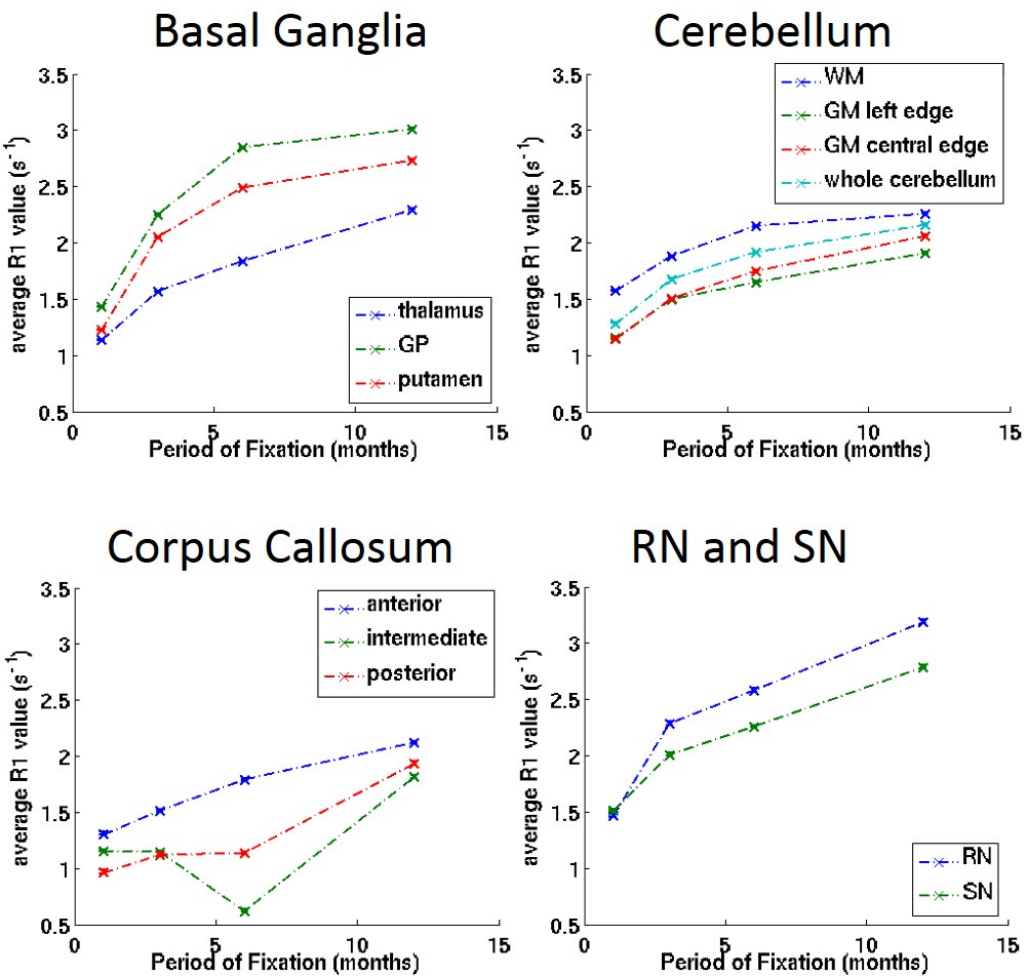

Figure 4.21: Average R_1 value in ROIs across basal ganglia, cerebellum and corpus callosum against fixation time.

4.4 Conclusion

A circulator was designed, built and tested to enable temperature-controlled scanning. The efficiency of the circulator was restricted by the rate of heat transfer to the centre of the sample, which depended on the size and composition of the sample itself. It was noted that temperature gradients needed to be considered during temperature-controlled scanning.

The effect of temperature on the MR parameters of a ferritin phantom and post-mortem brain were investigated. The magnetic susceptibility of the agar cylinder with the largest ferritin concentration was 12% higher at 5°C compared to 32°C. The R1 and R_2* values changed much more significantly over this temperature range as R_2* increased and R_1 decreased. For the post-mortem tissue, the R_1, R_2* and susceptibility values all decreased with increasing temperature, due to the reduction in the susceptibility of iron dominating the effect of the increased rate of diffusion of water. However, the post-mortem tissue has a lower susceptibility but greater R_1 and R_2*. This could be due to agar having a more homogeneous consistency than brain tissue. The associated errors were larger in the post-mortem brain than in the agar phantom, due to temperature variations and the low resolution of the data which made it harder to identify the edges of each brain region.

For the temperature-dependent project, more time to equilibrate and more temperature probes could be used to measure the temperature of the tissue to obtain a better temperature uniformity. The measurements could be repeated during cooling to measure the lag in the temperature change and whether there is any hysteresis. The temperature could also be verified by using MR thermometry [30].

The effect of fixation and handling on post-mortem tissue was also investigated. During the longitudinal fixation of the post-mortem brain, the volume decreased by 2.9±1.6 cm^3/month. R_2* initially increased in some regions but overall decreased. The susceptibility followed a similar trend. R_1 increased overall, but dipped midway during the fixation period in a few regions and seamed to plateau at the end of the fixation period. These MR parameters are also dependent on distance from the edge of the tissue.

In a future longitudinal fixation study, scanning could be repeated more often during the first 6 months and samples could be taken from the other brain half, of cortical and deep grey and white matter. This would allow a comparison of the MR susceptibility values to a physical measurement of iron concentration, using inductively-coupled mass spectrometry (ICPMS). Fixed tissue could also be compared to fresh frozen tissue from another brain, by dividing, sectioning one half and following a similar scanning protocol as above. The other half would then be frozen for spectroscopic analysis. In this way, a comparison of iron distribution could be made with fixation time, between fresh and frozen tissue and would allow comparison of MR imaging with histology and spectroscopy.

In conclusion, comparisons of post-mortem MRI values with in vivo imaging is possible as long as the fixation time, temperature and other parameters are carefully considered.

Bibliography

[1] Sam Wharton, Andreas Schäfer, and Richard Bowtell. Susceptibility mapping in the human brain using threshold-based k-space division. *Magnetic Resonance in Medicine*, 63(5):1292–1304, 2010.

[2] Paraskevi Kosta, Maria I Argyropoulou, Sofia Markoula, and Spyridon Konitsiotis. MRI evaluation of the basal ganglia size and iron content in patients with parkinson's disease. *Journal of Neurology*, 253(1):26–32, 2006.

[3] WR Wayne Martin, Marguerite Wieler, and Myrlene Gee. Midbrain iron content in early Parkinson disease a potential biomarker of disease status. *Neurology*, 70(16 Part 2):1411–1417, 2008.

[4] Adolf Pfefferbaum, Elfar Adalsteinsson, Torsten Rohlfing, and Edith V Sullivan. MRI estimates of brain iron concentration in normal aging: comparison of field-dependent (FDRI) and phase (SWI) methods. *Neuroimage*, 47(2):493–500, 2009.

[5] Masaki Fukunaga, Tie-Qiang Li, Peter van Gelderen, Jacco A de Zwart, Karin Shmueli, Bing Yao, Jongho Lee, Dragan Maric, Maria A Aronova, Guofeng Zhang, et al. Layer-specific variation of iron content in cerebral cortex as a source of MRI contrast. *Proceedings of the National Academy of Sciences*, 107(8):3834–3839, 2010.

[6] Christoph Birkl, Christian Langkammer, Heinz Krenn, Walter Goessler, Christina Ernst, Johannes Haybaeck, Rudolf Stollberger, Franz Fazekas, and Stefan Ropele. Iron mapping using the temperature dependency of the magnetic susceptibility. *Magnetic Resonance in Medicine*, 73(3):1282–1288, 2015.

[7] E Mark Haacke, Norman YC Cheng, Michael J House, Qiang Liu, Jaladhar Neelavalli, Robert J Ogg, Asadullah Khan, Muhammad Ayaz, Wolff Kirsch, and Andre Obenaus. Imaging iron stores in the brain using magnetic resonance imaging. *Magnetic Resonance Imaging*, 23(1):1–25, 2005.

[8] Weili Zheng, Helen Nichol, Saifeng Liu, Yu-Chung N Cheng, and E Mark Haacke. Measuring iron in the brain using quantitative susceptibility mapping and x-ray fluorescence imaging. *Neuroimage*, 78:68–74, 2013.

[9] Klaus Schmierer, Janet R Thavarajah, Shu F An, Sebastian Brandner, David H Miller, and Daniel J Tozer. Effects of formalin fixation on magnetic resonance indices in multiple sclerosis cortical gray matter. *Journal of Magnetic Resonance Imaging*, 32(5):1054–1060, 2010.

[10] Robert J Dawe, David A Bennett, Julie A Schneider, Sunil K Vasireddi, and Konstantinos Arfanakis. Postmortem MRI of human brain hemispheres: T2 relaxation times during formaldehyde fixation. *Magnetic Resonance in Medicine*, 61(4):810–818, 2009.

[11] Peter E Thelwall, Timothy M Shepherd, Greg J Stanisz, and Stephen J Blackband. Effects of temperature and aldehyde fixation on tissue water diffusion properties, studied in an erythrocyte ghost tissue model. *Magnetic Resonance in Medicine*, 56(2):282–289, 2006.

[12] Arushi Dugar, Michelle L Farley, Angeline L Wang, Mary B Goldring, Steven R Goldring, Bryan H Swaim, Benjamin E Bierbaum, Deborah Burstein, and Martha L Gray. The effect of paraformaldehyde fixation on the delayed gadolinium-enhanced MRI of cartilage (dgemric) measurement. *Journal of Orthopaedic Research*, 27(4):536–539, 2009.

[13] Charlotte J Yong-Hing, Andre Obenaus, Rodrick Stryker, Karen Tong, and Gordon E Sarty. Magnetic resonance imaging and mathematical modeling of progressive formalin fixation of the human brain. *Magnetic Resonance in Medicine*, 54(2):324–332, 2005.

[14] GRW Moore, E Leung, AL MacKay, IM Vavasour, KP Whittall, KS Cover, DKB Li, SA Hashimoto, J Oger, TJ Sprinkle, et al. A pathology-MRI study of the short-T2 component in formalin-fixed multiple sclerosis brain. *Neurology*, 55(10):1506–1510, 2000.

[15] David I Thickman, HL Kundel, and G Wolf. Nuclear magnetic resonance characteristics of fresh and fixed tissue: the effect of elapsed time. *Radiology*, 148(1):183–185, 1983.

[16] Yutong Liu, Balasrinivasa R Sajja, Howard E Gendelman, and Michael D Boska. Mouse brain fixation to preserve in vivo manganese enhancement for ex vivo manganese-enhanced MRI. *Journal of Magnetic Resonance Imaging*, 38(2):482–487, 2013.

[17] Wanida Chua-anusorn, John Webb, David J Macey, Pensri Pootrakul, and Timothy G St Pierre. The effect of histological processing on the form of iron in iron-loaded human tissues. *Biochimica et Biophysica Acta (BBA)-Molecular Basis of Disease*, 1360(3):255–261, 1997.

[18] John K Olynyk, K Rajender Reddy, Adrian M di Bisceglie, Lennox J Jeffers, Talley I Parker, Jason L Radick, Eugene R Schiff, and Bruce R Bacon. Hepatic iron concentration as a predictor of response to interferon alfa therapy in chronic hepatitis c. *Gastroenterology*, 108(4):1104–1109, 1995.

[19] Anna Wypijewska, Jolanta Galazka-Friedman, Erika R Bauminger, Zbigniew K Wszolek, Katherine J Schweitzer, Dennis W Dickson, Andrzej Jaklewicz, Danek Elbaum, and Andrzej Friedman. Iron and reactive oxygen species activity in Parkinsonian substantia nigra. *Parkinsonism & related disorders*, 16(5):329–333, 2010.

[20] LO Thomas, OB Boyko, DC Anthony, and PC Burger. MR detection of brain iron. *American Journal of Neuroradiology*, 14(5):1043–1048, 1993.

[21] B Hallgren and P Sourander. The effect of age on the non-haemin iron in the human brain. *Journal of Neurochemistry*, 3(1):41–51, 1958.

[22] YT Konttinen, V Bergroth, K Käyhkö, and S Reitamo. Human ferritin: effects of antigen source and fixation on leucocyte staining by immunoperoxidase technique. *Histochemistry*, 75(4):585–589, 1982.

[23] Rodney A Brooks, Josef Vymazal, Ron B Goldfarb, Jeff WM Bulte, and Phlip Aisen. Relaxometry and magnetometry of ferritin. *Magnetic Resonance in Medicine*, 40(2):227–235, 1998.

[24] Nicolaas Bloembergen, Edward Mills Purcell, and Robert V Pound. Relaxation effects in nuclear magnetic resonance absorption. *Physical Review*, 73(7):679, 1948.

[25] Panu T Vesanen, Koos CJ Zevenhoven, Jaakko O Nieminen, Juhani Dabek, Lauri T Parkkonen, and Risto J Ilmoniemi. Temperature dependence of relaxation times and temperature mapping in ultra-low-field MRI. *Journal of Magnetic Resonance*, 235:50–57, 2013.

[26] Ferdinand Schweser, Andreas Deistung, Berengar Wendel Lehr, and Jürgen Rainer Reichenbach. Quantitative imaging of intrinsic magnetic tissue properties using MRI signal phase: an approach to in vivo brain iron metabolism? *Neuroimage*, 54(4):2789–2807, 2011.

[27] Mark Jenkinson and Stephen Smith. A global optimisation method for robust affine registration of brain images. *Medical Image Analysis*, 5(2):143–156, 2001.

[28] Mark Jenkinson, Peter Bannister, Michael Brady, and Stephen Smith. Improved optimization for the robust and accurate linear registration and motion correction of brain images. *Neuroimage*, 17(2):825–841, 2002.

[29] R Vre, R Grimee, F Parmentier, and J Binet. The use of agar gel as a basic reference material for calibrating relaxation times and imaging parameters. *Magnetic Resonance in Medicine*, 2(2):176–179, 1985.

[30] Viola Rieke and Kim Butts Pauly. MR thermometry. *Journal of Magnetic Resonance Imaging: An Official Journal of the International Society for Magnetic Resonance in Medicine*, 27(2):376–390, 2008.

Chapter 5

Using ultra high field MRI to identify the nuclei of the human thalamus

5.1 Introduction

The thalamus is a crucial structure for multiple cognitive, motor and perceptual functions, as it combines information and regulates its transfer from sub-cortical regions to the cerebral cortex. This makes it an important target clinically and for research. It is composed of a series of independent functional nuclei. Several neurological disorders have been associated with thalamic abnormalities including Alzheimer's disease, Parkinson's disease and multiple sclerosis [1]. Thalamic regions are also increasingly being targeted for therapeutic intervention using deep brain stimulation [2]. The applications for in vivo thalamic nuclei delineation also include fMRI connectivity mapping of the thalamus in pain and other higher function studies and epilepsy. Understanding the structure and function of the thalamus is therefore of key importance.

The thalamic nuclei have been mapped with great detail, ex vivo. One of the most commonly used atlases of the thalamus is by Morel et al [3], derived from the immunohistochemistry of myelin (Cresyl Violet) and calcium binding proteins (parvalbumin, calbindin and calretinin stains) on 9 blocks across 5 brains to distinguish the boundaries of the nuclei. In MR images of the thalamus, the contrast is also affected by myelin and calcium [4].

More than fifty thalamic sub-regions have been identified via histological investigation, which is regarded as being the gold standard, but depiction of thalamic substructure in vivo using MRI has proven to be difficult due to the limited T_1 and T_2 contrast between different regions and the relatively low achievable spatial resolution at 1.5T and 3T [5]. The availability of ultra high field (7T) scanners and a wider range of contrasts now opens up new possibilities for using MRI to probe thalamic anatomy.

The aims of this chapter are (1) to assess the capability of post-mortem 7T MRI to visualise and identify thalamic nuclei with comparison to histological data from the same brains. (2) To optimise the in vivo contrast within the thalamus. (3) To enable the delineation of the thalamic nuclei in vivo with reasonable confidence.

In this chapter, the contrast within the thalamus and the ability to delineate and identify

the nuclei, manually and automatically, was investigated. A review of the segmentation techniques used in the literature to delineate thalamic nuclei, is presented. A range of high resolution MR sequences for imaging of post-mortem and in vivo brains were optimised and a range of segmentation techniques were assessed. A process for manually delineating and identifying thalamic nuclei was defined. Results from post-mortem imaging, segmentation and comparison with histology are presented. The broad and fine structures of the nuclei were delineated, the nuclei were identified and compared between manual outlines and automatic segmentation (primarily hierarchical clustering). The delineation of the nuclei in in vivo images was rated across subjects and imaging contrasts.

Figure 5.1 shows a few atlas slices used often in this project. Below are the abbreviations used to denote the structures observed (taken from Morel atlas):

AC- anterior commissure
AM- anteromedial nucleus
AV- anteroventral nucleus
Cd- caudate nucleus
CeM- central medial nucleus
CL- central lateral nucleus
CM- centre median nucleus
Fx- fornix
IC- internal capsule
LD- lateral dorsal nucleus
Li- limitans nucleus
LP- lateral posterior nucleus
MB- mammillary body
MD- mediodorsal nucleus
MDmc- mediodorsal nucleus, magnocellular division
MDpc- mediodorsal nucleus, parvocellular division
MDpl- mediodorsal nucleus, paralamellar division
MTT- mammillothalamic tract
MV- medioventral nucleus
Pf- parafascicular nucleus
Po- posterior nucleus
PuA- anterior pulvinar
PuL- lateral pulvinar
PuM- medial pulvinar
Pv- paraventricular nuclei
R- reticular thalamic nucleus
RN- red nucleus
sPf- subparafascicular nucleus
STh- subthalamic nucleus
VA- ventral anterior nucleus
VAmc- ventral anterior nucleus, magnocellular division
VLa- ventral lateral anterior nucleus
VLp- ventral lateral posterior nucleus
VM- ventral medial nucleus

VPL- ventral posterior lateral nucleus
VPLa- ventral posterior lateral nucleus, anterior division
VPLp- ventral posterior lateral nucleus, posterior division
VPM- ventral posterior medial nucleus
VPMpc- ventral posterior medial nucleus, parvocellular division
ZI- zona incerta

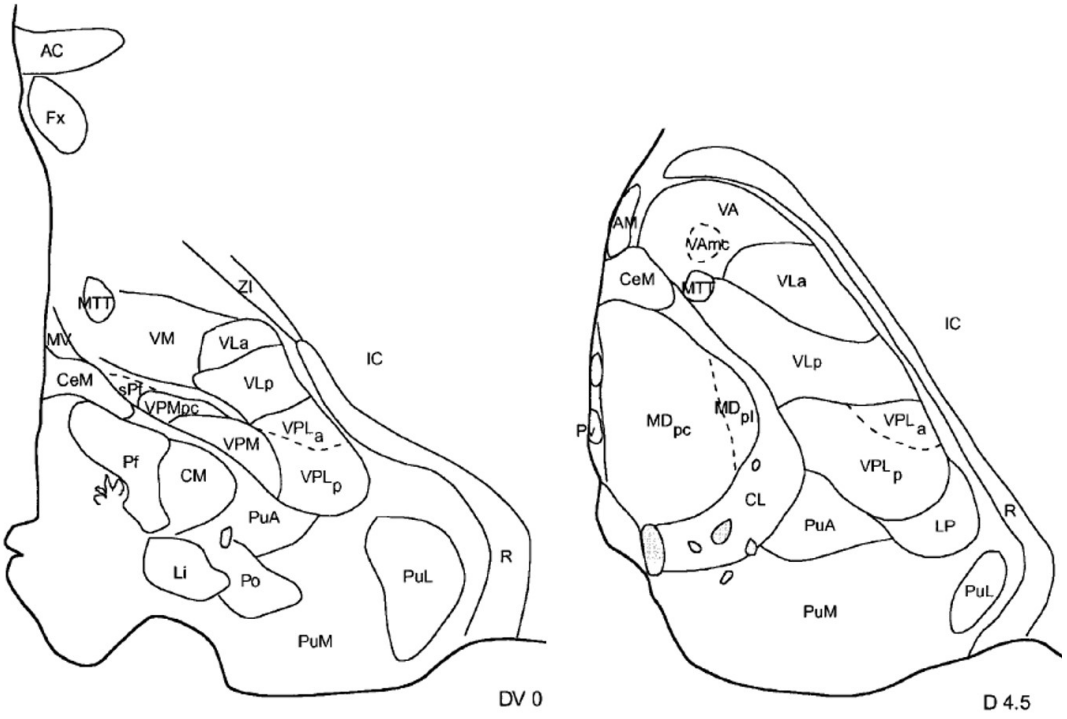

Figure 5.1: Commonly used slices from the Morel atlas [3], to illustrate the location of the nuclei listed above.

5.1.1 Review of MRI Thalamic Segmentation Methods

The thalamic nuclei have been delineated in MR images in previous studies, using a variety of imaging and analysis techniques.

Imaging Methods

Based on the anatomical features in MR images, the boundaries of the thalamic nuclei have been identified with varying degrees of complexity. In a study by Deistung et al., 7T GRE 0.4mm isotropic scans were used to calculate and compare magnitude, QSM, frequency and R_2* images on which to outline nuclei [6]. QSM provided greater contrast and could visualise structures that were not visible in the other contrasts, as shown in Figure 5.2. The outlines used by Deistung et al. are mostly based on the older Olszewski [7] and Schaltenbrand [8] atlases, but the Morel [3] atlas was also used.

An alternative contrast can be produced by nulling the white-matter signal in an MPRAGE sequence, at 7T [1]. After scanning and measuring T_1 values in 5 subjects, optimum

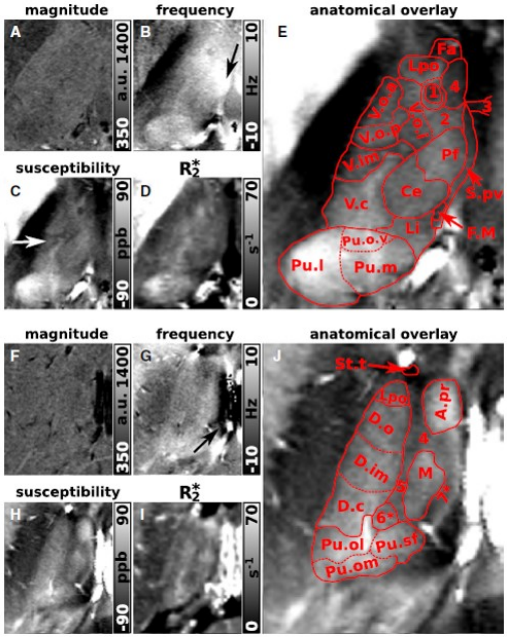

Figure 5.2: 7T QSM based contrast by Deistung et al. [6].

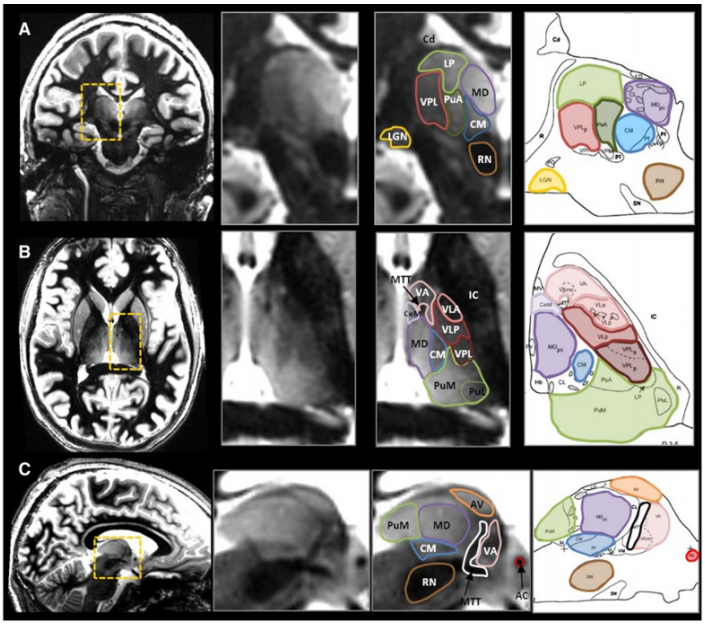

Figure 5.3: Contrast in white matter-nulled MPRAGE by Tourdias et al. [1].

parameters were simulated for an MPRAGE sequence which was then performed on a further 6 subjects. This produced good thalamic contrast, as shown in Figure 5.3, as long as the inversion time was close to the white matter null point for each subject individually. Such anatomical approaches are least common due to poor overall thalamic contrast, especially at lower field strengths.

As the thalamus is an important pathway of information flow through the brain, many nerve fibres project to and from it. As such, the white matter fibres have been traced

from the cortex, back to nuclei within the thalamus. One technique to measure the orientation of the fibres within the thalamus is diffusion tensor imaging (DTI). An example of a DTI image of a stroke patient [9] is shown in Figure 5.4. The colours represent the fibre orientation which is enough to show the broad structure of the thalamus, however due to the low contrast and resolution, DTI lacks the required detail to identify the fine structure.

As the visibility of the thalamic structures are poor in DTI, another study used spectral clustering to systemically produce groupings of voxels, to identify the location of a range of nuclei [10], as shown in Figure 5.4. However, the groupings lack the fine detail of the thalamic structure as described in various thalamic histology atlases.

To enhance the detail within the thalamus, the fibres from the cortex have been tracked back to the thalamus using diffusion tractography (DTT). This takes DTI a step further and can be done with a probability based segmentation [11], as shown in Figure 5.4. The measured groupings were linked to the Brodmann areas, and lesions, from patients with bilateral thalamic infarcts. The groupings were identified to cover a range of nuclei, but the boundaries of the groupings were not correlated to the boundaries of the thalamic nuclei from any histological atlases.

Figure 5.4 shows a higher resolution $1mm^3$ stochastic fibre tracking method provided a better segmentation [12]. The contrast was derived from the functional areas of the cortex rather than the physiological differences between the nuclei, therefore the structures do not directly relate to the anatomy of the thalamus.

All of these techniques suffer from the same limitations of low spatial resolution and poor correlation with the histological definitions of the nuclei. Also the regions are not easily matched with nuclei from atlases, except in the spectral clustering study [10].

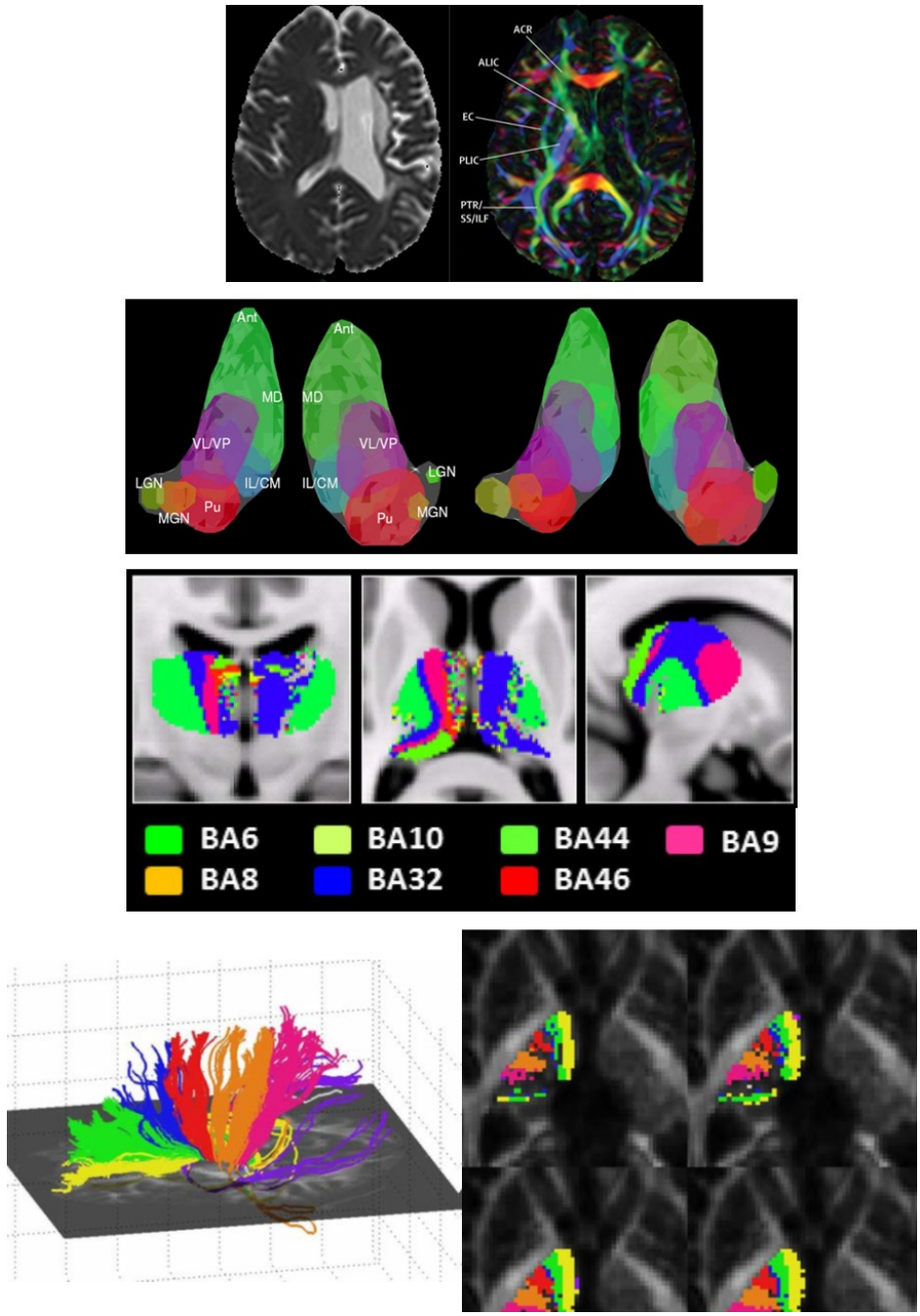

Figure 5.4: DTI based thalamic nuclei segmentation. (Top row) example of DTI image quality for stoke patient [9]. (Second row) spectral clustering [10]. (Third row) DTT probability based segmentation, linked to Brodmann areas [11]. (Bottom row) Higher resolution 1mm^3 stochastic fibre tracking [12].

Segmentation Methods

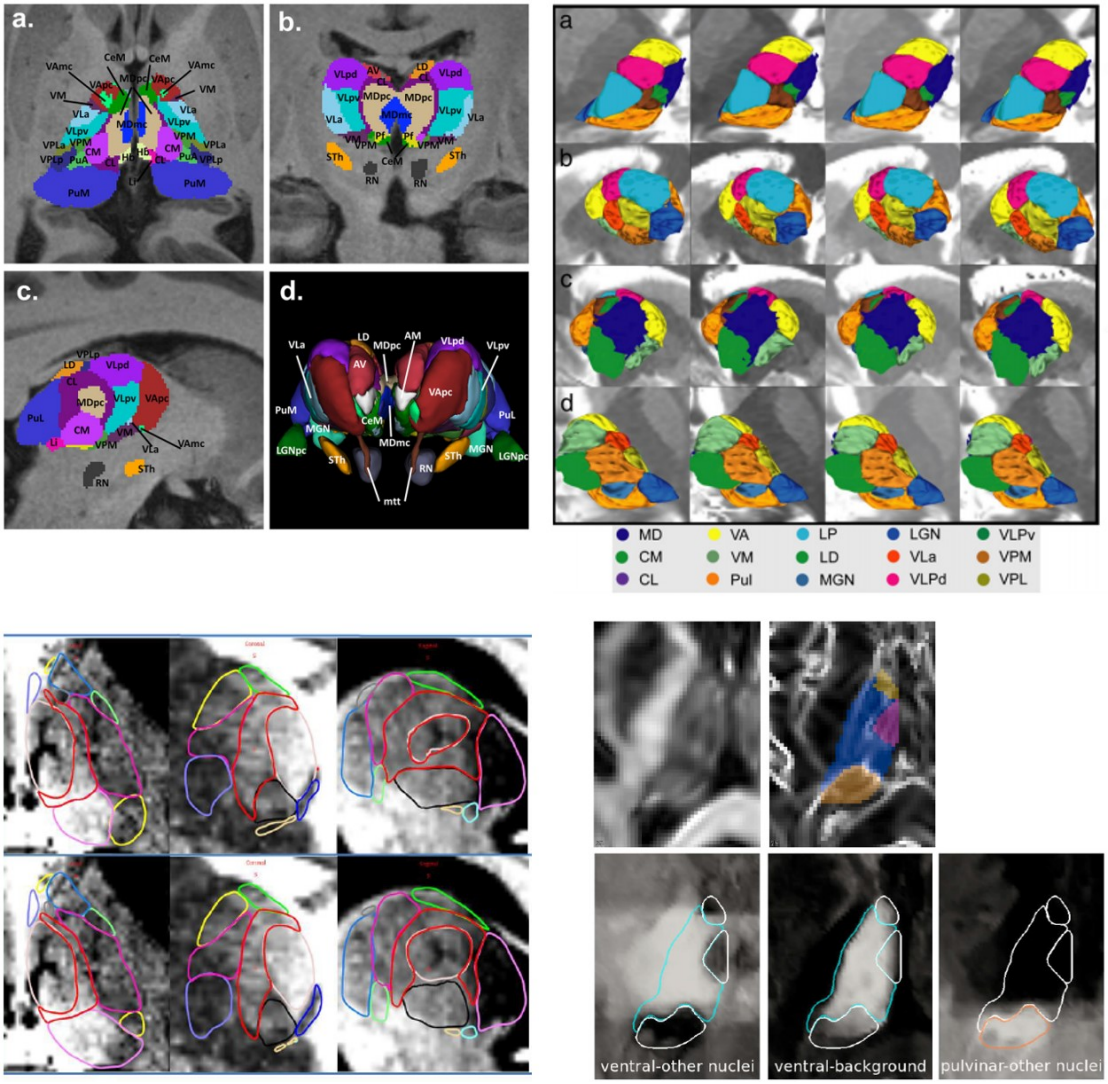

Figure 5.5: Algorithm based thalamic nuclei segmentation. Top left: Multi-contrast head model [13]. Top right: k-means clustering [14]. Bottom left: shape models [15]. Bottom right: random forest clustering [16].

Automated segmentation techniques have been used to delineate the thalamic nuclei as the MR contrast is too low for manual annotations, and also this approach has been used to avoid significant bias of the annotator [17]. Numerous methods have been used to classify image voxels into groups belonging to different nuclei, as described below.

The most comprehensive approach involved producing a model using 3T T_1, T_2, MRA and DTI scans [13], as shown in Figure 5.5. The multiple contrasts were initially processed and then segmented using k-means clustering on the first and last slices and were then refined manually. A topologically flexible interpolation was used to automatically segment the tissue in the middle slices and the refinement was repeated, to identify 153 structures. This method requires many scans and a great deal of analysis. Similarly, k-means has also been used on 1.5T T_1 and T_2 weighted images [14]. Reasonable contrast

is shown in (8 subject) averaged T_1 maps. This approach worked for lower resolution and lower contrast data.

An alternative method of segmenting the nuclei is using shape models, produced from 7T MPRAGE images which were manually delineated. The shape models were then applied to 3T images which worked by splitting the image into large regions of nuclei which were subsequently split into smaller and smaller subregions, forming a hierarchical structure, to obtain outlines of the thalamic nuclei [15], as shown in Figure 5.5. This appeared to work well.

Segmentation can also be performed with initial user guidance. Random forest learners were given a training set to generate a multi-dimensional feature set which was associated with manually delineated nuclei [16]. It is difficult to generate the training set if the contrast is too low. On the other hand, the random forest segmentation would not be required if the contrast was high and the nuclei were clearly visible.

In summary, the anatomical contrast within the thalamus in MRIs is limited. Tractography gives a measure of functional rather than physical structure. Automated segmentation is more systematic, however it is difficult to verify visually and requires a great deal of analysis, limiting its use in a clinical setting since the physiological differences between the nuclei are subtle. The QSM appeared to be more sensitive than the magnitude images, but a combined image optimisation and segmentation approach would provide the best of both methods.

5.2 Method

A series of scans were optimised and performed on post-mortem and in vivo brains. Histology of a post-mortem brain was acquired, which the post-mortem MRI was compared to, to assess the contrast within the thalamus and the ability to visually identify the nuclei. The nuclei were manually delineated in the histological, post-mortem and in vivo data and compared with systematic delineations using automatic segmentation methods.

5.2.1 Image Acquisition

Post-mortem MRI

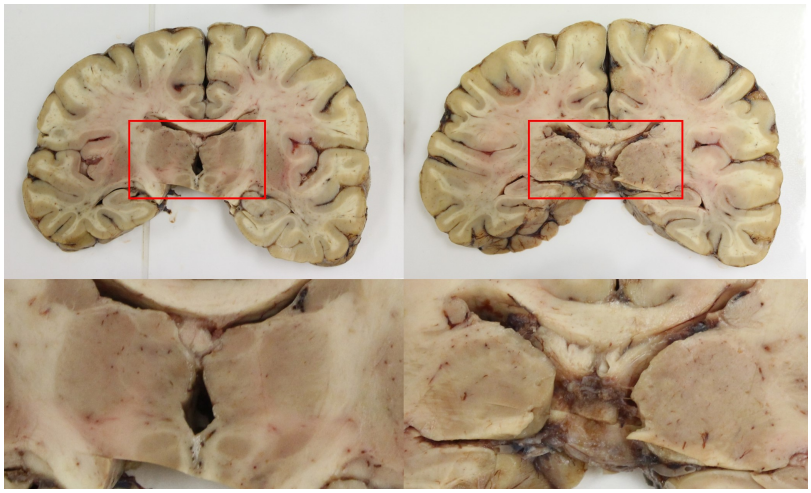

Figure 5.6: Raw fixed post-mortem tissue of coronal anterior section (left) and posterior section (right) of the thalamus. Red rectangle indicates area of zoomed images.

The ability of 7T MRI to provide contrast between the thalamic nuclei was investigated using six post-mortem brains (Brains 3-8 as detailed in Table 5.1) which were obtained with consent for research. After 1-5 months of fixation in formalin, the frontal cortex was removed and one cerebral hemisphere from each brain was placed inside a Fomblin-filled (Solvay Solexis, Brussels, Belgium), 16cm-diameter plastic sphere, and wedged in position with sponge blocks. Each brain was scanned over an 11 hour period on a 7T Philips MRI scanner, with FFE gradient echo, multi gradient echo, inversion recovery and pulsed saturation sequences, which were used to calculate R_2*, R_1, QSM and magnetisation transfer ratio (MTR) maps, respectively. The scan parameters are detailed in Table 5.2.

	Brain 3	Brain 4	Brain 5	Brain 6	Brain 7	Brain 8
ID	16D37005	16D28190	16D14540	16D26011	16D35916	16D31741
Period between death and post-mortem (PM)	9 days	8 days	2 days	7 days	10 days	7 days
Date of PM	17/08/16	27/06/16	05/04/16	13/06/16	10/08/16	26/07/16
Age at death	82	62	79	69	92	74
Sex	F	M	M	M	F	M
Diagnosis	dementia -pulmonary embolism	Healthy brain, Aortic valve disease	Pulmonary fibrosis	Dementia with Lewy bodies	Cancer of unknown primary	Metastatic carcinoma, no known dementia
Section scanned	right	left	left	left	right	left
Fixation Period						
1	scan1-09/09/2016				scan1-28/09/2016	
2						scan1-29/09/2016
3		scan1-24/09/2016		scan1-27/09/2016		
4						
5			scan1-26/09/2016			

Table 5.1: Properties of post-mortem brains used in thalamus study.

Histology

After MR imaging, the thalamus from the opposite side of Brain 6 was sectioned into 7 coronal slices of thickness 5μm, separated by 1.8mm. These were stained using luxol fast blue (LFB) to highlight myelin within the thalamic substructure, and immunohistochemically stained for synaptophysin, a marker protein of neuroendocrine cells which is present in the synapses [18].

Subsequently, coronal MRI data was registered to the histology using an affine two dimensional registration in Matlab (Mathworks, Massachusetts, United States). The intensity values in the stains were correlated with the T_1, R_1, R_2*, MTR and susceptibility values, to probe the underlying MRI contrast mechanisms within the thalamus.

In vivo MRI

For in vivo scanning, the post-mortem sequences were adjusted by increasing the slice thickness to 1.2mm, reducing the NSA to 1 and turning on SENSE 2, to produce acquisition times of less than 10 minutes duration. Initially, 5 healthy volunteers were scanned with a 3D multi-slice GE sequence (0.3x0.3x1.2mm^3 voxel, FOV=200x178x86mm^3, TE1=16ms, flip angle=20^o), under ethical approval from the University of Nottingham Medical School Ethics Committee. The contrast between the thalamic nuclei and signal to noise ratios of the in vivo and post-mortem magnitude images were compared across the thalamus and other deep grey matter regions.

	Single echo GE	Multi-echo GE	Inversion Recovery	Magnetisation Transfer
Resolution (mm^3)	0.33x0.33x0.33	0.6x0.6x0.6	0.6x0.6x0.6	0.6x0.6x0.6
FOV (mm^3)	192x170x80	192x161x80	200x181x80	192x160x80
Flip Angle (^{o})	17	25	8	8
NSA	4	4	4	4
Approx. scan time (hr)	5	2	4	1
TE1 (ms)	20	9.1		
Echoes	1	5		
ΔTE (ms)		9.1		
TI (ms)			250-2100	
Saturation pulses / angle (^{o})				20/500
Duration (ms) / pulse spacing (ms)				30/60

Table 5.2: Scan parameters for post-mortem MR imaging.

A series of sequences was optimised for in vivo contrast between the thalamic nuclei, using an additional set of healthy volunteers. These sequences included multislice FLASH (fast low angle shot- T_1-FFE), FSE (fast spin echo- SE-TSE), DTI (diffusion tensor imaging- SE-EPI) and IR-TSE (inversion recovery- turbo spin echo) sequences, as detailed in Table 5.3. To reduce brain movement, the sequences were cardiac-gated where possible. As the heart pumps blood to the head, this causes small movements of the brain on the order of 0.1-0.5mm [19]. This is enough to cause blurring in some sequences especially at high resolutions.

	FLASH	FSE	DTI	IR-TSE
Resolution (mm3)	0.3x0.3x1.2	0.4x0.4x1	1.5x1.5x1.5	0.35x0.37x1
FOV (mm3)	164x164x26	164x164x24	164x164x24	164x164x24
Cardiac-gated	yes	yes	yes	no
TR beats	1	6	3	
TR (ms)				15859
Dynamics	2	1	5	1
Scan time (min)	9	7	6	8
TE (ms)	25			6.3
Echoes	1			
Slice gap (mm)		0.2		0.2
Refocusing angle (^{o})		90		160
Halfscan			0.689	
TI (ms)				320

Table 5.3: MR parameters for optimised in vivo thalamus sequences.

A scanning protocol was then formed from the FLASH and FSE (as well as a PSIR for positioning the imaging stack on the thalamus) and a further 5 healthy volunteers (age=26.6$\pm$5.4 years, 2 male and 3 female) were scanned. The contrast was compared

across the magnitude images produced using the different sequences. The VSHARP filtered phase and QSM were also calculated from the 3D T_2* and FLASH data, as additional contrasts. These were then compared with the post-mortem images to assess image quality.

5.2.2 Manual Delineation

Initially, the thalamic nuclei were identified on the histological sections by referencing to the Morel atlas [3]. The stains were compared to the coronal post-mortem MRI data from the scanned hemisphere by visually identifying common boundaries. Thalamic features were then compared across the different axial post-mortem MR contrasts and all of the brains. Groups of nuclei were matched to the atlas and then were outlined by identifying consistent features between brains and image types.

Manual delineations of the thalamic nuclei were methodically obtained by using all the different image contrasts. The major groups of nuclei were identified first to provide a rough overall structure. Firstly, the largest nucleus was outlined on the image with the greatest contrast, usually the QSM. Secondly, the outline was verified by alternating between the QSM, FLASH magnitude and FSE images, in the case of the in vivo data, and adjusting the boundary of the nuclei if necessary. Then the next largest nucleus was identified and the above process was repeated until the smallest nuclei and the nuclei with the lowest contrast within the slice were outlined, as illustrated in Figure 5.7.

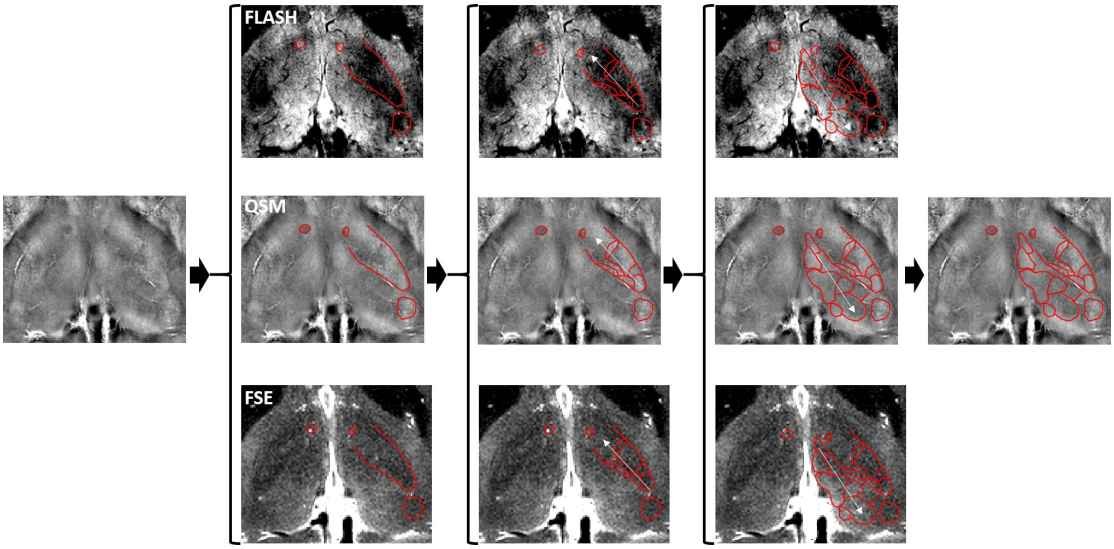

Figure 5.7: Flow diagram of the process of manually outlining the thalamic nuclei on in vivo FLASH (top), QSM (middle) and FSE (bottom) MR images. White arrows indicate the order in which the groups of nuclei were broken down.

The above process was performed on the histology, post-mortem MRI and in vivo data, using the different image contrasts in each of the datasets, to obtain manual delineations of the thalamic nuclei.

5.2.3 Automatic Segmentation

Comparison of Techniques

To improve confidence in the delineation of nuclei and to overcome annotator bias, automatic segmentation techniques were also used to outline the nuclei based solely on image contrast. The following methods were tested for capability to systematically identify the thalamic nuclei.

Canny edge detection was initially trialled, as it is better at dealing with noise compared to other edge detection methods [20]. It was applied to the different contrasts after the image intensity histograms had been distributed evenly to broaden the image contrast range (histogram equalisation), to systematically delineate boundaries within the image. Landmarks were then identified on these boundaries to non-linearly register the MRI with landmarks on slices from the Morel [3] atlas using thin-plate spline warping.

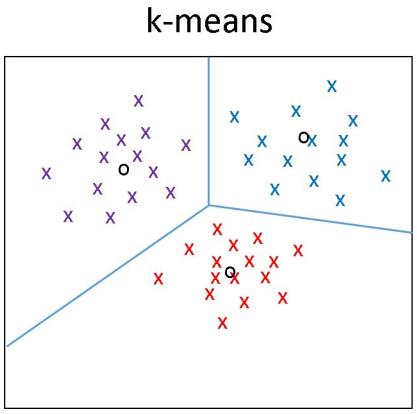

Figure 5.8: k-means cluster with k=3. Black circles indicate the means of the clusters.

For automatic segmentation, k-means [21] and hierarchical clustering [22] were used to systematically segment the smaller nuclei. In k-means clustering, the clusters are generated by minimising the within cluster sum of squares of a set of points for a given number (k) of centres (means), as illustrated in Figure 5.8. Standard methods are iterative. The centres are randomly placed and the points are divided into clusters by finding the nearest mean. The new mean is placed at the centroid of each cluster, as shown with black circles in Figure 5.8, and this process is iterated until the results converge.

Hierarchical clustering generates groupings by calculating the distance between a set of coordinates and ordering them by closest distance to form subgroups [22]. These are ordered in turn until the distance between all subgroups and groups are found to build a hierarchy of distances. This is then cut through using a threshold value or by defining a number of groups, as illustrated in Figure 5.9, to form the clusters.

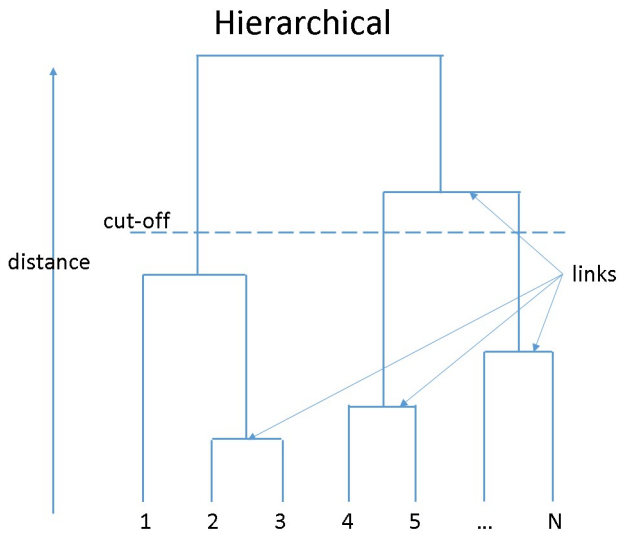

Figure 5.9: Hierarchy of voxel distances, showing links between voxels and groups of voxels.

Application of Segmentation

In practice, the dimensions were placed as column vectors into a matrix with dimensions, number of voxels x N (contrasts). The Euclidean distances between the intensity values of the voxels in 1, 2, 3 or more dimensions was calculated, which was used to generate the linkages in the hierarchy and the number of groupings was set manually.

Hierarchical clustering was applied to the spatial coordinates of the voxels and the voxel intensity values in the GE, R_2*, R_1 and MTR images, to find the Euclidean distance in N dimensional space, for the post-mortem data. The dimensions used for the hierarchical clustering of the histological data were, spatial coordinates, synaptophysin and LFB. The histology and post-mortem MRI data from the scanned hemisphere were compared, through the use of k-means clustering, Canny edge detection and hierarchical clustering.

Hierarchical clustering was applied to the in vivo images in the same way as for the post-mortem data, to delineate the thalamic nuclei without human bias from an expectation of outlines derived from the atlas. The clustering parameters were empirically adjusted to compensate for the reduced contrast in the in vivo images. The clustering was firstly applied to the individual magnitude, QSM and FSE contrasts, secondly to a combination of the magnitude and QSM and thirdly to a combination of all 3 contrasts. Subsequently, the clustering was applied to 2D slices with manually scaled intensity levels to match the images used for the annotations. Finally, the clustering was applied across a set of 3 adjacent slices, to form 3D clusters.

Comparison of Manual Delineation and Automatic Segmentation

To assess the performance of the automatic segmentation techniques, these were compared with the manual outlines. The position of the boundaries relative to each of

the identified bordering nuclei in the histology (and coronal post-mortem MR images), were manually matched with the boundaries in the hierarchical clustering, k-means clustering and Canny edge detection of the histology.

For the post-mortem MRI data, the automated clusters were compared to the manual outlines of the same slice to assess the differences between the perceived boundaries and image-derived boundaries. The manual outlines were overlaid on the groupings from the hierarchical clustering.

In order to compare the boundaries of the nuclei in the in vivo manual outlines and clusters, and variability across subjects and imaging contrasts, the clusters were rated across the 5 subjects for how many clusters each nuclei was visible in, per contrast. The nuclei were given 1 point per subject, for a maximum of 5 points, if either the majority of the boundaries and area of the manual outlines and clusters overlapped or if the clusters would help to redefine the location of the manual outlines, i.e. if the cluster was convincing or useful. This was done as some nuclei were consistently identifiable in the clusters, but displaced from the manual outlines.

5.3 Results

The results are presented in the following order to provide convincing outlines of the thalamic nuclei, from the highest quality dataset (histology), relating it to the imaging technique (post-mortem MRI) and assessing the degree of contrast reduction in the most applicable imaging technique (in vivo MRI). The broad and fine structures of the nuclei were identified and compared between manual outlines and automatic segmentation techniques, primarily hierarchical clustering.

5.3.1 Histology

Imaging

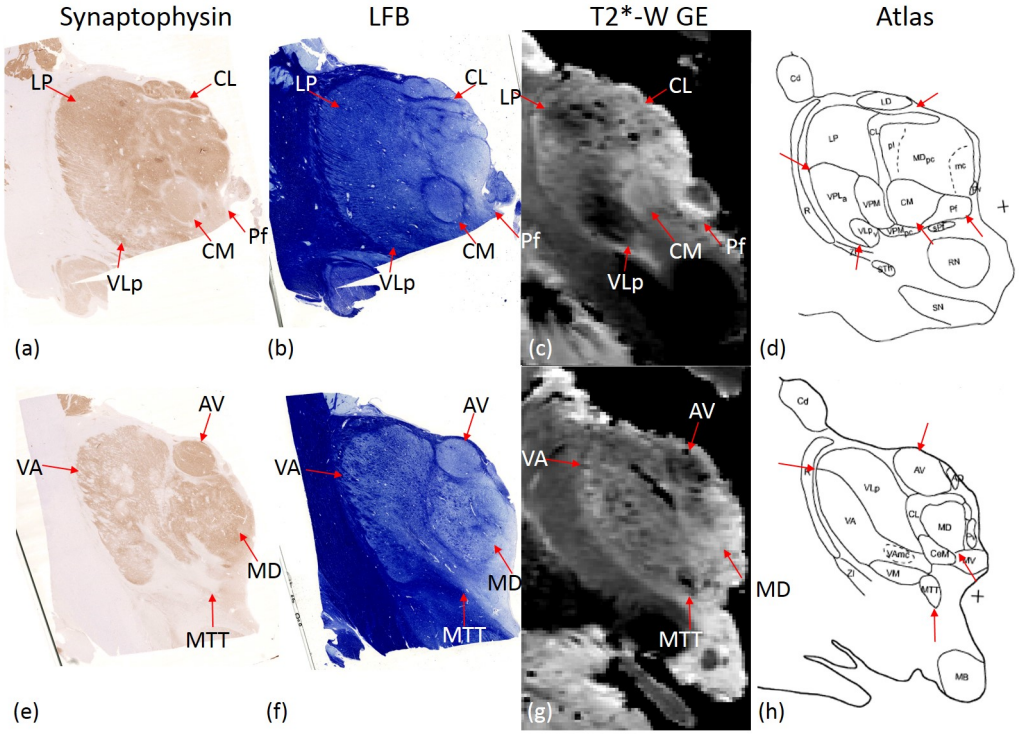

Figure 5.10: Comparison of coronal stained sections and MRI allowing matching to the atlas and thus identification of nuclei within the thalamus on post-mortem scans. a) Coronal Synaptophysin and b) LFB stains of sectioned right thalamus with c) corresponding high resolution GE magnitude MR image of left thalamus and d) atlas slice. e-h) Equivalent images for anterior section of thalamus.

Histology is the gold standard for the visualisation of thalamic nuclei as it has greater resolution and specificity in the thalamus, than MRI. Figure 5.10 shows that the synaptophysin and LFB stained sections containing distinct boundaries, which appeared as light brown and dark blue, respectively. These correlated with the coronal T_2* weighted MRI scans, as a range of boundaries were identified manually across the images, including the LP, CL, Pf, CM and VLp.

Automatic Segmentation

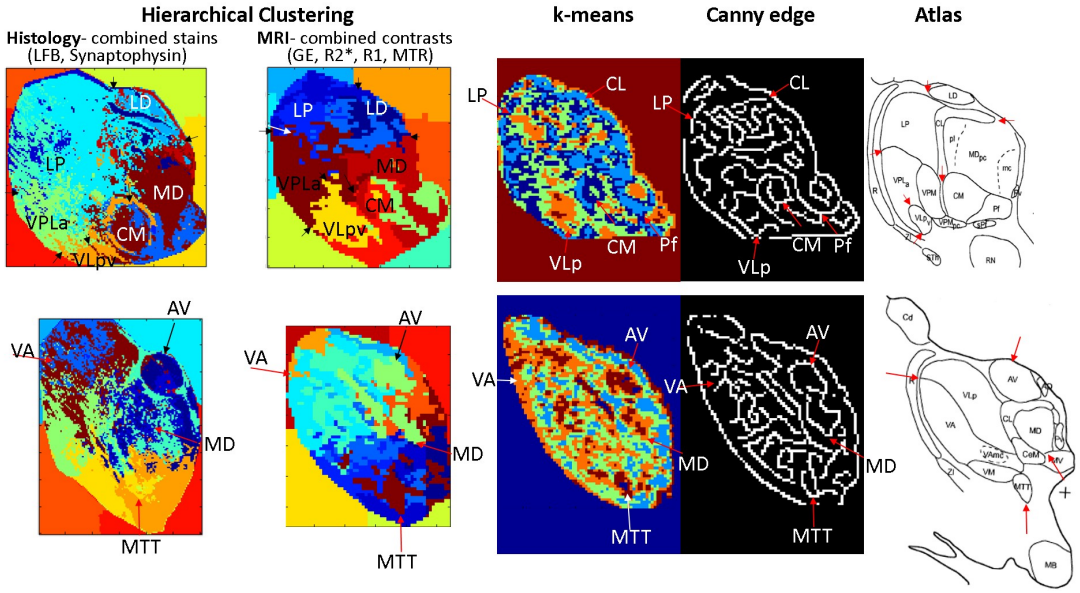

Figure 5.11: A comparison of hierarchical clusters generated from MRI and stains. Hierarchical clustering of combined a) stains and b) MRI contrasts. c) k-means clustering d) Canny edge detection and e) atlas slice. f-j) Equivalent images for anterior section of thalamus.

In Figure 5.11, the k-means clustering, Canny edge detection and hierarchical clustering of the combined contrasts of the post-mortem MRI (GE, R_2*, R_1 and MTR) and histology (LFB and synaptophysin) contain similar structure for the stains and MR images. The k-means and Canny results are noisy and include additional edges caused by the noise in the underlying MRI data. The nuclei identified as the VLp, VPM, CM, CL, LD and VPLa are marked with arrows.

5.3.2 Post-mortem MRI

Imaging

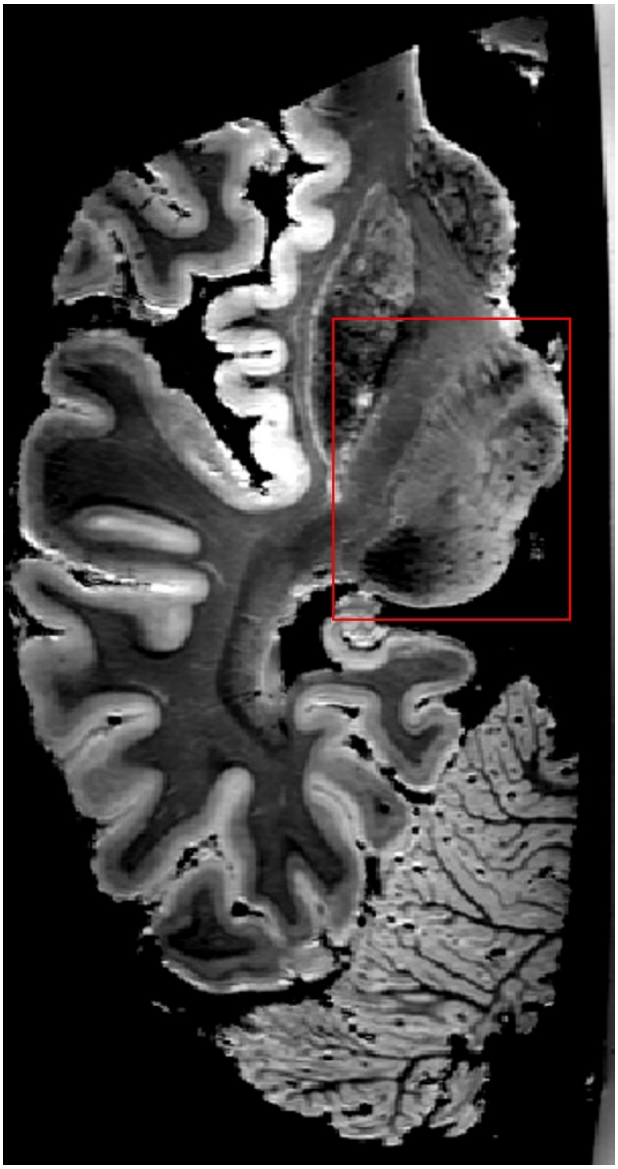

Figure 5.12: Axial, 0.3mm resolution T_2*-weighted magnitude image of left cerebral hemisphere acquired post mortem from Brain 6. Red box indicates zoomed section of the thalamus, as shown in Figure 5.13.

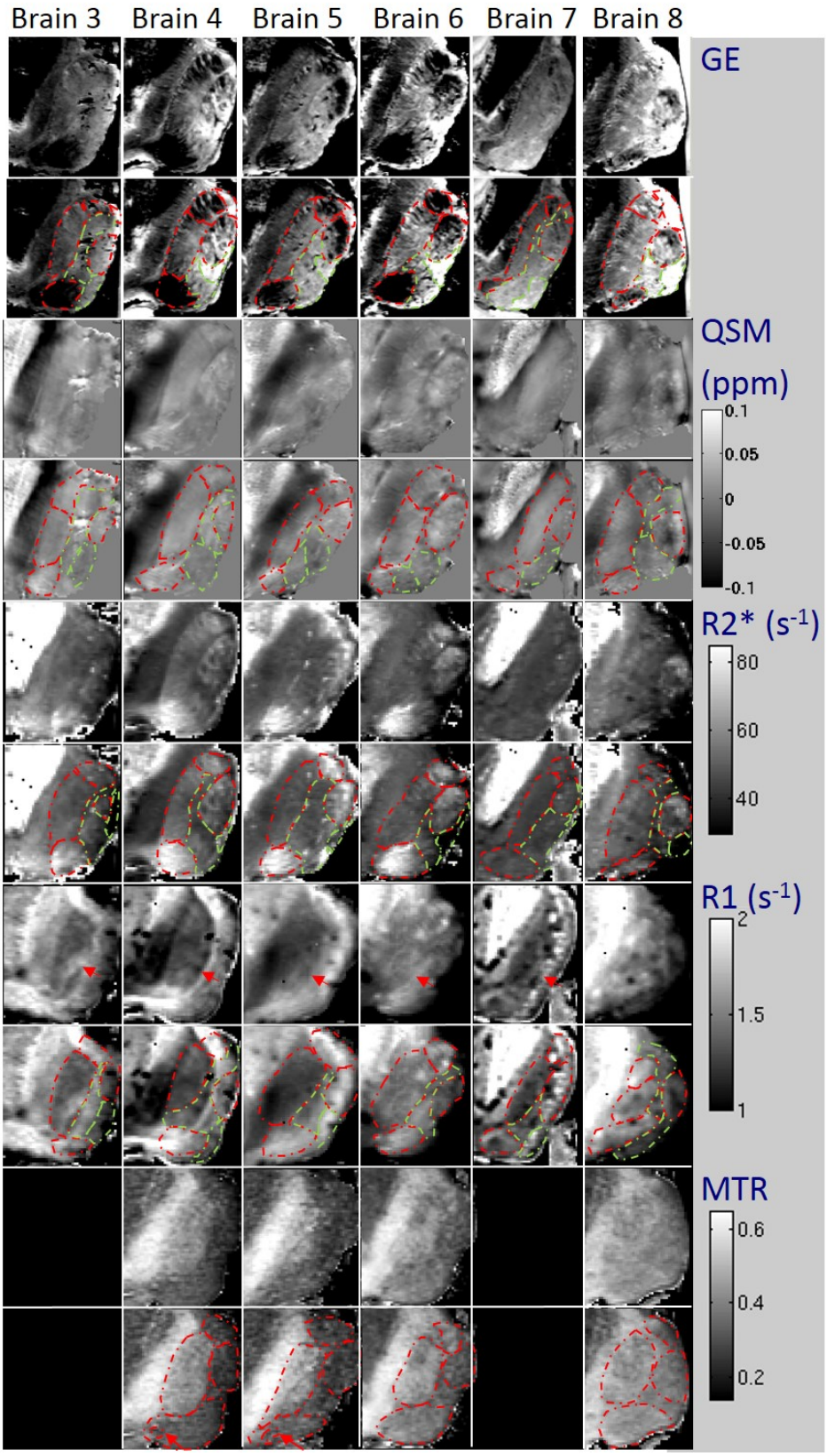

Figure 5.13: From top to bottom: 0.3 mm resolution T_2*-weighted magnitude and QSM images and 0.6 mm resolution R_2*, R_1 and MTR maps from six different post mortem brains (Brains 3-8). Each image is shown twice, with the identifiable thalamic sub-regions, identified using all contrasts, were delineated on the lower image of the pair. Consistently identified sub-regions are shown in red, while less consistently seen sub-regions are shown in green. MTR data was not acquired from Brains 3 and 7.

Figure 5.13 shows axial MR images of the six post-mortem thalami, with different contrasts. Consistent groups of nuclei were outlined across the brains to identify broad structures, without using references such as histology or an atlas. Five consistently observed sub-regions of the thalamus and two less consistently observed sub-regions are outlined in red and green respectively, on the high-resolution T_2*-weighted GE images. Only four regions were consistently identified in the QSM, R_2* and R_1 maps, and these displayed opposite intensities compared to the T_2*-weighted images. The MTR maps showed four regions, with a smaller hypointense region visible inside a larger region in some thalami (red arrows).

The R_1 maps showed a bright band through the middle of the post-mortem thalamus (shown with red arrows), caused by the cross-linking in the fixation front as it diffuses through the tissue. This obscured some of the boundaries, which were then estimated. The contrast of the MTR does appear to be similar to the R_1 map, as R_1 is expected to decrease as MTR increases, as both are influenced by myelin. However, the MTR does not appear to be as heavily affected by the fixation front as the R_1 map. The T_2*-weighted GE images, QSM and R_2* maps show almost no sign of being affected by the fixation front.

Correlation of Contrast in Histology and Post-mortem MRI

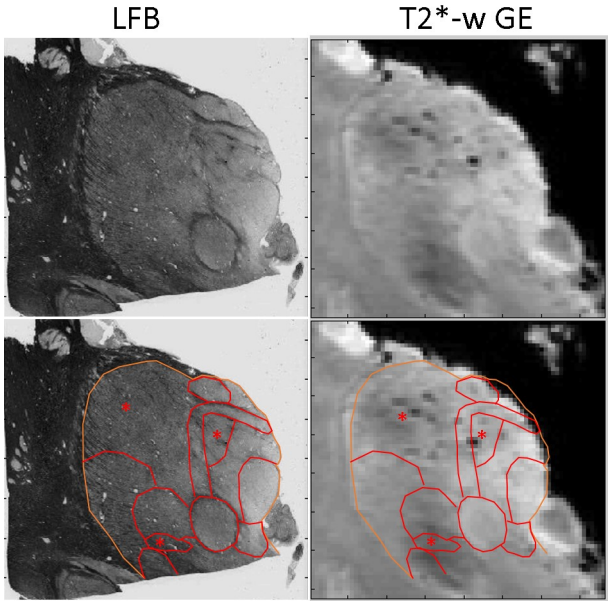

Figure 5.14: LFB stains and high resolution GE MRI with overlay of manually outlined boundaries from LFB on the MRI.

Figure 5.14 shows the LFB stain and T_2*-weighted high resolution GE MRI. The boundaries in the LFB image were outlined, overlain on the GE and compared to the intensities of the boundaries in the GE. The nuclei generally are homogeneous in intensity and are surrounded by dark boundaries, in both the LFB and GE. The MRI contained

many hypointense regions, indicated with stars in both the stain and MRI.

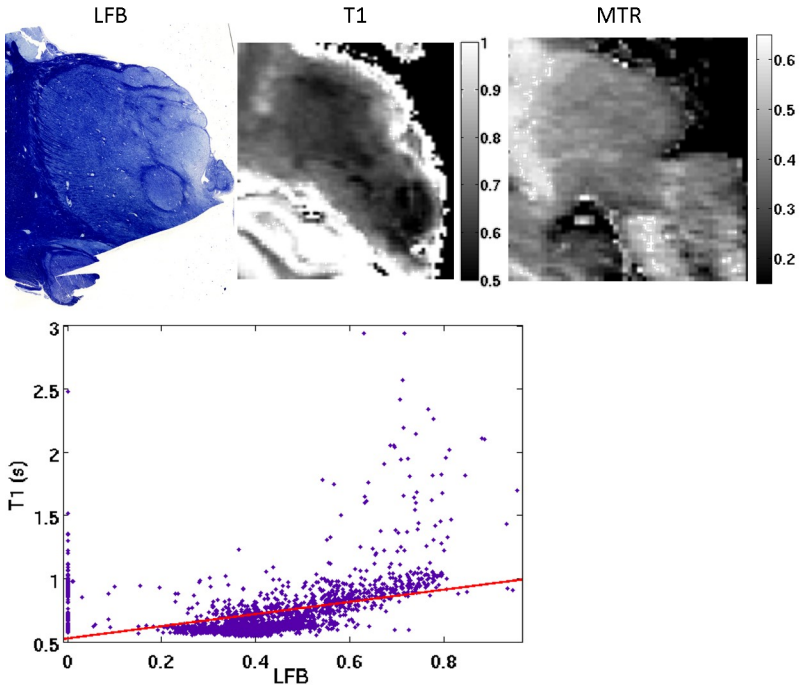

Figure 5.15: LFB stain, T1 and MTR maps. Plot of T_1 values against LFB intensities, in the thalamus. Comparison of contrast in LFB stains and high resolution GE MRI.

A plot of T_1 values against LFB intensity values is shown in Figure 5.15, along with the corresponding slices. T_1 increases linearly with a gradient of 0.4818±0.02s with normalised greyscale LFB intensities, although some points deviate from the linear fit at high LFB image intensities (low staining).

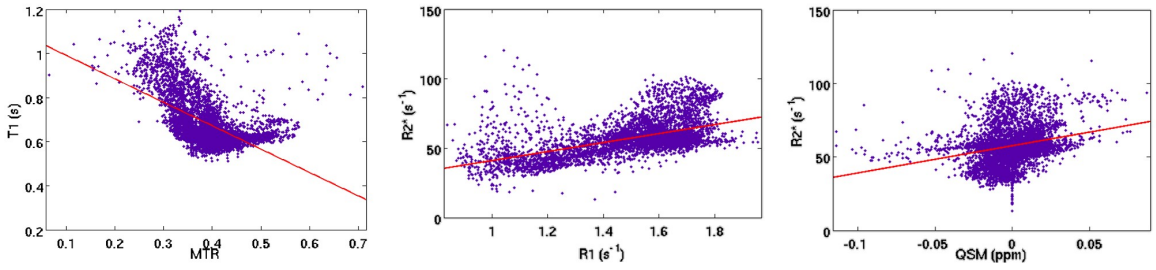

Figure 5.16: Plots of T_1 against MTR, R_2* against R_1 and R_2* against susceptibility values.

Figure 5.16 shows a plot of T_1 values against MTR, for voxels within the thalamus, in Brain 6. There is a negative correlation of -1.062±0.04s. Most of the points are close to the linear fit but there is a large spread of points for voxels with small MTR and large T_1 values. There is a large amount of noise in the fitting of T_1, especially from background voxels with low signal intensities. R_1 increases with fixation, as shown in Chapter 4,

therefore T_1 would decrease in highly myelinated areas which have large MTR values, but MTR is visibly much less affected by fixation, as shown in Figure 5.13.

Figure 5.16 also shows plots of R_2* against R_1 and R_2* against susceptibility values. R_2* increases linearly with R_1 with a coefficient of 32 ± 1 and the points are spread evenly. R_2* increases linearly with susceptibility with a gradient of 190 ± 20 s^{-1} ppm^{-1}, but the points are more centred around 0ppm.

Manual Delineation

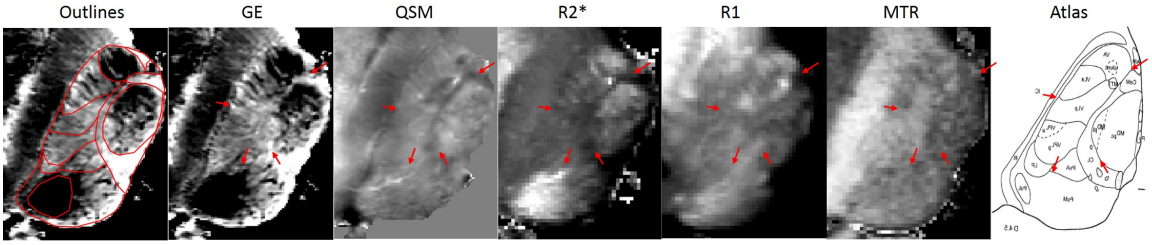

Figure 5.17: (Left to right) High resolution GE magnitude image for brain 6 with and without manually drawn outlines. QSM, R_2*, R_1 and MTR maps and corresponding slice from atlas. Red arrows indicate boundaries between VLa and VLp, top of PuM, top of CM and bottom of MD.

The consistently-identified groups of nuclei from Figure 5.13 were split into subregions, as the majority of the thalamic nuclei were identified and outlined. Figure 5.17 shows the manually drawn outlines of the nuclei, overlaid on the magnitude image. The contrast in the GE image was adequate to identify most of the nuclei so the less clear nuclei were identified with the help of the additional contrasts and with reference to the atlas. The R_2* maps and QSM data had similar contrast to the T_2*-w image but the R_1 had a bright band across the thalamus and the MTR was more blurry.

Automatic Segmentation

Figure 5.18 shows the results of applying Canny edge detection to the different image types from Brain 6. This generated multiple subdivisions across the VA, VLa, VLp and VPL, leaving a similar problem to that faced with the raw images. Also shown are the segmented images produced by applying k-means clustering (7 clusters) to histogram-equalized images from Brain 6.

To identify the smaller nuclei, the MRI data was thin-plate spline warped to the atlas using landmarks identified from the Canny edge detection on the MRI data, as shown in Figure 5.19. This gave a good estimate of the location of the smaller nuclei, but the boundaries in the MR image became blurred.

Figure 5.20 shows the effect of including spatial coordinates, and additional contrast on the hierarchical clustering of the high resolution GE data. Clustering on the intensities

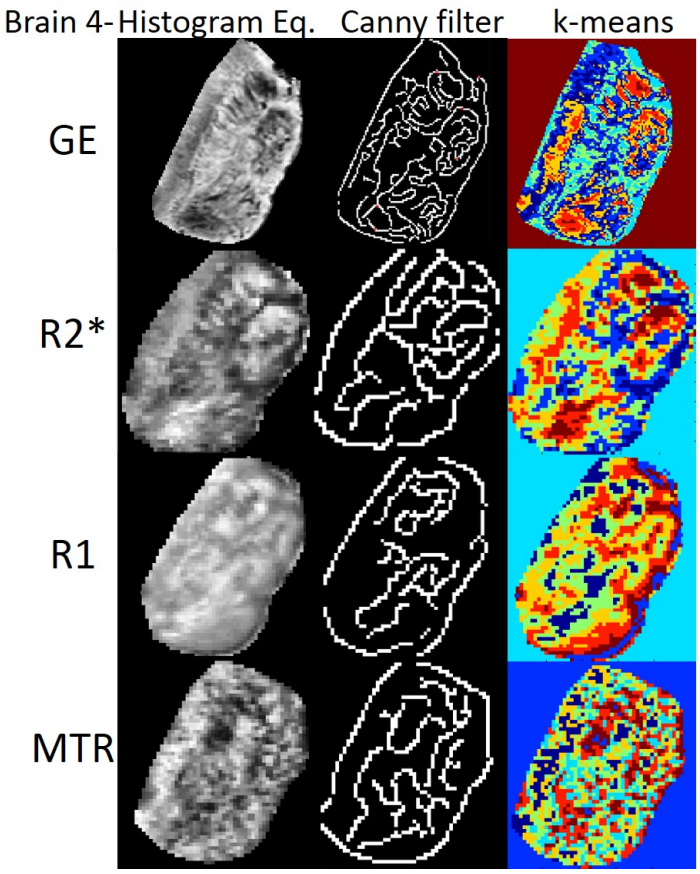

Figure 5.18: Segmented 0.3mm resolution magnitude images after histogram equalization, Canny edge detection outlines and k-means clustering (7 clusters) images for Brain 4.

only produces noisy results and has little correlation between neighbouring pixels but shows gross structure. Including spatial information reduces the noisy appearance of the clustering and meaningful groups start to emerge. Increasing the weighting factor of the spatial coordinates has the effect of smoothing the image. Including the additional contrasts causes the small groups to merge into larger groups; the resulting maps also appear smoothed, but provide a greater degree of confidence in the clustering, as the underlying contrast is derived from multiple datasets.

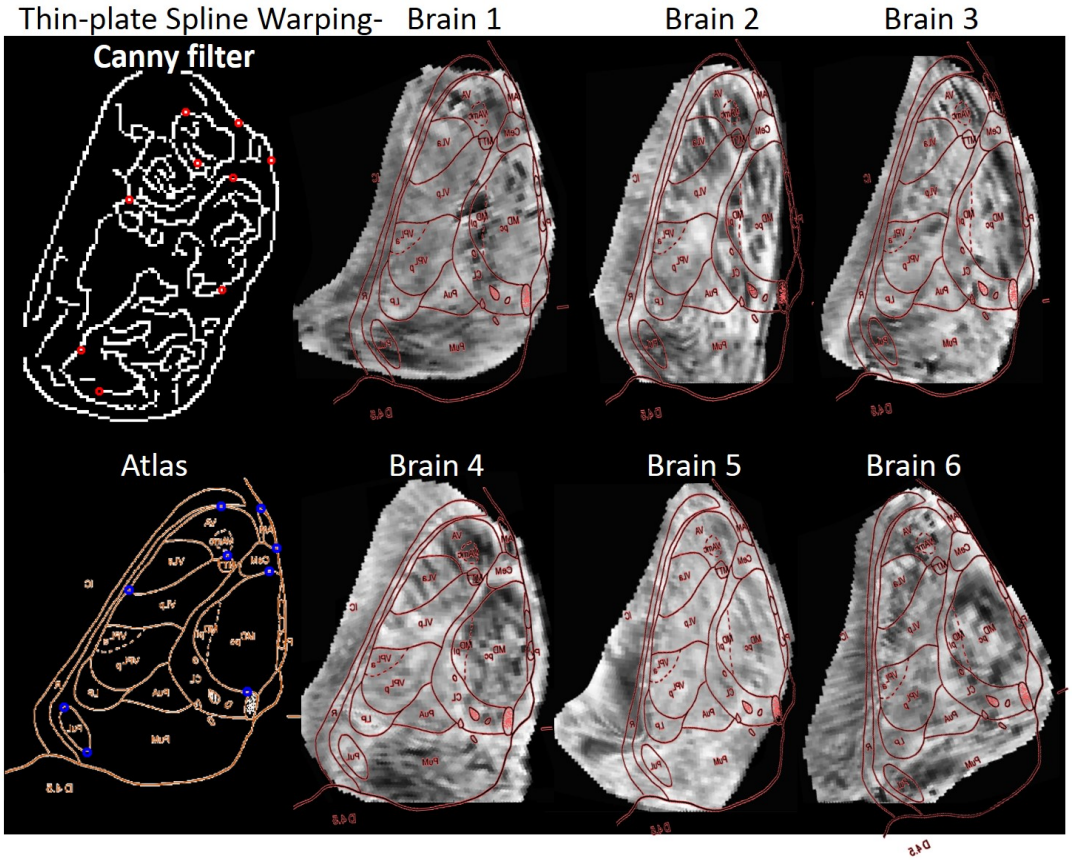

Figure 5.19: Canny edge detection with identified landmarks marked in red and corresponding landmarks marked on atlas in blue. Warped MR images with atlas overlaid for Brains 1-6.

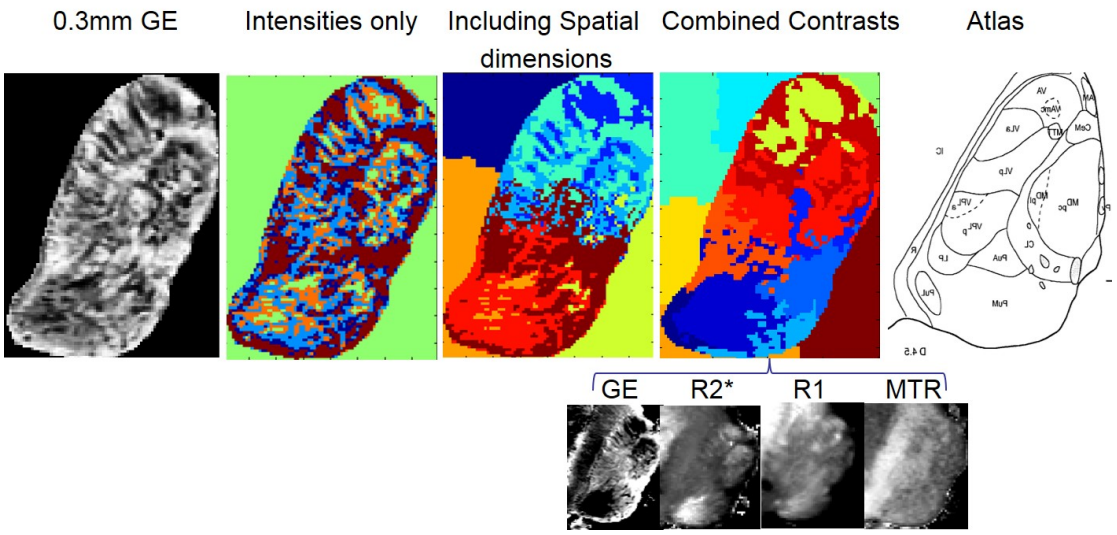

Figure 5.20: Histogram-equalised GE MRI of masked thalamus. Hierarchical clustering on pixel intensity levels and with additional dimensions of spatial coordinates and multiple contrasts.

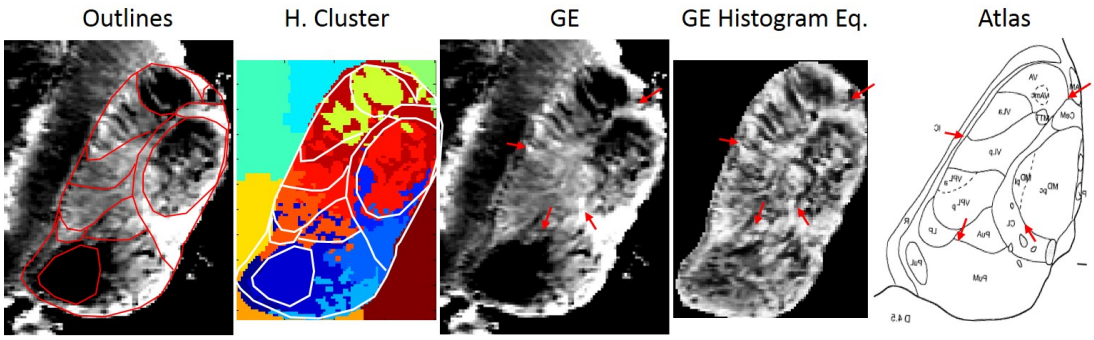

Figure 5.21: A comparison of the boundaries derived manually from the GE image, overlain on the automatically generated hierarchical clusters. The histogram-equalised GE image is included to illustrate the data that the hierarchical clustering was performed on.

Figure 5.21 shows the manual outlines from Figure 5.17 overlaid on the hierarchical clusters from Figure 5.20. The majority of the boundaries between the outlines and clusters match well, but the VA and VLa clusters are somewhat merged. Also shown are the manually windowed GE image and the histogram equalised GE, for comparison of the data to which the manual and automatic methods were applied, respectively.

5.3.3 In vivo MRI

Imaging

In Figure 5.22, the signal to noise ratio (SNR) of the images from the post-mortem brain, which was scanned at room temperature, was calculated to be 12.7, using the standard deviation of the low intensity region formed by the Fomblin filled ventricles. This was higher than the SNR of either of the in vivo brain scans which were calculated to be 8.3 and 8.6, using the standard deviation of the cerebrospinal fluid (CSF) surrounding the brain.

Figure 5.23 shows the lateral pulvinar (PuL), mediodorsal (MD) and ventral-anterior (VA) nuclei identified on post-mortem MRI were also visible on in vivo images, although the signal to noise ratio was lower than the post-mortem scans due to the restricted scanning time and subject movement.

Figure 5.24 shows a series of optimised sequences for contrast in the thalamus, across a set of healthy volunteers. These include cardiac-gated FLASH with the corresponding VSHARP filtered phase and QSM images. FSE, IR-TSE and DTI with fractional isotropy (FA) are also shown. The FLASH data is noticeably less noisy and contains better inter-nuclei contrast than the FSE images, but the contrast between the thalamus and internal capsule is much better in the FSE. The IR-TSE is significantly noisier compared to both the FLASH magnitude and FSE, however with slightly better defined

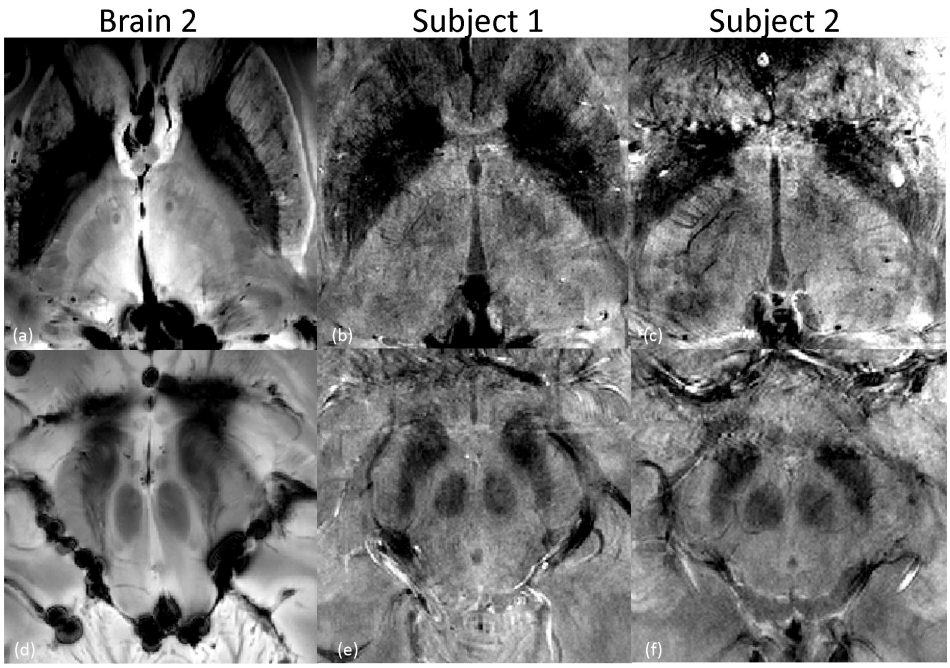

Figure 5.22: Comparison of high resolution magnitude images of thalamus and globus pallidus for (a) post-mortem Brain 2, (b) Subject 1 and (c) Subject 2 and of red nuclei and substantia nigra for (d) post mortem, (e) Subject 1 and (f) Subject 2.

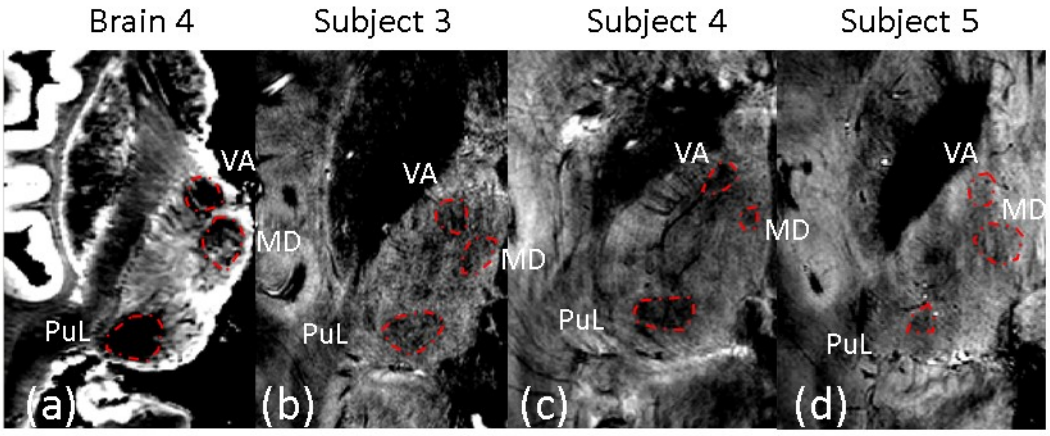

Figure 5.23: Comparison of PM and in vivo GE 3 subjects. Comparison of (a) axial post-mortem high resolution T_2*-weighted images from brain 4, with (b-d) in vivo images from three different volunteers. Consistently observed sub-regions on the in vivo images are delineated in red and were identified as the lateral pulvinar (PuL), medial-dorsal (MD) and ventral anterior (VA) nuclei.

boundaries around the edge of the thalamus.

In the DTI image, the direction of the diffusion tensor gives an indication of the fibre orientation, which is represented by the RGB colour space. The MR images show a few

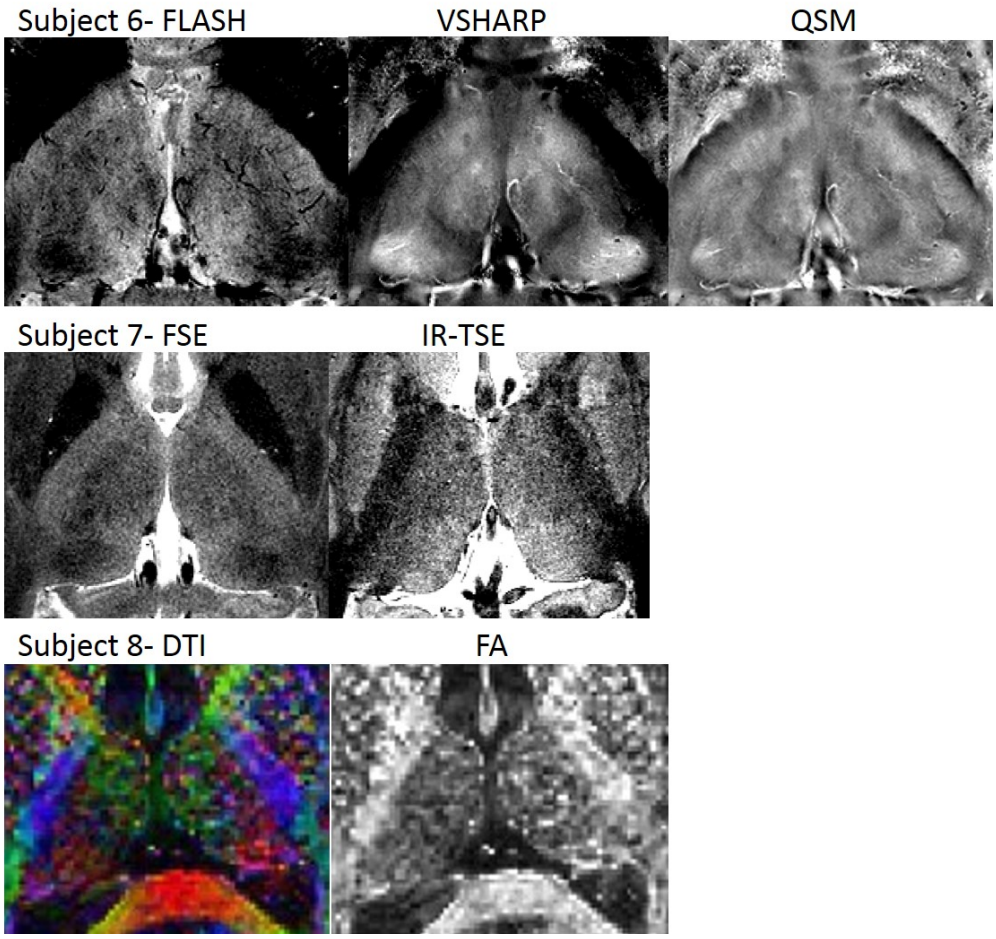

Figure 5.24: MR images from optimised sequences showing contrast within the thalamus, FLASH, VSHARP and QSM for Subject 6, FSE and IR-TSE for Subject 7, DTI for Subject 8.

distinct regions, blue for the internal capsule, red for the corpus callosum, and a gradient of green to purple going down the thalamus. These are also symmetric between the left and right side of the brain. On the other hand, the FA does not contain any useful contrast within the thalamus.

Manual Delineation

Figure 5.25 shows FLASH magnitude, FLASH QSM and FSE images for 5 healthy volunteers. Manual outlines of the nuclei are shown overlaid on the QSM data which had the most contrast and appeared the sharpest. The MTT is clearly visible, only in the QSM.

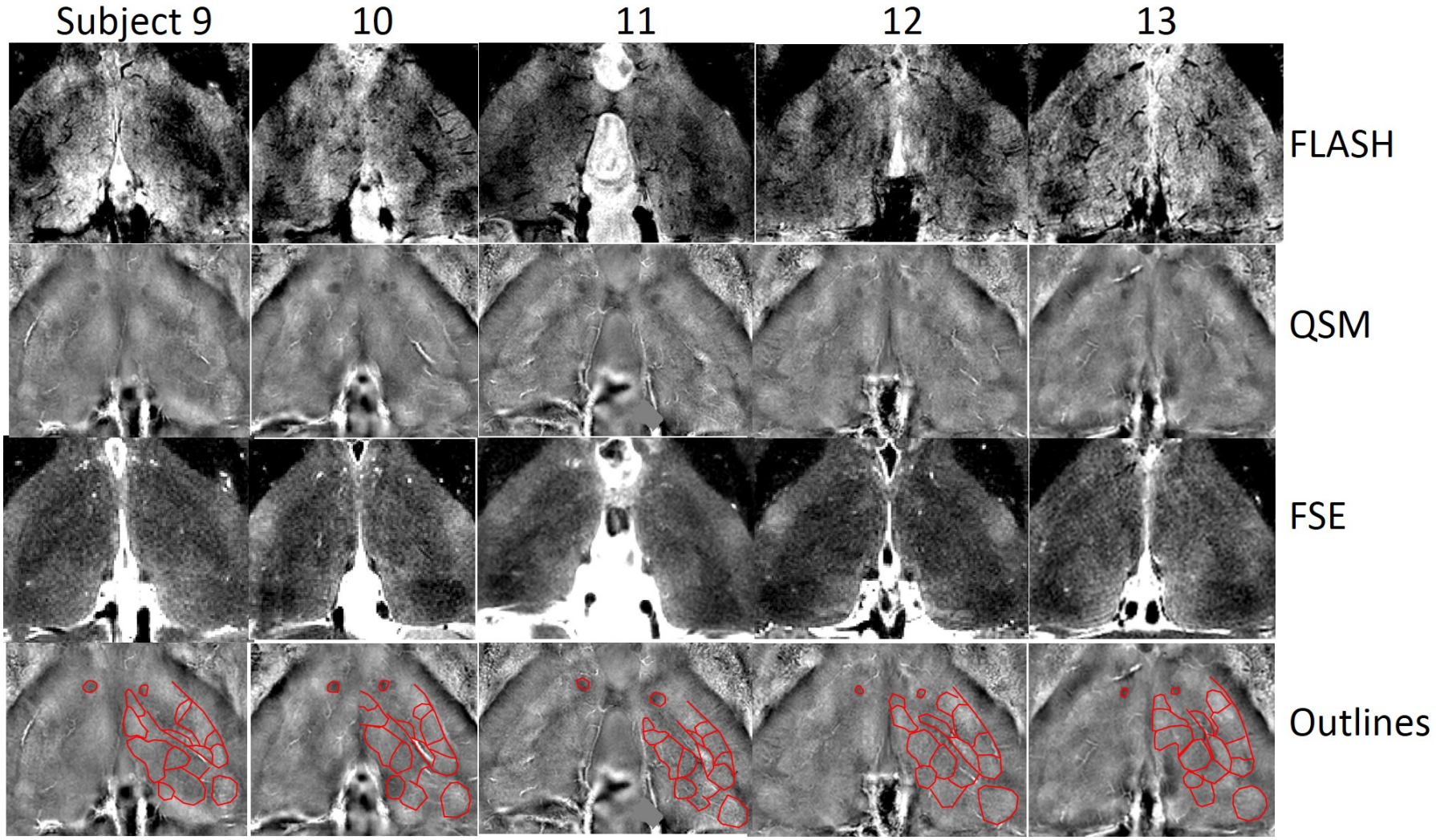

Figure 5.25: FLASH, QSM and FSE images across Subjects 9-13 with manual outlines overlain on the QSM data.

Automatic Segmentation

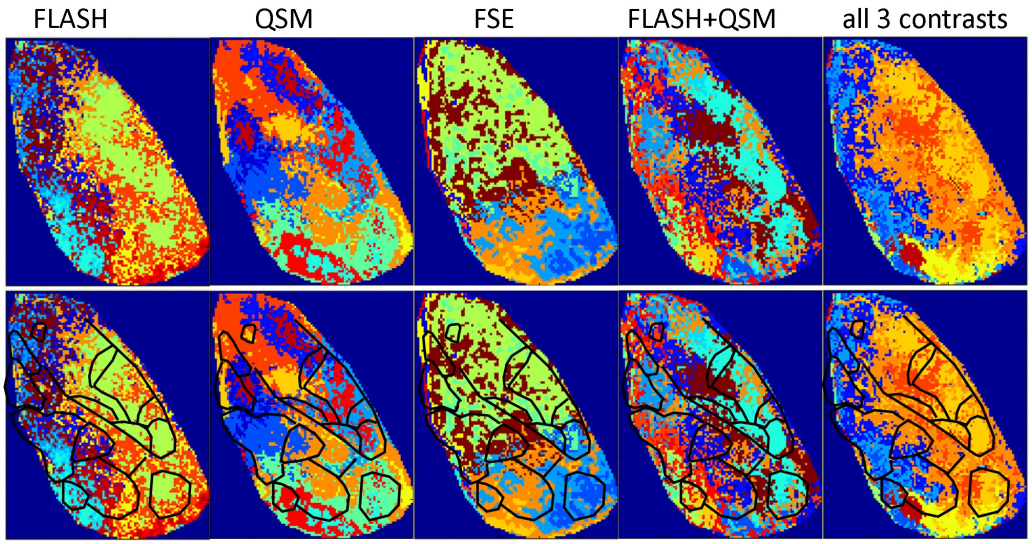

Figure 5.26: Hierarchical clustering of 2D MR images with manual intensity scaling, for Subject 9. The manual outlines are overlain on the bottom row of clusters.

Hierarchical clustering was used to produce a parcellation that could be compared to the manual outlines drawn on the in vivo data. The clustering method from the post-mortem data was altered to obtain meaningful groupings, as the spatial weighting factor had to be increased to accommodate the lower contrast.

Figure 5.26 shows the groupings produced by applying the hierarchical clustering, for Subject 9. The intensity level range of the input 2D MR images was manually scaled to match the images used for the manual outlines, rather than histogram equalised. This was done to assess the performance of the clustering relative to the annotator, with the same input data. The clustering was applied to the individual FLASH, QSM and FSE contrasts (3D: x, y, contrast), to the FLASH and QSM contrasts together (4D) and finally with all three contrasts as dimensions in the clustering matrix (5D). Overlain on a second set of clusters, are the manual outlines. Thus the clustering was applied to the same set of images as for the annotations, to compare the clustering algorithm and annotator's performances.

The clustering was also performed in 3 dimensional space, across a range of 3 slices and the z coordinates were added as additional spatial information. Figures 5.27 shows hierarchical clustering applied to the data from the 5 subjects on the individual magnitude, QSM and FSE contrasts (4D: x, y, z, contrast). The clustering was also applied to the magnitude and QSM contrasts together (5D) and finally with the addition of the FSE (6D).

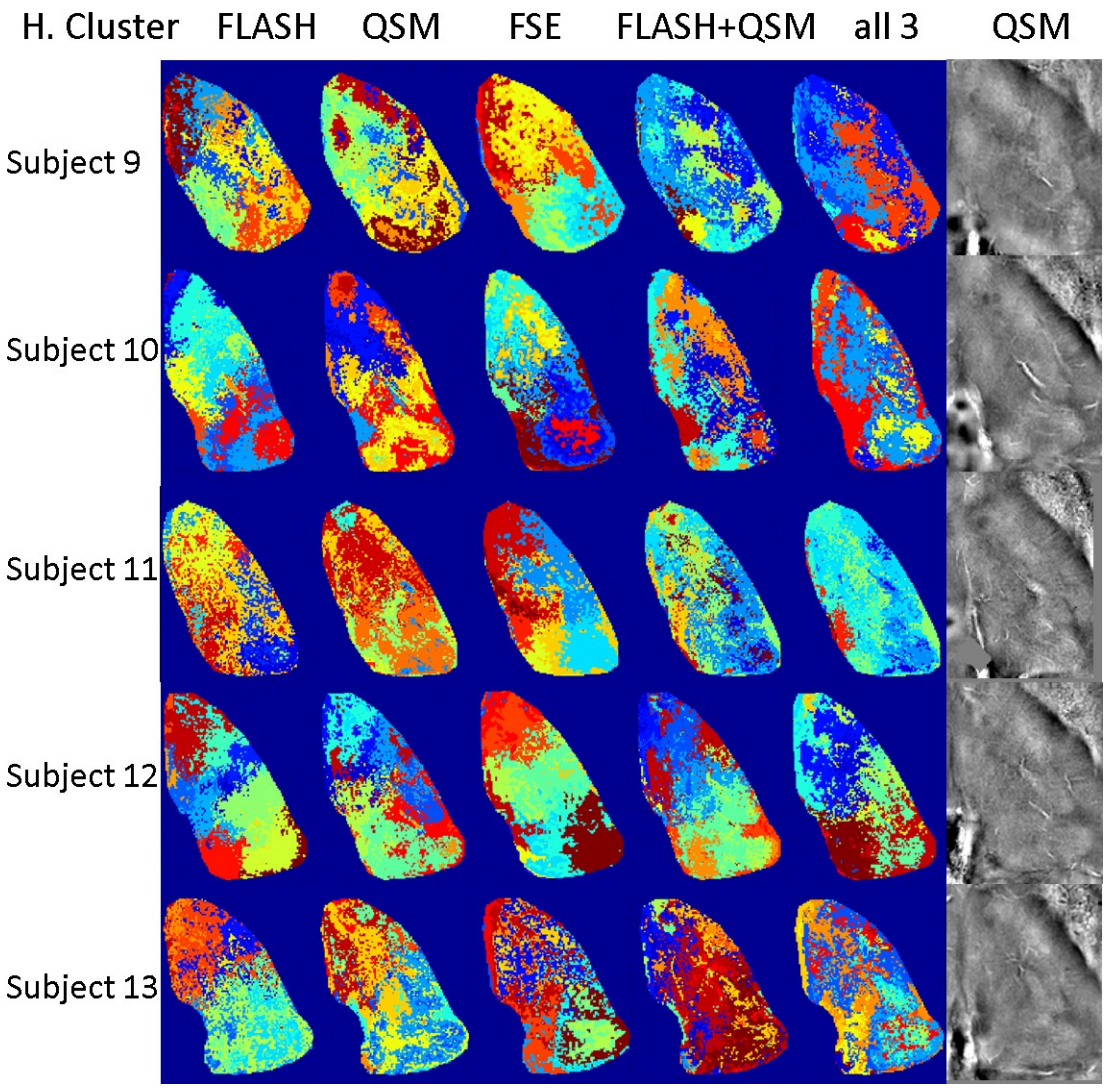

Figure 5.27: 3D hierarchical clustering of Subjects 9-13, with histogram equalisation across 3 slices. Clustering was performed on the (Left to right) FLASH, QSM, FSE, combination of FLASH and QSM, and combination of all three FLASH, QSM and FSE contrasts.

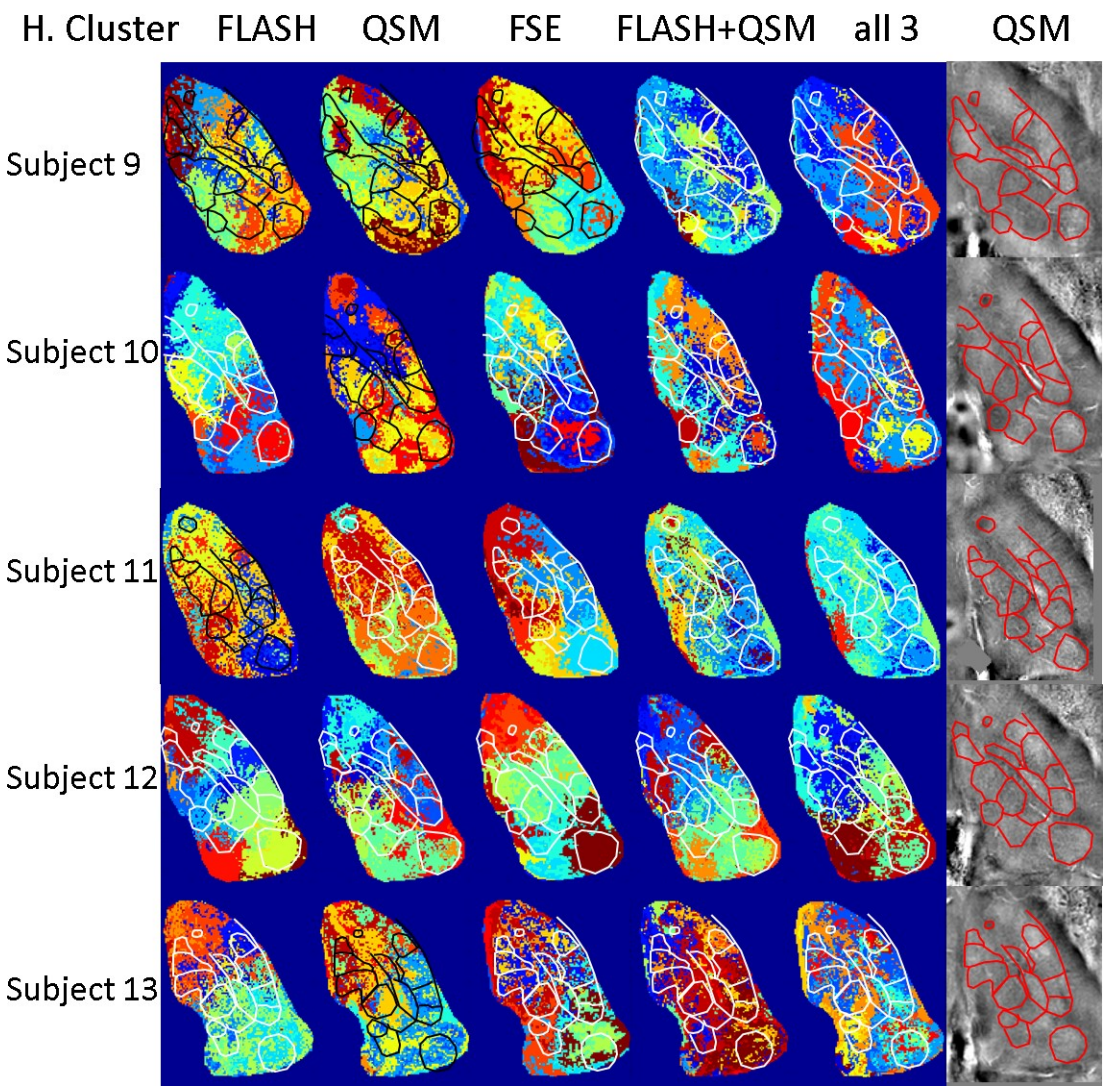

Figure 5.28: Hierarchical clustering with manual outlines overlaid.

Nucleus	FLASH	QSM	FSE	FLASH+QSM	All 3
MTT	2	5	1	3	3
VLa	5	4	3	3	4
VLp	5	4	5	4	3
VPLa	4	3	3	2	3
VPLp	4	5	4	5	5
VPMpc	3	2	1	3	0
VPM	3	4	2	4	5
MV	2	2	3	4	3
CeM	3	4	1	4	2
Pf	3	3	3	3	2
CM	3	5	4	4	4
PuA	3	4	3	3	4
Po	4	5	5	3	3
Li	3	4	2	5	1
PuL	5	5	5	5	5
Average	3.5	3.9	3.0	3.7	3.1

Table 5.4: Ratings of the plausibility and distinction of the hierarchical clustering of each nuclei, across the in vivo imaging contrasts. 1 point was given for each subject (for a total maximum score of 5).

Figure 5.28 shows the manually delineated outlines (Figure 5.25) overlaid on the groupings from hierarchical clustering (Figures 5.27), to compare the difference between the in vivo boundaries.

The ratings of the nuclei identified in the different clusters, out of 5 subjects, are given in Table 5.4. The nuclei were given 1 point per subject, for a maximum of 5 points, if either the majority of the boundaries and area of the manual outlines and clusters overlapped or if the clusters would help to redefine the location of the manual outlines, e.g. if the cluster was consistently identified, but displaced from the manual outlines. The VM and PuM are open ended and the sPf was not identifiable from the MR images during the process of drawing the manual outlines, so these were not rated.

5.4 Discussion

5.4.1 Histology

Imaging

In Figure 5.10, the MRI data contained more regional variation in intensity rather than the distinct boundaries of the stains. In the histology, only one factor is stained for, whereas in T_2* weighted images, the contrast is influenced by multiple factors. Correlation of coronal post-mortem MRI with histology allowed detection of multiple corresponding nuclei. The nuclei were identified by finding distinct boundaries or regional changes in intensity. The CM and AV nuclei were particularly distinct regions in both the stains and coronal MRI. However, the boundary between the LP and VPLa is unclear on the stains, whereas it is more distinct on the MRI.

Morel used parvalbumin, calbindin and calretinin stains to segment the thalamus through histology [3]. Calcium and calcium binding proteins have little MR contrast. Therefore the LFB stain is much more relevant as myelin produces an MR contrast through its magnetic susceptibility. This can also be detected indirectly using a variety of techniques as described in Section 5.1.1.

Automatic Segmentation

The aim of the clustering and edge detection in Figure 5.11 was to highlight the edges of the nuclei independently, without bias from the annotator's knowledge of the expected structure from the atlas. The groupings from the clustering of the MR data are consistent with the stain and the atlas.

In the coronal plane, the inferior edge of the thalamic anatomy is not defined with a clear boundary. Thus selecting the edge around the bottom of the thalamus mask is difficult. The more inferior nuclei can be cut off or too much extra surrounding tissue can be included, which decreases the quality of the clustering.

The additional edges in the Canny edge detection can be confused with the actual boundaries of the nuclei, so Canny edge detection is not suitable for highlighting the boundaries of the nuclei by itself.

Histology contained the best possible contrast and highest degree of detail, producing the most confident delineation of the thalamic nuclei. Post-mortem MRI had good overall contrast, thus realistically detailing the thalamic nuclei and providing a possibility of visualising the nuclei in 7T in vivo MR imaging.

5.4.2 Post-mortem MRI

Imaging

In Figure 5.13, thalamic structure was consistently observed across brains of different post-mortem ages and conditions and the constituent nuclei were identified in the ax-

ial post-mortem GE image. The bottom left hypointense region was identified as the pulvinar (Pu), the semicircular structure along the middle of the right-hand edge was identified, using the slice from the atlas in Figure 5.17, as the mediodorsal (MD) nucleus and the band along the edge was identified as the lateral-posterior (LP) nucleus, ventral-lateral (VL) nucleus, ventral-posterior lateral (VPL) nucleus, ventral-anterior (VA) nucleus and anteromedial (AM) nucleus.

From Brains 3-8, Brain 6 showed the best contrast and most well defined structure so outlines were drawn around the identifiable nuclei. The handling and storage conditions of the tissue were similar across the brains, except Brain 7 which appeared to have become deformed during storage. Also the contrast between the nuclei in Brain 7 was the worst.

Any angulation of the slices would also cause the images to become skewed. The MR images were not always exactly aligned with the anterior-posterior commissure plane as the atlases were, due to restricted visibility in the survey scans.

Correlation of Contrast in Histology and Post-mortem MRI

In Figure 5.14, the thalamic nuclei were manually delineated with strong confidence, as the LFB stain contained dark boundaries. The underlying contrast of the LFB stain is myelin, which the post-mortem MRI was compared with and also contained many hypointense regions. Myelin in the thalamus causes the signal to decay more rapidly, in this T_2*-weighted scan. The MRI also contained a few brighter regions which were similar to the lighter regions of the stain. Thus MR sequences optimised for high white matter and low grey matter content would be desirable.

In Figure 5.15, the points in the T_1 against LFB plot that deviate from the linear fit, have elevated T_1 values which appear to originate from the bright fixation front along the lateral edge of the thalamus. This also applies to the T_1 against MTR plot in Figure 5.16, where the MTR map appears slightly darker along the edge of the thalamus. The effect of fixation is much stronger for the T_1 values compared to MTR.

The effect of the fixation front is inverted for the R_1 values in the R_2* against R_1, from the axial post-mortem images. The R_2* and susceptibility values appear to be much less affected by the fixation front as fewer points deviate from the linear fit. The T_1 map was directly correlated with the LFB, therefore the MTR, R_2* and susceptibility were indirectly linked to the LFB by the T_1 and R_1 values.

The correlation of values between the different image contrasts required registration of the 2D stains to 3D MR data, in order to account for differences in angulation and any deformation of the tissue. This was challenging so a 2D to 2D registration was used on best matching slices instead, which performed acceptably.

Manual Delineation

In Figure 5.17, all of the nuclei from the corresponding atlas slice were outlined in the GE, with a high degree of confidence. However, the exact position of the boundaries between nuclei in certain subgroups, particularly along the lateral edge can be ambiguous due to the texture of the image, in which case the boundaries can be manually placed based on where they are expected to be, based on the atlas. The MTR image was more blurry due the point spread function requiring optimisation.

Automatic Segmentation

In Figure 5.18, k-means clustering generally highlighted the regions that were also detected visually, particularly on the T_2*-weighted images and R_2* maps, but the voxels contained in each cluster were spread out, thus highlighting multiple nuclei per cluster. The Canny edge detection identified some boundaries, but was confounded by noise.

In Figure 5.19, the thin-plate spline warping could be used to guide non-linear registrations, but was not suitable for systematically identifying the nuclei, as the MRI was effectively forced to fit the higher resolution atlas image. The distance between the slices in the atlas (0.9mm) was larger than the slice thickness (0.33mm) so only a fraction of the MR images were in-line with the atlas. Overall, there was not enough information to support the manual outlines or to provide any additional details.

As part of the development of an automatic segmentation technique to systematically identify the boundaries of the thalamic nuclei, the automatic segmentation technique was decided upon, with the optimisation of a hierarchical clustering algorithm. In Figure 5.20, upon comparison with the atlas, the hierarchical clustering with spatial information and combined contrasts correlated best. The majority of the information came from the GE and R_2*. The R_1 and MTR added little, as was the case for manual annotations.

Comparison of Manual Delineation and Automatic Segmentation

In Figure 5.21, the contrast in the post-mortem images was significant enough to produce convincing groupings with the hierarchical clustering. In the manually windowed GE image data, the lower intensity limit was set higher to minimise the texture in the PuL and VA, so as to effectively flatten the intensity profile of the regions.

The use of edge detection or clustering techniques depends on the type of contrast within the image. If the intensity is homogeneous across the regions, but boundaries are clear, then edge detection may be preferable. If there are no distinct boundaries but the intensity levels are different between regions, then clustering would be better. Hierarchical clustering with spatial information worked well in both cases.

The automatic segmentation techniques serve to corroborate the location of the boundaries of the nuclei. They can also serve to guide the manual annotation of the images, alongside the other contrasts. As the contrast is low, prior knowledge of the structure is

required, which is a limitation for both manual and clustering segmentations.

5.4.3 In vivo MRI

Imaging

In Figure 5.22 and Figure 5.23, the amount of detail in the images of the post-mortem brain was also higher. This is partially due to the higher SNR but also due to the complete absence of motion. As the slice thickness was increased to reduce the in vivo scanning time, the detail of thin structures is reduced. Despite the 3 times larger in vivo voxel volume, the SNR was still lower than the post-mortem SNR as the number of signal averages for the post-mortem was 4 times higher. Also, the substantia nigra look more similar across the three brains compared to the globus pallidus. The different amounts of cerebellum visible in each of the three brains indicates that the slices were taken with different angulations.

Overall, GE in vivo images suffer from limitations of SNR, movement and susceptibility artefacts from sinuses compared to post-mortem. Preliminary in vivo measurements suggest that some of the thalamic features identified post-mortem can also be seen in vivo, but alternative contrasts need to be explored requiring different imaging sequences.

From the imaging protocol of optimised sequences in Figure 5.24, the FLASH sequence had the highest in-plane resolution, thus the most detail compared to the FSE, IR-TSE and the DTI had the lowest resolution. However the QSM contained the greatest contrast and is more appropriate than the VSHARP filtered phase, as the QSM accounts for non-local phase variations. The cardiac-gating also increased the image quality as it reduced the blurring of the images. After assessing the thalamic contrast, an imaging protocol was constructed from the optimised FLASH and FSE sequences, as the QSM contained the most satisfactory boundaries, followed by the FLASH magnitude and FSE.

Manual Delineation

In Figure 5.25, all of the nuclei were identified consistently across the contrasts and subjects, within natural variation, but this process was more difficult in Subject 3 and in the FLASH magnitude and hardest in the FSE. The boundaries of the nuclei are not immediately obvious upon looking at the images. They become clearer as the image is segmented into groups of nuclei and further into nuclei. The exact position of some of the boundaries can be unclear along the band of nuclei on the right edge due to the texture of the image. The divisions of the subgroup into nuclei could be placed along multiple different lines which is narrowed down by comparing with the other contrasts. The FLASH and FSE have slightly different contrasts which allows this differentiation.

Automatic Segmentation

In Figure 5.26, overall, the manual outlines matched with the boundaries of the manually windowed clusters best for the FLASH, then the three combined contrasts, QSM, two combined contrasts and worst for the FSE. The clusters from the three combined contrasts did provide better segmentation of the nuclei compared to the FLASH, in the ventral and lateral groups of nuclei.

In Figures 5.27, the FSE increases the quality of clustering for some nuclei, such as the VPM, whereas noise in the FSE and registration errors between the contrasts, causes the clustering of other nucleus to more often become worse. The inclusion of the adjacent slices and the histogram equalisation of the intensity window also improved the clustering, compared to the manually windowed clusters in Figure 5.26.

The segmentation of nuclei in vivo is a greater challenge, as the contrast is lower and noise is higher compared to post-mortem. As the parameters were adjusted, care needs to be taken that the spatial weighting is balanced between reducing noise and losing details in the clustering. Clustering was limited to a predetermined number of clusters rather than being variable depending on the information in the images. Additionally, there could be a need for further reduction in motion during in vivo scans to gain clearer details.

Comparison of Manual Delineation and Automatic Segmentation

The average of the ratings per contrast in Table 5.4 was calculated and the clusters of the QSM matched best with the outlines, followed by the FLASH and FSE, as observed during the process of drawing the manual outlines. The combined FLASH and QSM scored second highest overall so it provides better segmentation than the individual FLASH or FSE images but was still worse than just the QSM data. The three combined contrasts performed second worst on average and only slightly better than the individual FSE.

The combinations of contrasts (the FLASH and QSM, and also the FLASH, QSM and FSE) can be used to guide or to verify the position of the manual outlines. For the clustering, the image intensities were histogram-equalised to increase the contrast but this can cause noise to be amplified. For the manual outlines, the images were narrowly windowed to visualise the nuclei. The actual contrast of the images is much lower.

Overall, for manual outlines and automatic clustering, the manual outlines were performed with a higher degree of confidence as the multiple contrasts provided adequate detail to delineate all of the nuclei within the slice, for post-mortem and in vivo MRI. The hierarchical clustering provided the best segmentation. It worked well on the post-mortem images, but performed worse for in vivo data due to the reduction in SNR.

Comparison of Clustering Performance with Literature

The obtained QSM data appeared similar to the 7T QSM images by Deistung et al. [6] (Figure 5.2). The manual delineation of the thalamic nuclei was performed with a similar process to the automated process used in the shape models by Liu [15] (Figure 5.5), of dividing regions in the image repeatedly until the structure of the nuclei was reached.

In this project, k-means clustering didn't perform as well as in the multi-contrast head model [13] or the k-means clustering applied to the 8 subject averaged 1.5T T_1 and T_2 weighted images [14], in Figure 5.5. However, the hierarchical clustering performed similarly to these.

5.5 Conclusion

The thalamic nuclei were identified in the histology and corresponding post-mortem MR images with reference to the atlas. An anatomical structure consisting of groups of nuclei was consistently observed across the post-mortem brains with different ages and conditions, and across the in vivo subjects. These groups were divided into sub-regions to delineate and identify the thalamic nuclei with a high level of confidence in the histology, post-mortem MRI and in vivo MRI. Hierarchical clustering with spatial information and multiple contrasts produced the best agreement with the manual delineations.

The contrast and signal to noise ratios of the post-mortem images were better than the optimised in vivo scans. The presence of blood flow and head movement increased the noise in vivo. The QSM data contained the greatest contrast between the thalamic nuclei and the QSM obtained from the cardiac-gated FLASH was preferred to QSM from the 3D gradient echo sequence. The manual outlines of the in vivo data matched well with the hierarchical clusters, but the clustering for in vivo was relatively less well defined than the post-mortem clusters. In future, the quality of the in vivo images could be improved by reducing noise from movement and to further optimise the sequences to increase contrast.

The 5 post-mortem datasets could be used to create a thalamic atlas. Comparison of histology and MR data could be used to investigate the origins of contrast in the thalamus. Finally, the thalamic outlines could be used to correlate the anatomical structure with areas of activation in the thalamus, from fMRI measurements.

Bibliography

[1] Thomas Tourdias, Manojkumar Saranathan, Ives R Levesque, Jason Su, and Brian K Rutt. Visualization of intra-thalamic nuclei with optimized white-matter-nulled MPRAGE at 7T. *Neuroimage*, 84:534–545, 2014.

[2] Jean-Jacques Lemaire, Jérôme Coste, Lemlih Ouchchane, François Caire, Christophe Nuti, Philippe Derost, Vittorio Cristini, Jean Gabrillargues, Simone Hemm, Franck Durif, et al. Brain mapping in stereotactic surgery: a brief overview from the probabilistic targeting to the patient-based anatomic mapping. *Neuroimage*, 37:S109–S115, 2007.

[3] Anne Morel, Michel Magnin, Daniel Jeanmonod, et al. Multiarchitectonic and stereotactic atlas of the human thalamus. *Journal of Comparative Neurology*, 387(4):588–630, 1997.

[4] John F Schenck and Earl A Zimmerman. High-field magnetic resonance imaging of brain iron: birth of a biomarker? *NMR in Biomedicine*, 17(7):433–445, 2004.

[5] B Bender, C Mänz, A Korn, T Nägele, and U Klose. Optimized 3D magnetization-prepared rapid acquisition of gradient echo: identification of thalamus substructures at 3T. *American Journal of Neuroradiology*, 32(11):2110–2115, 2011.

[6] Andreas Deistung, Andreas Schäfer, Ferdinand Schweser, Uta Biedermann, Robert Turner, and Jürgen R Reichenbach. Toward in vivo histology: a comparison of quantitative susceptibility mapping (QSM) with magnitude-, phase-, and R2*-imaging at ultra-high magnetic field strength. *Neuroimage*, 65:299–314, 2013.

[7] Jerzy Olszewski, Donald Baxter, et al. Cytoarchitecture of the human brain stem. *Cytoarchitecture of the human brain stem.*, 1954.

[8] Georges Schaltenbrand. Atlas for stereotaxy of the human brain. *Georg Thieme*, 1977.

[9] Rebecca F Gottesman and Argye E Hillis. Predictors and assessment of cognitive dysfunction resulting from ischaemic stroke. *The Lancet Neurology*, 9(9):895–905, 2010.

[10] Ulas Ziyan, David Tuch, and Carl-Fredrik Westin. Segmentation of thalamic nuclei from DTI using spectral clustering. In *International Conference on Medical Image Computing and Computer-Assisted Intervention*, pages 807–814. Springer, 2006.

[11] Laura Serra, Mara Cercignani, Giovanni A Carlesimo, Lucia Fadda, Nadia Tini, Giovanni Giulietti, Carlo Caltagirone, and Marco Bozzali. Connectivity-based parcellation of the thalamus explains specific cognitive and behavioural symptoms in patients with bilateral thalamic infarct. *PloS One*, 8(6):e64578, 2013.

[12] U Klose, K Gorczewski, M Erb, and W Grodd. Image processing and visualization. *Int J CARS*, 2(1):S82–S133, 2007.

[13] Maria Ida Iacono, Esra Neufeld, Esther Akinnagbe, Kelsey Bower, Johanna Wolf, Ioannis Vogiatzis Oikonomidis, Deepika Sharma, Bryn Lloyd, Bertram J Wilm, Michael Wyss, et al. Mida: a multimodal imaging-based detailed anatomical model of the human head and neck. *PloS One*, 10(4):e0124126, 2015.

[14] Sean CL Deoni, Brian K Rutt, Andrew G Parrent, and Terry M Peters. Segmentation of thalamic nuclei using a modified k-means clustering algorithm and high-resolution quantitative magnetic resonance imaging at 1.5T. *Neuroimage*, 34(1):117–126, 2007.

[15] Yuan Liu, Pierre-François D'Haese, Allen T Newton, and Benoit M Dawant. Thalamic nuclei segmentation in clinical 3T T1-weighted images using high-resolution 7T shape models. In *SPIE Medical Imaging*, pages 94150E–94150E. International Society for Optics and Photonics, 2015.

[16] Joshua V Stough, Chuyang Ye, Sarah H Ying, and Jerry L Prince. Thalamic parcellation from multi-modal data using random forest learning. In *Biomedical Imaging (ISBI), 2013 IEEE 10th International Symposium on*, pages 852–855. IEEE, 2013.

[17] Mariano Cabezas, Arnau Oliver, Xavier Lladó, Jordi Freixenet, and Meritxell Bach Cuadra. A review of atlas-based segmentation for magnetic resonance brain images. *Computer Methods and Programs in Biomedicine*, 104(3):e158–e177, 2011.

[18] Michael E Calhoun, Mathias Jucker, Lee J Martin, Gopal Thinakaran, Donald L Price, and Peter R Mouton. Comparative evaluation of synaptophysin-based methods for quantification of synapses. *Journal of Neurocytology*, 25(1):821–828, 1996.

[19] DR Enzmann and NJ Pelc. Brain motion: measurement with phase-contrast MR imaging. *Radiology*, 185(3):653–660, 1992.

[20] John Canny. A computational approach to edge detection. In *Readings in Computer Vision*, pages 184–203. Elsevier, 1987.

[21] James MacQueen et al. Some methods for classification and analysis of multivariate observations. In *Proceedings of the Fifth Berkeley Symposium on Mathematical Statistics and Probability*, volume 1, pages 281–297. Oakland, CA, USA, 1967.

[22] Daniel Defays. An efficient algorithm for a complete link method. *The Computer Journal*, 20(4):364–366, 1977.

Chapter 6

Atlas of Large Vessels in The Brain

6.1 Introduction

The brain is the most metabolically active organ in the body by weight, accounting for approximately 2% of the body mass, but consuming about 20% of the oxygen supply [1]. Therefore, it requires a significant supply of blood, about 15% of the cardiac output, to provide the nutrients and oxygen needed for it to function properly [2]. The brain is serviced by a complex network of arteries, veins and capillaries which supply oxygenated blood to the brain tissue and drain the deoxygenated blood. Damage to these, for example in the form of aneurysms or haemorrhages, results in loss of functionality and is the basis of some cerebrovascular diseases.

Understanding the distribution of venous blood vessels in the brain via production of an atlas of venous blood vessels would be of some value. A number of diseases have a cerebrovascular component e.g. vascular dementia and multiple sclerosis [3, 4, 5]. Applications of a venous atlas include assessing the development and atrophy of small veins in white matter to detect abnormalities from cerebrovascular diseases [6, 7], and guiding surgical planning for intervention in the case of venous malformations [8].

Aims: To create an MRI-based atlas of venous density and to distinguish small vessels in white matter. To compare the variation and overlap of veins and arteries, across subjects. To utilise the vessel maps in oximetry measurements.

In this chapter, the generation of contrast between the susceptibility of the blood and tissue is described. Methods of vessel imaging to provide anatomical information and oxygenation measures are outlined. A description of the optimisation for the imaging and segmentation techniques of the vessels is given. The calculation of the atlas, overlap maps and susceptibility values of the vessels are explained. The results from the optimisation and segmentation are shown, and the methods for the reduction of artefacts in the venous segmentations are compared. The variation in the distribution, image quality and overlap of the veins and arteries was compared across subjects. Additionally, the venous atlas is presented. The susceptibility values of the vessels are plotted against a range of categories including varying radii and locations within the grey and white matter.

6.1.1 Susceptibility of Blood

Imaging of the venous blood is possible due to its susceptibility difference from the surrounding tissue. Deoxyhaemoglobin acts as an intrinsic paramagnetic contrast agent which is found in venous blood. On the other hand, oxyhaemoglobin is diamagnetic. Therefore the susceptibility of blood depends on the oxygenation levels, which gives rise to the BOLD (blood oxygen level dependent) effect [9] that is exploited in functional MRI. The susceptibility difference between venous blood and surrounding tissue can be used to enhance contrast in magnitude images, for example in susceptibility weighted imaging (SWI) [10], and it is also possible to measure this effect using quantitative susceptibility mapping (QSM) [11], as described in Chapter 2.

Imaging of blood vessels

In MR angiography, contrast is generated from the flow of blood. In time of flight (TOF) angiography, a gradient echo sequence is used, with a short repetition time and small flip angle. The stationary spins within the imaging volume experience many RF pulses, reducing their longitudinal magnetisation, until it reaches a steady state. Moving spins from outside of the imaging volume flow in, and since they have experienced fewer RF pulses, they retain a much larger magnetisation compared to the stationary tissue. The contrast is generated from the magnitude of the replenished magnetisation of the inflowing blood. In phase contrast angiography (PCA), the flow of blood is encoded using a bipolar gradient, which generates a net phase shift, as the spins move through different portions of the gradient field. The phase shift is proportional to the displacement of the spins, thus enabling the calculation of the velocity. For stationary spins, the effect of the bipolar gradients cancel and the net phase difference is zero [12]. In contrast, venograms are typically performed as minimum intensity projections (mIP) of susceptibility weighted images (SWI), from a GE sequence with a long echo time [13]. In SWI, the veins appear dark against a bright tissue background.

The motivation for imaging blood vessels at higher field strengths is justified, as the contrast to noise ratio (CNR) between the vessels and background tissue increases by 83-88$\%$ at 7T compared to 3T, allowing visualisation of smaller vessels [15]. The visualisation of veins benefits much more from higher field strength than arteries [16], due to the greater susceptibility difference of venous blood compared to tissue.

Venograms and oxygen saturation maps have been calculated at 3T from QSM maps by Fan et al. [14], as shown in Figure 6.1. QSM allows the calculation of oxygenation values of vessels that are not parallel to the magnetic field, as was the limitation of previous MR susceptometry techniques [17, 18, 19]. The oxygen saturation (SvO_2) of the blood is related to its susceptibility difference from tissue, $\Delta\chi_{blood}$, by

$$\Delta\chi_{blood} = \Delta\chi_{DO} \times Hct \times (1 - SvO_2) + \Delta\chi_O \times Hct \tag{6.1}$$

where, Hct (haematocrit) is the fraction of blood that consists of red blood cells, determined experimentally to be about 0.4 [20], $\Delta\chi_{DO}$=0.27ppm (cgs) [21], $\Delta\chi_O$=-0.03ppm (cgs) [22] and SvO_2 is expected to be around 0.61 ± 0.06 in venous blood [23].

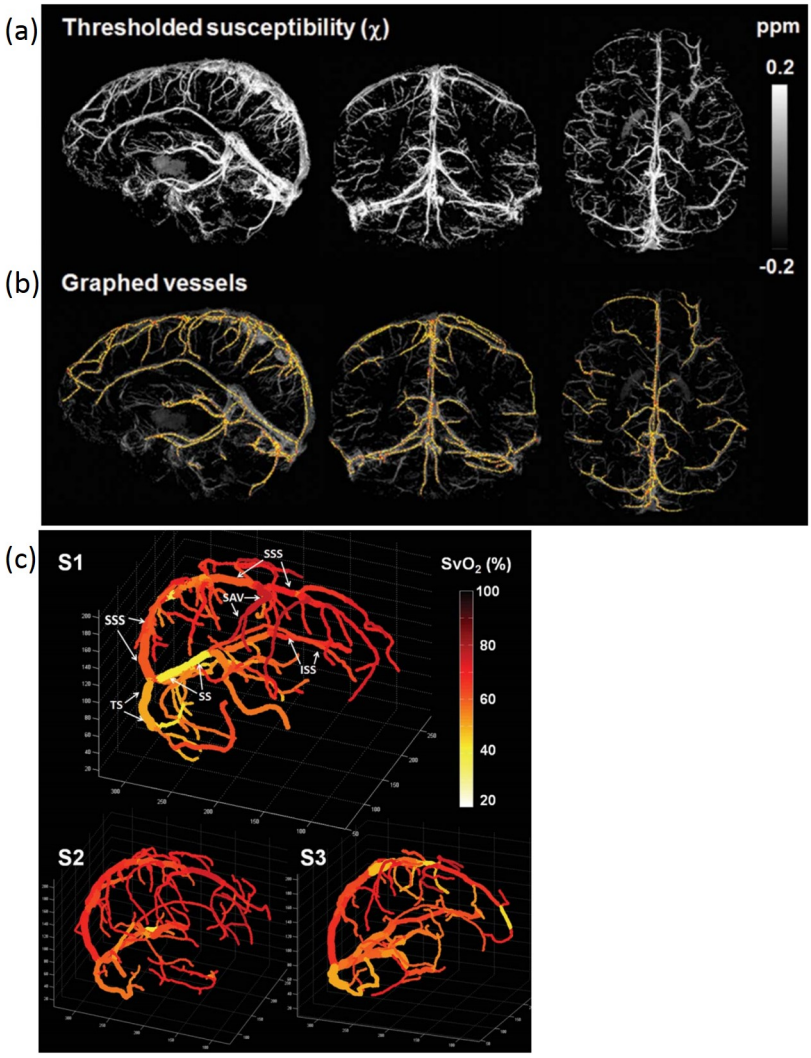

Figure 6.1: a) Thresholded quantitative susceptibility maps showing the deoxygenated blood and iron rich structures. b) vectorised vessels from thresholded QSM c) oxygen saturation maps, for 3 subjects, calculated from QSM maps at 3T by Fan et al. [14].

Fan et al. also used numerical simulations to determine the percentage error from the method of QSM regularisation and from the angle of the vessel with respect to the magnetic field. L_1 regularisation resulted in an error of less than 10% across all vessel orientations.

In order to segment the cerebral vessels to create a venous atlas, a commonly used approach has been a Hessian-based (Frangi) filter [25] and thresholding technique [26]. This has been demonstrated in a number of studies, including on SWI data [27], QSM data [28] and TOF data [29]. These approaches are limited by the contrast and artefacts in the underlying data.

Alternatively, Ward et al. produced an anatomical atlas by manually tracing 0.9mm resolution 3T GE SWI images from 10 volunteers [24]. A vein atlas was produced by interpolating the manual tracings into MNI space and then averaging. Additionally,

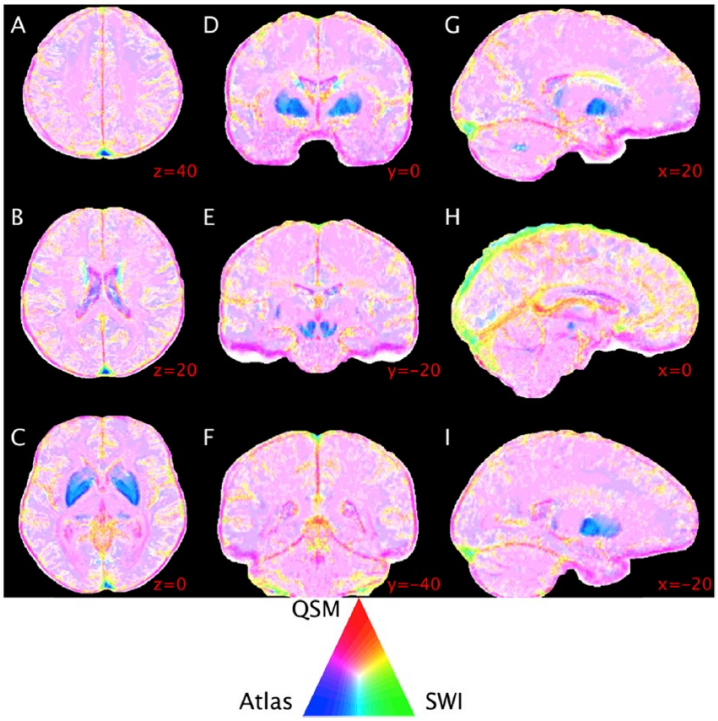

Figure 6.2: Overlap of venous segmentations from manually traced atlas and normalised SWI and QSM data, across 10 volunteers at 3T, by Ward et al. [24].

SWI and QSM data were normalised using a Gaussian mixture model, with vein and non-vein components. The vein atlas and normalised SWI and QSM data were combined to produce a composite vein image, as shown in Figure 6.2. The composite vein image provided more accurate automatic segmentation than using either the SWI or QSM data on their own, as measured using the Cohen's D metric [24].

6.2 Method

Imaging sequences were optimised to provide the best visualisation of the cerebral veins and arteries. The segmentation of the images to produce vessel maps, is described. The overlap of the veins and arteries was calculated. The venous maps were used to isolate the susceptibility values (in SI units) of the veins and the maps were also averaged to produce an atlas of the venous structure. All subjects were scanned with ethical approval from the University of Nottingham Medical School Ethics Committee.

6.2.1 Optimisation and Segmentation

A series of imaging sequences, including phase contrast angiography (PCA), time of flight (TOF) and a 3D gradient echo (GE) to obtain SWI data, were optimised on healthy volunteers (Subjects 1-3, male/female=1/2, age=25.7$\pm$1.5) and compared for venous and arterial contrast. The parameters for the PCA and TOF were chosen to suppress the signal from background tissue and to enhance the signal from the blood vessels, and vice versa for the SWI. In the TOF sequence, the volume was divided into a series of smaller chunks. The magnetisation of the blood becomes saturated as it flows through the chunks and thus its signal intensity is reduced. The number of chunks in the TOF was varied to match the tissue signal intensity between the edges of adjacent chunks [12].

A high in-plane resolution was initially chosen to maximise sharpness, in order to identify the smallest possible vessels, at the expense of the detail in the slice direction, as is the conventional method of recording SWI data. An initial set of high resolution protocols was used to scan Subjects 3-5 (age=26.7$\pm$1.2 years, male/female=1/2). Later, protocols incorporating a more isotropic resolution with a greater field of view (FOV) were chosen, to retain more detail in the vessels, in the slice direction. Subjects 6-10 (age=26.6$\pm$5.4 years, male/female=2/3) were scanned with the new protocol, as shown in Table 6.1. Veins were primarily imaged using SWI, but were also visualised using phase and QSM data, while arteries were imaged via time of flight methods.

Additionally, localised TOF volumes were acquired in the coronal orientation, across the visual cortex, with the same parameters as the first set of sequences. These were compared to the near full-brain volumes of the axial TOF, to assess the visibility of vessels propagating in different directions.

	PCA	TOF (Sub. 3-5)	TOF (Sub. 6-10)	SWI (Sub 3-5)	SWI (Sub. 6-10)	PSIR
FOV (mm)	230x170x30	200x178x86	200x178x90	200x178x86	200x178x100	224x224x157
resolution (mm)	0.6x0.6x0.6	0.3x0.3x0.6	0.5x0.5x0.5	0.3x0.3x1.2	0.5x0.5x1	0.7x0.7x0.7
TR/TE (ms)	19/10	21/3.5	21/3.5	25/16	25/16	6.3/2.6
FA	7	20	20	15	15	5
scan time (minutes)	3.2	10	7.5	10	7.5	6
chunks		9	9			
Flow direction	RL-AP-FH	FH				
velocity (cm/s)	5					

Table 6.1: Scanning parameters used for PCA, TOF and SWI investigations of Subjects 3-5 (set 1) and 6-10 (set 2).

6.2.2 Construction of Venograms, Arteriograms and Atlases

Processing of GE Data to Form Venous Maps and Atlas

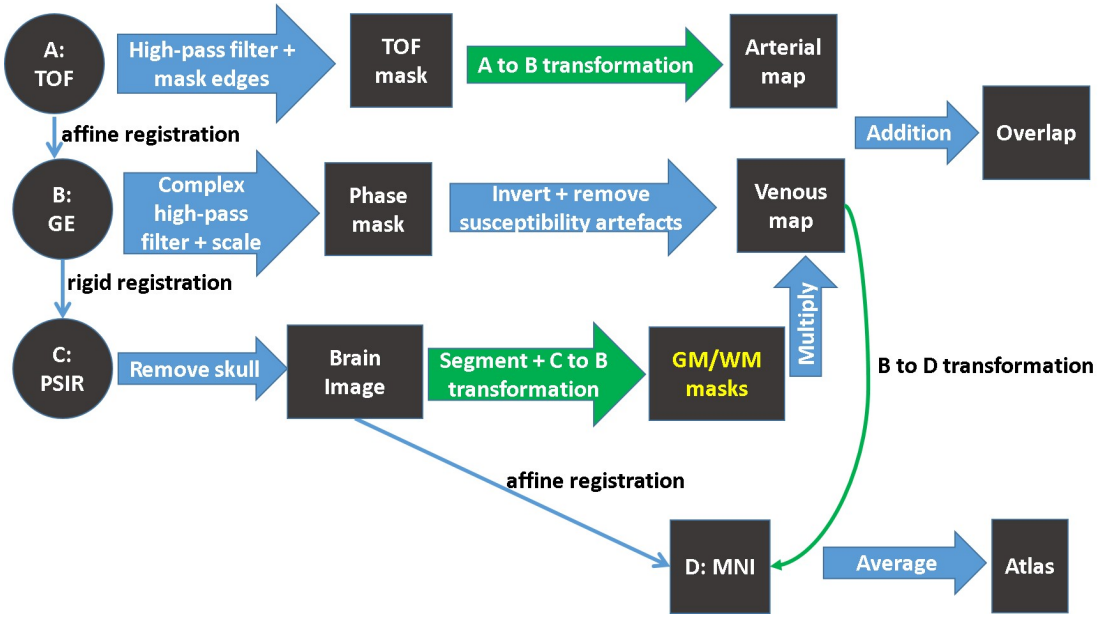

Figure 6.3: Work-flow diagram with processes used to generate arterial, venous and overlap maps for each subject, and a venous atlas averaged across subjects. Processed images are symbolised with grey boxes. Input data are represented with grey circles and include TOF, GE and PSIR. Green arrows are used to denote transformations and thin blue arrows are used for registrations. The "GM/WM masks" box is highlighted in yellow, which is further explained in Figure 6.4.

To segment the veins and create a venous map, initially the complex GE image was low-pass filtered by multiplying the complex image with a Gaussian filter, with full width at half maximum (FWHM) of 2mm, in Fourier space. The original complex image was then divided by the low-pass filtered data, resulting in a high-pass filtered phase dataset. The phase values between 0 and π were scaled between 1 and 0 and phase values less than 0 were set to a value of 1 to produce a phase mask for the SWI processing, as described in Chapter 2. SWI is classified as a dark blood image as the tissue is bright. The phase masks were inverted to produce a bright blood image of the veins, similar to TOF. This is illustrated in the middle flowchart in Figure 6.3. In order to assess the quality of the segmentation of the veins, a Frangi filter [25] was also applied to the magnitude images, to enhance the long thin dark vessel-like objects and compared with the inverted phase masks.

In the first step of improving the phase masks, the susceptibility artefacts from the sinuses were removed by manually masking around the base of the brain. To further improve the phase masks, the grey-white matter boundaries which appeared in the high-pass filtered images due to the sharp interface of the differing tissues, were removed by multiplying the phase mask with a combination of grey and white matter masks. Using the FMRIB Software Library (FSL- Oxford centre for Functional MRI of the Brain, University of Oxford), the brain was extracted from the PSIR data using the Brain

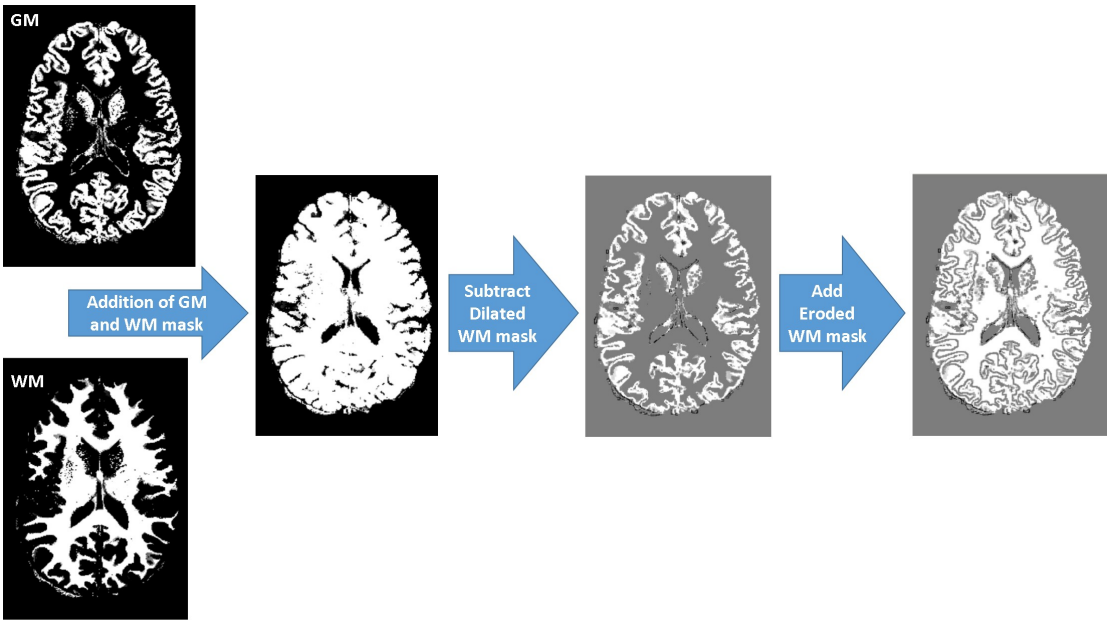

Figure 6.4: Combining of grey and white matter masks, to remove the artefacts from the grey-white matter boundaries, in the phase masks.

Extraction Tool (BET) [30] in FSL which was segmented to produce grey and white matter masks using FMRIB's Automated Segmentation Tool (FAST) [31] in FSL. The grey and white matter masks were added together to define the brain volume. Then the white matter mask was dilated and subtracted from the brain volume mask to define the outside edges of the grey-white matter boundary, and eroded and summed to define the inside edges of the grey-white matter boundary, as shown in Figure 6.4. This eliminated the region in which the grey-white matter edges were located.

After the removal of the susceptibility artefacts and grey-white matter boundaries, all of the venous maps were registered to the MNI (Montreal Neurological Institute) standard space, by initially registering the GE image data to the PSIR data using FMRIB's Linear Image Registration Tool (FLIRT) [32, 33] in FSL. The inverse transformation of the GE to PSIR registration was applied to the grey and white matter masks to transform into GE space, to reduce the grey-white matter boundaries, as described above. Secondly, the PSIR brain was registered to (0.3mm^3) MNI space. Thirdly, the GE to PSIR and the PSIR to MNI transformations were concatenated together and applied to the phase masks to transform into MNI space. The phase masks were then averaged together to produce a structural atlas, as shown in Figure 6.3.

Processing of TOF Data to Form Arterial Maps

To produce similar maps of the arteries, the TOF image data was high-pass filtered by multiplying with an inverted Gaussian kernel in Fourier space. The skull was masked manually to remove the sharp boundaries between the edge of the brain and the CSF. To transform the mask of the arteries to GE space, the TOF magnitude image was registered to the GE image using FLIRT and the resulting transformation was then applied

to the mask of the arteries. This produced an arterial map, as illustrated in the top flowchart in Figure 6.3.

Calculating Colour-coded Overlap Maps

The relative spatial distribution of veins and arteries was investigated by calculating the overlap of the venous and arterial maps. Masks of the venous and arterial maps were generated where the value of the venous and arterial voxels were set to 1 and 2, respectively. These masks were added together and in the resulting mask, the overlap had voxel values of 3. The overlap mask was displayed with a colour map to display the veins in blue, the arteries in red and the overlap in green. Figure 6.3 summarises the processing and registrations applied to the images to obtain the arterial, venous and overlap maps, and atlas.

6.2.3 QSM Oxygenation Distributions

For subject 7, a quantitative susceptibility map was calculated from the GE data using STI suite (Brain Imaging and Analysis Center, Duke University), by unwrapping the phase image, removing background sources of phase with the VSHARP filter and performing the inversion with the iLSQR technique, as described in Chapter 4. The QSM data was multiplied by the vein mask (thresholded venous map) to isolate the susceptibility values within the veins. The veins were separated by size, by eroding and then dilating the vein mask using a 1 voxel disk kernel, to leave the large vessels, and then subtracting this from the original vein mask to leave the small vessels. The susceptibility values of the two vessel types were compared, and a comparison was also made between vessels located within the grey and white matter regions. The susceptibility values within these groups were plotted as histograms and compared.

The radii of the vessels were determined by calculating the distance of each voxel within the mask to the nearest background (zero) voxel, as shown by the red numbers in Figure 6.5. The mask was then skeletonised to take the distance value through the centre of the vessels, which corresponded to the radii. The susceptibility values along the centre of the vessels were plotted against the radius of the vessels to compare susceptibility change across a range of vein radii.

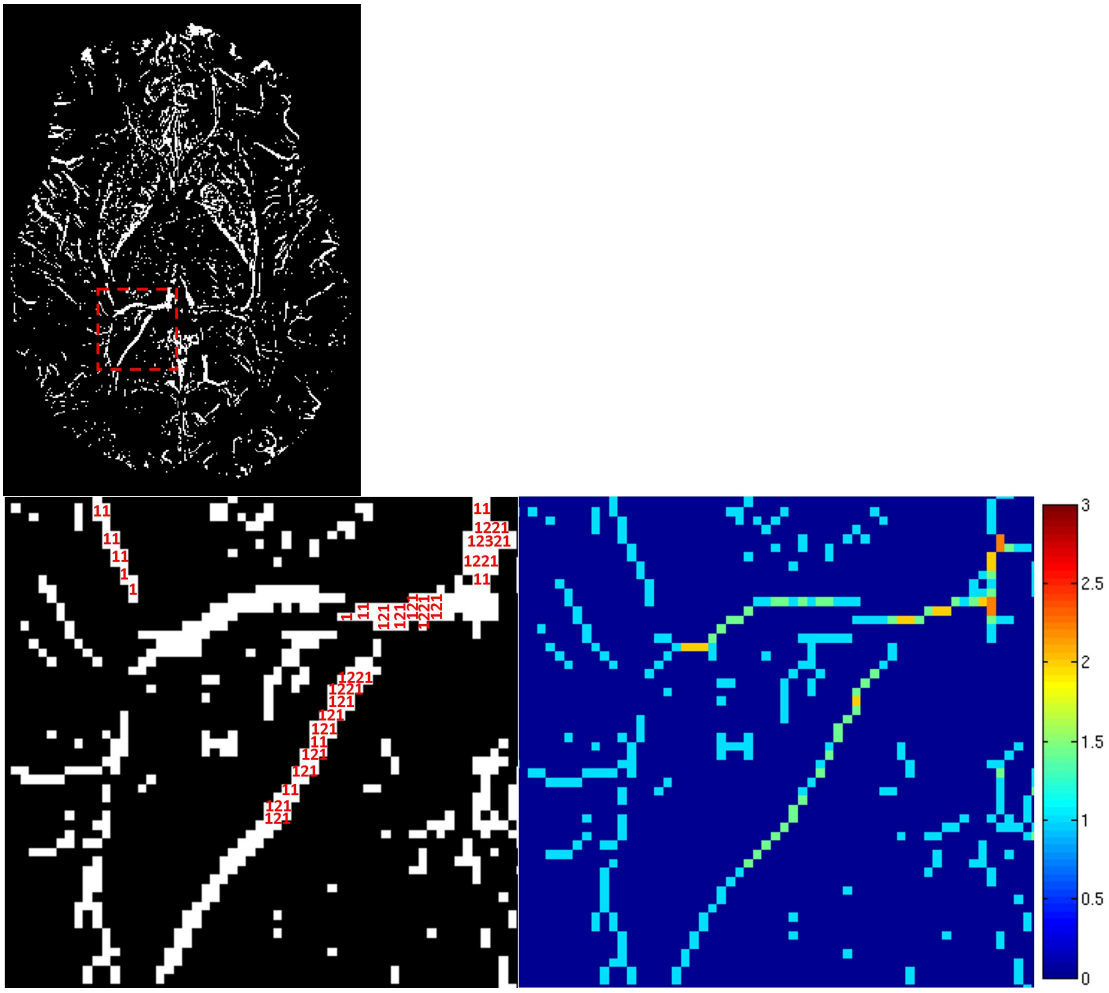

Figure 6.5: Top: vein mask with red box to indicate zoomed section. Bottom left to right: calculation of the distance of the voxels within the vessel to the background, illustrated with red numbers. The subsequent skeletonisation to extract the centre values, corresponding to the vessel radii.

6.3 Results and Discussion

Images from the different contrasts for vessel imaging are shown, followed by the segmentation of the veins from the phase data. The results produced by using the combination of techniques to eliminate artefacts and the effects of grey-white matter boundaries in the phase masks are presented. The veins are compared across all of the subjects and averaged to compare with the Ward atlas [24]. The overlap between the veins and arteries is compared across the subjects. The variation of the susceptibility values within the veins is assessed across vessels of varying radii and locations within the grey and white matter.

6.3.1 Optimising Contrast

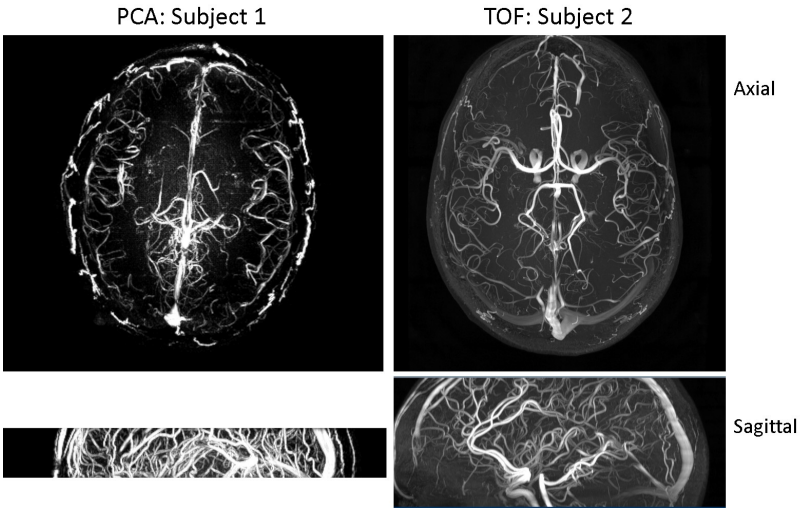

Figure 6.6: Axial and sagittal maximum intensity projects of PCA data for Subject 1(left) and TOF for Subject 2 (right).

Figure 6.6 shows optimised axial and sagittal maximum intensity projections (MIPs) of PCA and TOF images from Subjects 1 and 2, respectively. In both PCA and TOF images, the central vessels and the lateral vessels which travel through the imaging volume are clearly visible. In the TOF, more anterior and posterior vessels are visible compared to the PCA, possibly due to the larger field of view of the TOF.

In the sagittal MIPs, the angle of the vessels though the imaging volume are visible. The arteries are mostly in the vertical (head-foot) direction in the TOF as the contrast is generated by the flow of blood from the bottom to the top of the imaging volume, whilst the background tissue is suppressed. There are more visible vessels in the sagittal plane of the PCA as it was performed with flow measurement in 3 orthogonal directions.

Figure 6.7 shows axial and coronal MIP images from the TOF data taken coronally and axially. In the axial plane, the coronally acquired TOF contain more visible vessels running posteriorly, compared to the axially acquired TOF. In the coronal plane,

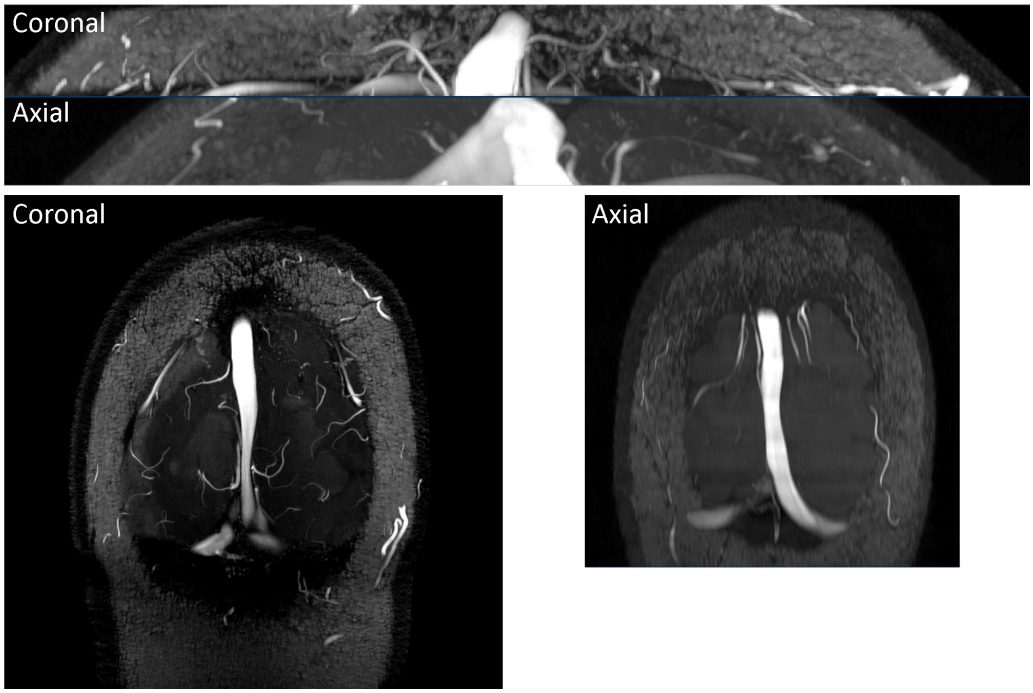

Figure 6.7: Axial and coronal MIP images from TOF scanned coronally and axially for Subject 3.

the coronally acquired TOF contains more laterally running vessels than the axially acquired TOF. In the axially acquired TOF, these vessels run parallel to the imaging plane and so are not visualised. Overall, these imaging sequences are sensitive to the orientation of the vessels and direction of flow, which requires scans along 3 orthogonal directions to image all of the vessels. However, the suppression of the signal from the subcutaneous fat is worse in the coronally acquired TOF images.

Figure 6.8 shows the SWI and phase data generated from the 3D gradient echo images. The maximum intensity projection (MIP) was calculated and shown across all of the following images to visualise the path of the veins through 6 slices. The SWI was used as the reference for the visualisation of the veins, to compare the vein segmentations against. Initially, the Frangi filter was applied to the magnitude images, but this produced thick, blurred objects around the ventricles, as shown in Figure 6.8. In contrast, the inverse phase mask appeared to segment the veins well, but is limited as it highlights the grey-white matter boundaries, boundaries of other iron rich regions and some edges of the brain. It is difficult to identify the real veins around the edge of the brain in the SWI data, as the veins appear dark so it is challenging to distinguish them from the surrounding CSF. An attempt was made to minimise the grey-white matter boundaries, as the Frangi filter was applied to the inverse phase mask which removed the grey-white matter boundaries, but also removed some of the small veins.

Figure 6.9 shows the grey and white matter masks extracted from the PSIR image, in blue and green, respectively. The combined grey and white matter mask is shown, which contains a grey band around the grey-white matter boundaries. A comparison of the phase mask multiplied by the combined grey-white matter mask is shown next to the

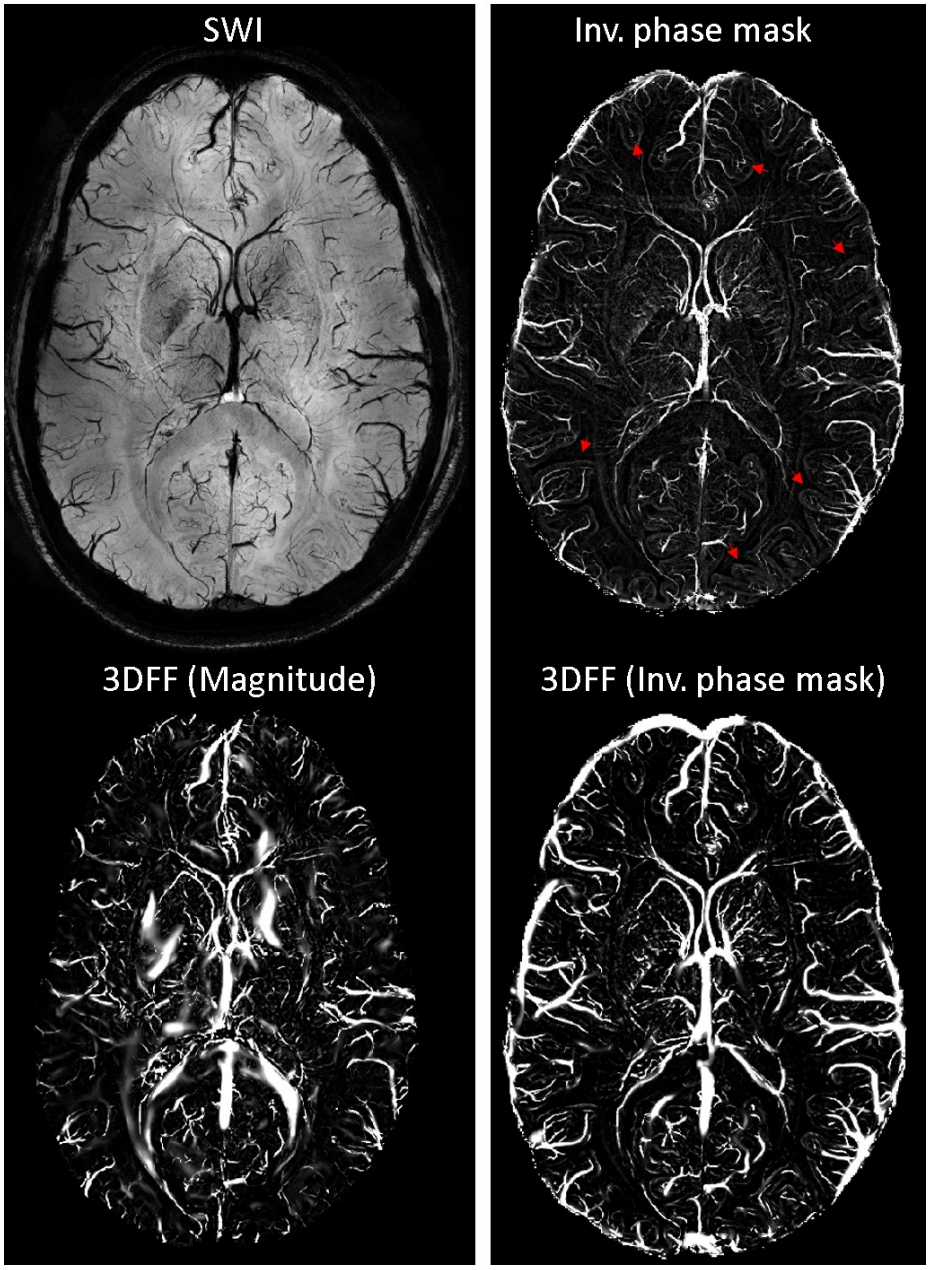

Figure 6.8: GE data from Subject 3 MIPed across 6 slices: Comparison of the visual prominence of the veins in the SWI data with the Frangi filtered (3DFF) magnitude data, and between the inverse phase mask and Frangi-filtered inverse phase mask.

original phase mask, showing the reduction in the artefacts from the grey-white matter boundaries with minimal removal of the veins. This worked well across the majority of slices, but overall, the success of this method depends mainly on the quality of the brain extraction and segmentation and to a lesser extent, on the quality of the registration.

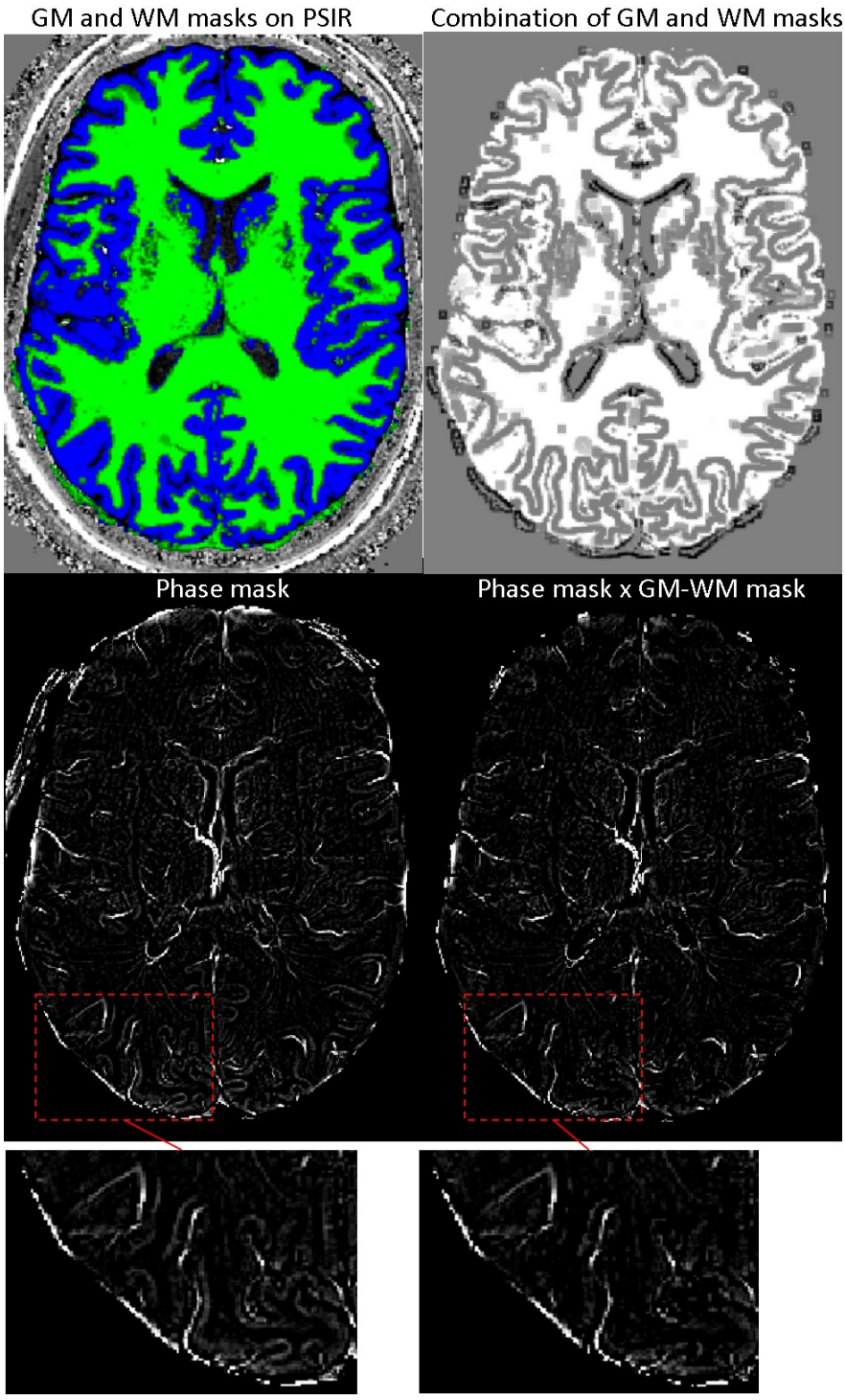

Figure 6.9: Subject 3: Top: grey (blue) and white (green) matter masks extracted from PSIR and combined grey-white matter mask. Bottom: original phase mask and resultant phase mask with grey-white matter boundary reduction, with zoomed sections.

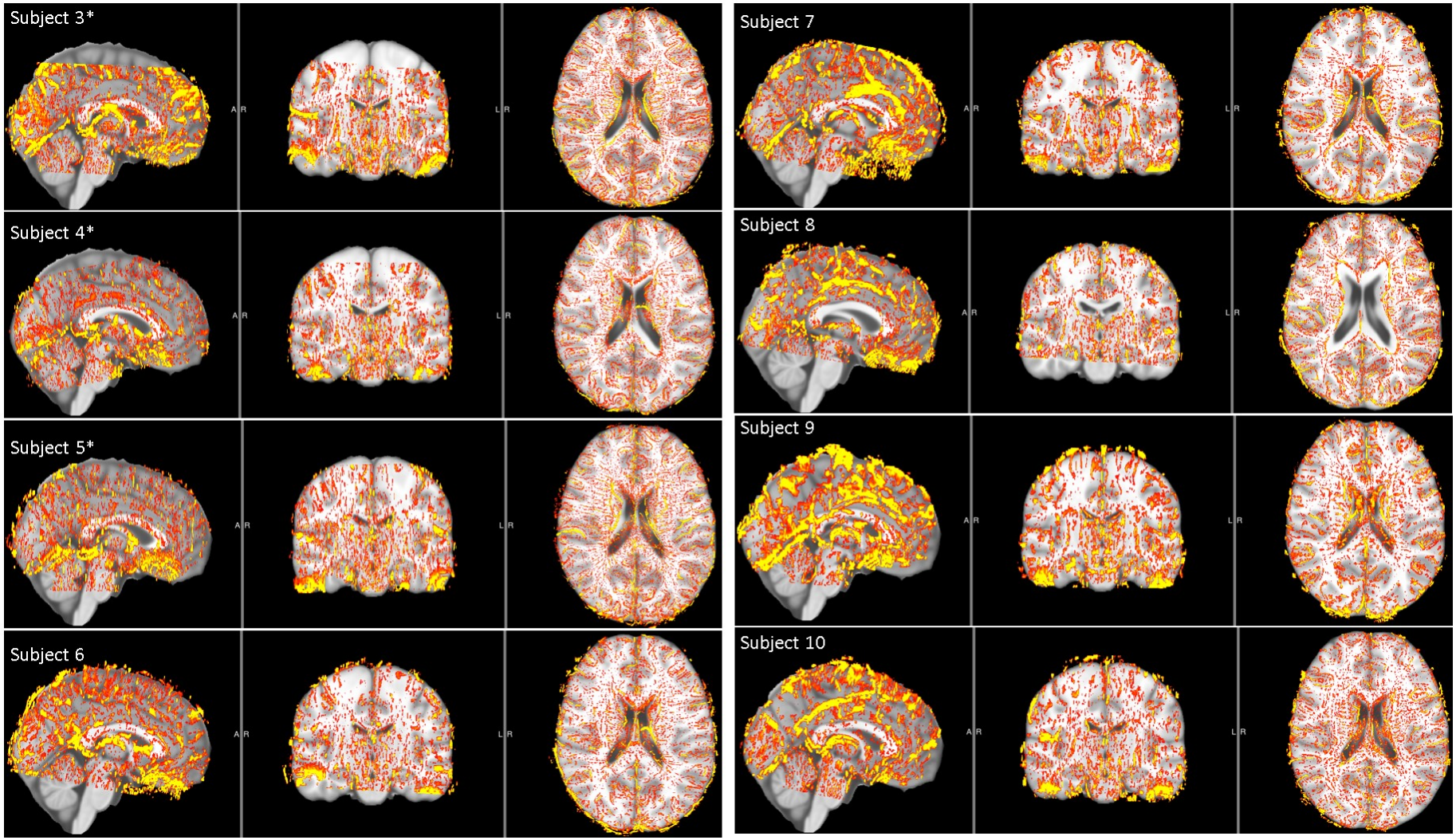

Figure 6.10: Registration of venous maps to MNI standard space for Subjects 3-10. *Performed with initial $0.3\times0.3\times1.2\text{mm}^3$ set of sequences.

6.3.2 Structural Venous Atlas

Figure 6.10 shows the venous maps for each subject registered to standard MNI space. In the sagittal orientation, the angulation and field of view of the imaging volume is evident. The distribution of the veins appears largely consistent between subjects for the large veins, but there is more variation in the distribution of smaller veins especially around the ventricles. In the sagittal plane, the thick veins running above and around the back of the corpus callosum are more visible, in Subjects 7-10 (Table 6.1, protocol 2). The veins in the axial images for Subjects 3-5 appear thinner and contain more detail due to the higher in-plane resolution (Table 6.1, protocol 1), but the projections of the veins in the z-direction are less continuous than in Subjects 6-10, due to the greater slice thickness.

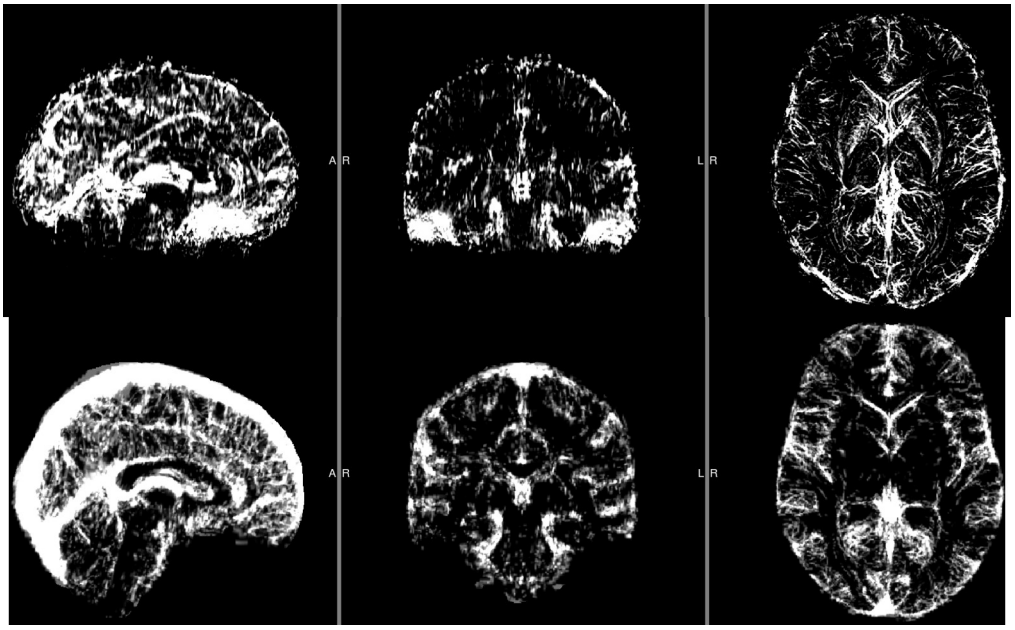

Figure 6.11: 8 subject (Subjects 3-10) averaged venous maps (top) and 10 subject averaged manual masks by Ward et al. [24] (bottom).

Figure 6.11 shows the venous maps averaged across the 8 subjects to produce a structural atlas. Also shown is a comparison with the 10 subject, manually-annotated vein mask atlas by Ward et al. [24]. The venous maps show greater detail within the deep grey matter regions such as the thalamus and globus pallidus, as the signal intensity is too low to segment these regions manually. However, the venous maps lack the sagittal sinus, due to its large flow and low signal intensity. The PSIR image was used to try to include the sagittal sinus in the brain mask. The BET and FAST tools were trialled on the PSIR images but the edges of the brain were segmented poorly. The PSIR could not be thresholded as the background intensity value was within the range of the tissue intensity values. Also the PSIR phase data could not be used to segment the sagittal sinus as there are wraps within the sagittal sinus.

The acquired GE images have different FOVs as the images for Subjects 3-5 did not cover the top of the brain and images acquired in all subjects did not cover the whole

of the cerebellum, compared to the Ward atlas in which whole brain coverage was achieved. The Ward vein atlas had a lower resolution of 0.5mm compared to the venous map atlas shown here, which had a resolution of 0.3mm to retain more detail, as contained in the higher resolution scans.

6.3.3 Overlap of Arterial and Venous Maps

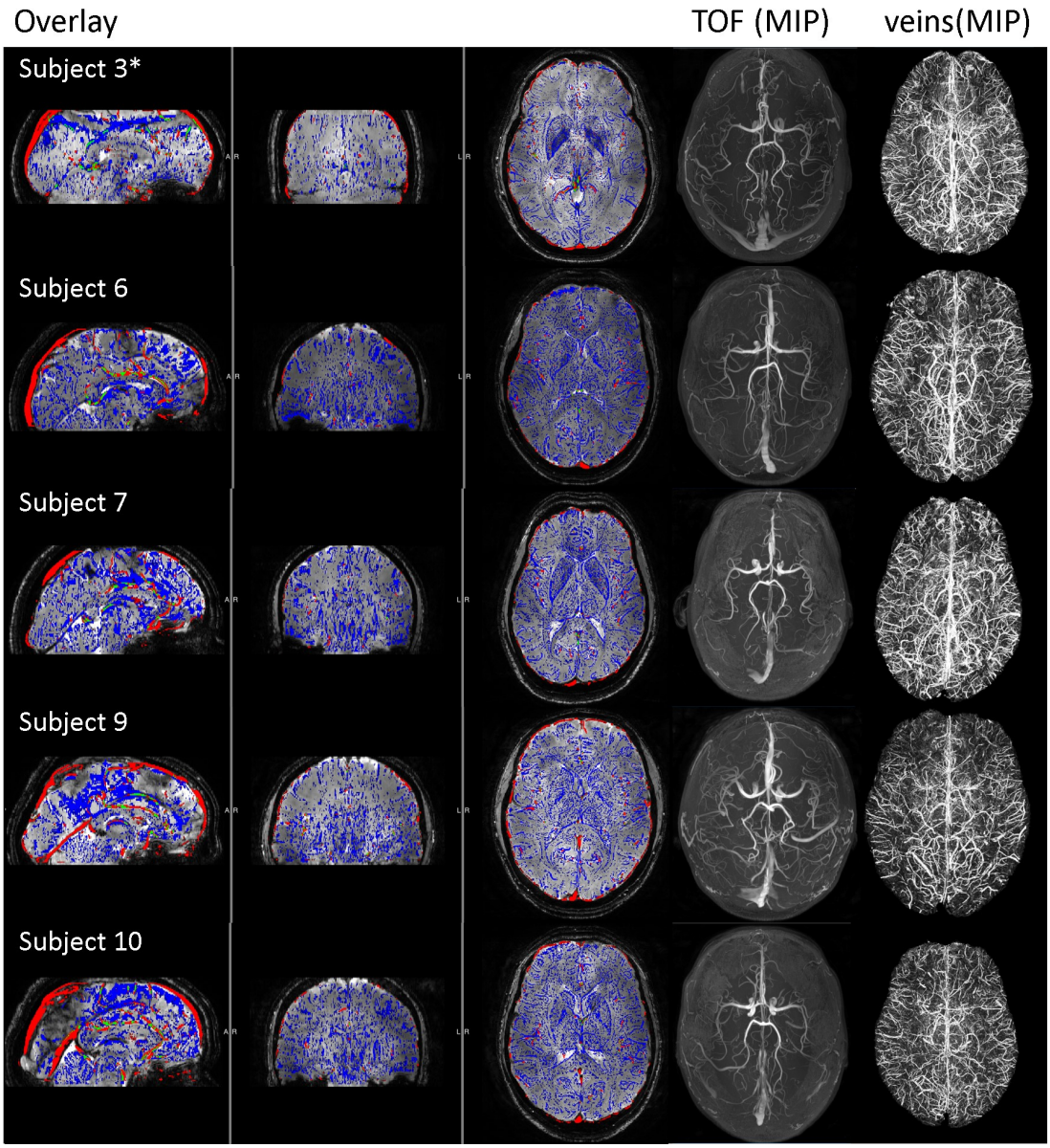

Figure 6.12: Left to right: overlays of arteries (red), veins (blue) and overlap (green) on GE image and MIP of TOFs and venous maps. *Performed with initial $0.3\times0.3\times1.2\text{mm}^3$ set of sequences.

For the 5 subjects (Subjects 3, 6, 7, 9 and 10) in which complete datasets were available, Figure 6.12 shows MIPs of venous maps and TOF images, along with overlays on the

GE images of venous, arterial and overlap maps, in blue, red and green respectively. There is low overlap between the venous and arterial maps of $\sim$6-8$\%$, but the sagittal sinus appears in the TOF images due to its large flow.

The circle of Willis is visible in all of the TOF MIPs. There is a similar semi-circular structure in the centre of the venous map MIPs, with extensions to the front and rear along the mid-line. There were slight differences in angulation between the subjects in the MIPs which changes the appearance of the circle of Willis. The angulation can be seen in the sagittal plane, which was corrected for by registering with MNI space.

The vessels clearly run to the edges of the brain in the venous map MIPs, but are not as evident in the TOF MIPs. Stepping through the slices, a few arteries do run towards the edge of the brain, mostly laterally. This may be due to the lower resolution of the TOF and the arteries decreasing in size towards the edges. TOF is also more sensitive to flow, so the lower flow of the small vessels will produce less signal and made them even less visible.

Upon evaluation of the artefacts in the TOF and vein maps, the appearance of the grey-white matter boundaries was minimal, as they would appear as slanted slabs around the edges of the brain. However, high-pass filtering of the TOF produced additional lines between the edge of brain and CSF. Automatic masking of the skull also proved to be difficult in the TOF, due to the low tissue signal intensities. Therefore, this was performed manually.

6.3.4 Venous Susceptibility Variation (Subject 7)

Figure 6.13 shows segmented susceptibility values of the veins produced by multiplying the QSM data by the vein mask. The susceptibility values range from -0.06 to 0.30ppm, corresponding to a minimum oxygenation fraction of 0.67, consistent with the 0.62 to 0.67 range measured by Fan et al. [14]. The negative susceptibility values are likely due to partial volume effects around the small, less deoxygenated veins.

Figure 6.14a shows histograms of the susceptibility values in all of the veins within the vein mask, divided into large and small veins. The average susceptibility values of all, large and small vein voxels was 0.04$\pm$0.05, 0.06$\pm$0.05 and 0.03$\pm$0.04ppm, respectively. The large veins had a higher peak susceptibility and a wider spread compared to the small veins. The histograms also show that the small veins represented a large portion of the voxels within the vein mask.

In Figure 6.14b, histograms of voxels within all veins and veins within the grey and white matter are shown. The average susceptibility values in the veins located across all of the brain, and grey and white matter are 0.04$\pm$0.05, 0.03$\pm$0.04 and 0.04$\pm$0.05pm, respectively. The grey matter has more voxels than the white matter (3120 compared to 2185, respectively) but the white matter has a higher average susceptibility, due to its larger spread and positive skew. In the normalised histograms (Figure 6.14c), the spread of the susceptibility values can be seen, as the peak of the grey matter histogram is narrower and has a higher modal susceptibility value compared to the white matter.

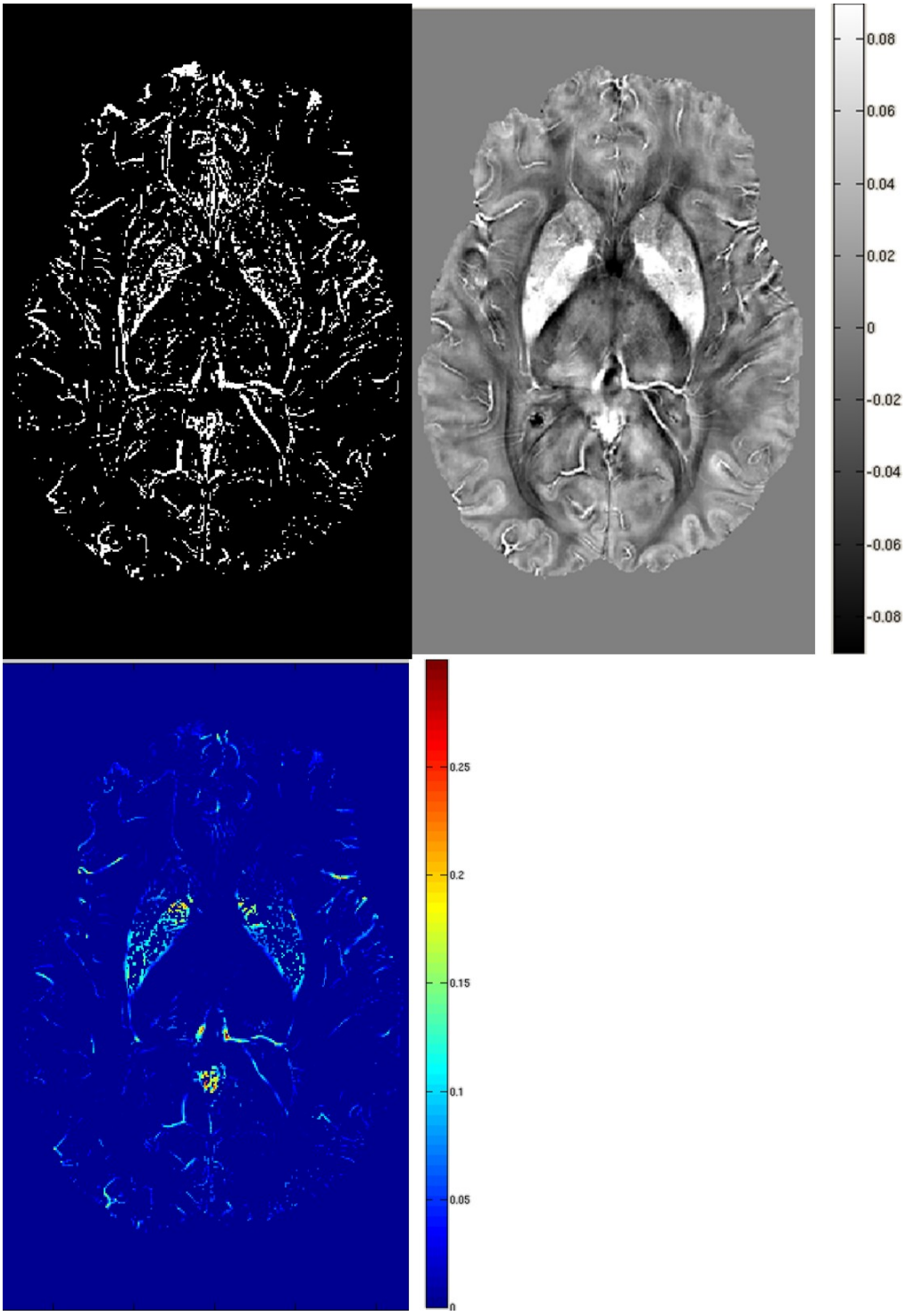

Figure 6.13: Vein mask, QSM and susceptibility values of veins from QSM multiplied by vein mask.

The grey and white matter data were split into large and small vessels and the normalised histograms were plotted, as shown in Figure 6.14d-e. The distribution of the susceptibility values of the small and large vessels in the grey matter are similar, with the large vessels being more positively skewed. This might be due to some continued

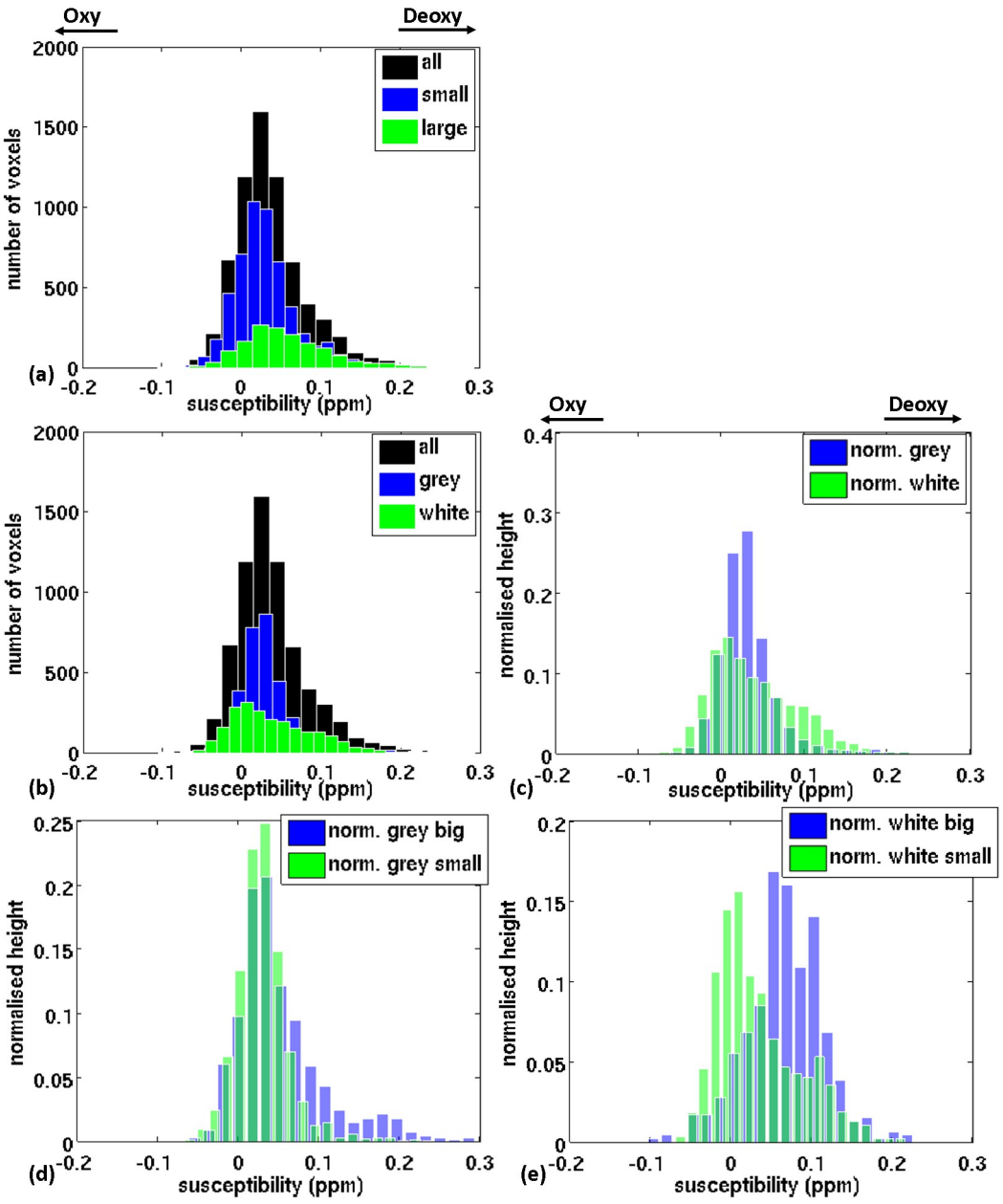

Figure 6.14: Histogram of susceptibility values in all, large and small veins. Histogram of voxels in all, grey and white matter. Corresponding normalised histogram of grey and white matter voxels. These groups are then slit into small and large vessels.

oxygen extraction from the veins as they merge together. On the other hand, the distribution of the susceptibility values of the large vessels in the white matter are shifted to higher susceptibility values compared to the small vessels, most likely due to the stronger partial volume effects for the small vessels in the white matter.

The susceptibility values of the large and small veins were split and plotted against vessel radii of 1 to 3 voxels, as shown in Figure 6.15a. The susceptibility values increased up to a radius of 2 voxels and then decreased. This is likely due to partial volume effects, especially on the edge of the less deoxygenated vessels for radii of less than 2

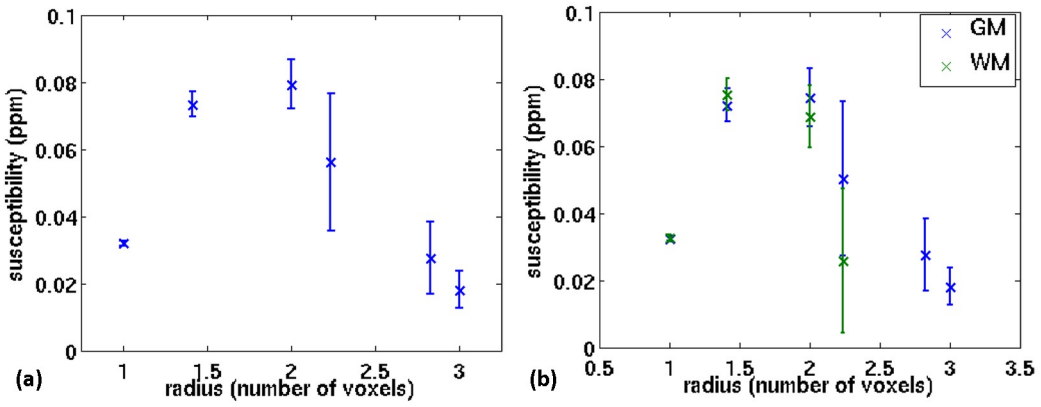

Figure 6.15: Plot of susceptibility values against vein radius. Plot of susceptibility values against vein radii in grey compared with white matter masks.

voxels. Additionally, the venous maps are less sensitive to the fast-flowing and less deoxygenated veins as they produce a smaller phase offset, and are less likely to be visualised in the venous map. For the vessels with radii greater than 2 voxels, small and fast-flowing veins join together with different oxygenation levels, averaging together, resulting in less deoxygenated blood, with lower susceptibility values. This might explain the large variation in the susceptibility values for veins with a radius of 2.2 voxels, as shown with error-bars of the standard error of the mean. The decrease in susceptibility values for vein radii of greater than 2 voxels was observed consistently across a range of subjects.

The susceptibility values against vessel radii were further separated by vessels within the grey and white matter masks and plotted, as shown in Figure 6.15b. The average radius of the veins in the grey and white matter were both 1.0 ± 0.2 voxels. The susceptibility values for grey matter veins were slightly lower than the white matter, for vessel radii of less than 2 voxels, but were higher for vessel radii of more than 2 voxels. The grey matter vessel radii also extended to a larger size. There were more vein mask voxels in the grey matter compared to the white matter (3120 compared to 2185).

Overall, there is a large spread in the susceptibility values of the veins, dependent on their size and location within the brain. The modal susceptibility value of the veins was higher in grey matter compared to white matter and were also higher in large veins compared to small veins. The large veins within the white matter had the highest modal susceptibility value as the largest vessels are located in the centre of the brain which is predominantly white matter. The small veins suffered from partial volume effects. Therefore this method is more suitable for the large veins.

6.4 Conclusion

TOF and GE imaging sequences were optimised to visualise the cerebral veins and arteries, with high spatial resolution at 7T. These were segmented by high-pass filtering of the phase and TOF data, to produce venous and arterial maps. The inverted phase mask method from the SWI analysis segmented the vessels better than the Frangi filter. The artefacts in the phase masks from the grey-white matter boundaries were largely removed and the venous maps were registered to standard space. This process was largely limited by the poor quality of the brain extraction using BET.

A venous atlas was produced and contained greater detail within the deep grey matter structures, but had a smaller FOV compared to the manually segmented Ward atlas [24]. The venous and arterial maps were found to only overlap by a small fraction. The sagittal sinus was challenging to segment due to its low signal intensity and proximity to the CSF.

The oxygenation of the venous blood was inferred from the susceptibility values within the vein mask. The calculated minimum oxygen fraction was consistent with the range of values reported in the literature. The susceptibility values of large veins and those within the grey matter were higher than values in small veins and those within the white matter. However, these susceptibility values contained a great degree of variation, as shown by the large error-bars and standard deviations. Finally, the susceptibility value of the veins were observed to vary with vessel radius and increased up to a radius of 2 voxels and then decreased.

For future work, the masking and brain extraction could be improved to be more inclusive of the sagittal sinus in the venous maps. The BET tool was not appropriate for the masking of the sagittal sinus so alternative methods would be investigated. The venous and arterial maps could be extended by increasing the FOV to cover the cerebellum.

Bibliography

[1] George Jed Siegel. *Basic neurochemistry: molecular, cellular and medical aspects*. Number V360 SIEb. 1999.

[2] Alifia Tameem and Hari Krovvidi. Cerebral physiology. *Continuing Education in Anaesthesia Critical Care & Pain*, 13(4):113–118, 2013.

[3] Helena C Chui, JI Victoroff, D Margolin, W Jagust, R Shankle, and R Katzman. Criteria for the diagnosis of ischemic vascular dementia proposed by the state of California Alzheimer's disease diagnostic and treatment centers. *Neurology*, 42(3):473–473, 1992.

[4] Miguel D'haeseleer, Melissa Cambron, Ludo Vanopdenbosch, and Jacques De Keyser. Vascular aspects of Multiple Sclerosis. *The Lancet Neurology*, 10(7):657–666, 2011.

[5] I Leng Tan, Ronald A van Schijndel, Petra JW Pouwels, Marianne AA van Walderveen, Juergen R Reichenbach, Radu A Manoliu, and Frederik Barkhof. MR venography of Multiple Sclerosis. *American Journal of Neuroradiology*, 21(6):1039–1042, 2000.

[6] Diego San Millán Ruíz, Hasan Yilmaz, and Philippe Gailloud. Cerebral developmental venous anomalies: current concepts. *Annals of Neurology*, 66(3):271–283, 2009.

[7] Dorota Kozinska, Christopher M Holland, Karl Krissian, Carl-Fredrik Westin, and Charles RG Guttmann. A method for the analysis of the geometrical relationship between white matter pathology and the vascular architecture of the brain. *Neuroimage*, 22(4):1671–1678, 2004.

[8] Günther Grabner, Thomas Haider, Mark Glassner, Alexander Rauscher, Hannes Traxler, Siegfried Trattnig, and Simon D Robinson. Post mortem validation of MRI-identified veins on the surface of the cerebral cortex as potential landmarks for neurosurgery. *Frontiers in Neuroscience*, 11:355, 2017.

[9] Seiji Ogawa, Tso-Ming Lee, Alan R Kay, and David W Tank. Brain magnetic resonance imaging with contrast dependent on blood oxygenation. *Proceedings of the National Academy of Sciences*, 87(24):9868–9872, 1990.

[10] E Mark Haacke, Yingbiao Xu, Yu-Chung N Cheng, and Jürgen R Reichenbach. Susceptibility weighted imaging (SWI). *Magnetic Resonance in Medicine*, 52(3):612–618, 2004.

[11] Sam Wharton, Andreas Schäfer, and Richard Bowtell. Susceptibility mapping in the human brain using threshold-based k-space division. *Magnetic Resonance in Medicine*, 63(5):1292–1304, 2010.

[12] David Saloner. The AAPM/RSNA physics tutorial for residents. An introduction to MR angiography. *Radiographics*, 15(2):453–465, 1995.

[13] Jurgen R Reichenbach, Ramesh Venkatesan, Douglas J Schillinger, Daniel K Kido, and E Mark Haacke. Small vessels in the human brain: MR venography with deoxyhemoglobin as an intrinsic contrast agent. *Radiology*, 204(1):272–277, 1997.

[14] Audrey P Fan, Berkin Bilgic, Louis Gagnon, Thomas Witzel, Himanshu Bhat, Bruce R Rosen, and Elfar Adalsteinsson. Quantitative oxygenation venography from MRI phase. *Magnetic Resonance in Medicine*, 72(1):149–159, 2014.

[15] Cornelius von Morze, Duan Xu, Derk D Purcell, Christopher P Hess, Pratik Mukherjee, David Saloner, Douglas AC Kelley, and Daniel B Vigneron. Intracranial time-of-flight MR angiography at 7T with comparison to 3T. *Journal of Magnetic Resonance Imaging*, 26(4):900–904, 2007.

[16] Wieslaw L Nowinski, Fiftarina Puspitasaari, Ihar Volkau, Yevgen Marchenko, and Michael V Knopp. Comparison of magnetic resonance angiography scans on 1.5, 3, and 7 tesla units: A quantitative study of 3-dimensional cerebrovasculature. *Journal of Neuroimaging*, 23(1):86–95, 2013.

[17] María A Fernández-Seara, Aranee Techawiboonwong, John A Detre, and Felix W Wehrli. MR susceptometry for measuring global brain oxygen extraction. *Magnetic Resonance in Medicine*, 55(5):967–973, 2006.

[18] Audrey P Fan, Thomas Benner, Divya S Bolar, Bruce R Rosen, and Elfar Adalsteinsson. Phase-based regional oxygen metabolism (prom) using MRI. *Magnetic Resonance in Medicine*, 67(3):669–678, 2012.

[19] Michael C Langham, Jeremy F Magland, Charles L Epstein, Thomas F Floyd, and Felix W Wehrli. Accuracy and precision of MR blood oximetry based on the long paramagnetic cylinder approximation of large vessels. *Magnetic Resonance in Medicine*, 62(2):333–340, 2009.

[20] AC Guyton and JE Hall. Red blood cells, anemia, and polycythemia. *Textbook of Medical Physiology*, 11:419–428, 1996.

[21] Varsha Jain, Michael C Langham, and Felix W Wehrli. MRI estimation of global brain oxygen consumption rate. *Journal of Cerebral Blood Flow & Metabolism*, 30(9):1598–1607, 2010.

[22] Robert M Weisskoff and Suzanne Kiihne. MRI susceptometry: Image-based measurement of absolute susceptibility of MR contrast agents and human blood. *Magnetic Resonance in Medicine*, 24(2):375–383, 1992.

[23] Naoya Hattori, Marvin Bergsneider, Hsiao-Ming Wu, Thomas C Glenn, Paul M Vespa, David A Hovda, Michael E Phelps, and Sung-Cheng Huang. Accuracy of a method using short inhalation of 15o-o2 for measuring cerebral oxygen extraction fraction with pet in healthy humans. *Journal of Nuclear Medicine*, 45(5):765–770, 2004.

[24] Phillip GD Ward, Nicholas J Ferris, Parnesh Raniga, David L Dowe, Amanda CL Ng, David G Barnes, and Gary F Egan. Combining images and anatomical knowledge to improve automated vein segmentation in MRI. *NeuroImage*, 165:294–305, 2018.

[25] Alejandro F Frangi, Wiro J Niessen, Koen L Vincken, and Max A Viergever. Multiscale vessel enhancement filtering. In *International Conference on Medical Image Computing and Computer-Assisted Intervention*, pages 130–137. Springer, 1998.

[26] Nicolas Vigneau-Roy, Michael Bernier, Maxime Descoteaux, and Kevin Whittingstall. Regional variations in vascular density correlate with resting-state and task-evoked blood oxygen level-dependent signal amplitude. *Human Brain Mapping*, 35(5):1906–1920, 2014.

[27] Günther Grabner, Assunta Dal-Bianco, Simon Hametner, Hans Lassmann, and Siegfried Trattnig. Group specific vein-atlasing: An application for analyzing the venous system under normal and multiple sclerosis conditions. *Journal of Magnetic Resonance Imaging*, 40(3):655–661, 2014.

[28] Marek Kociński, Andrzej Materka, Andreas Deistung, Jürgen Reichenbach, and Arvid Lundervold. Towards multi-scale personalized modeling of brain vasculature based on magnetic resonance image processing. In *Systems, Signals and Image Processing (IWSSIP), 2017 International Conference on*, pages 1–5. IEEE, 2017.

[29] Chih-Yang Hsu, Ben Schneller, Ali Alaraj, Michael Flannery, Xiaohong Joe Zhou, and Andreas Linninger. Automatic recognition of subject-specific cerebrovascular trees. *Magnetic Resonance in Medicine*, 77(1):398–410, 2017.

[30] Stephen M Smith. Fast robust automated brain extraction. *Human Brain Mapping*, 17(3):143–155, 2002.

[31] Yongyue Zhang, Michael Brady, and Stephen Smith. Segmentation of brain MR images through a hidden markov random field model and the expectation-maximization algorithm. *IEEE Transactions on Medical Imaging*, 20(1):45–57, 2001.

[32] Mark Jenkinson and Stephen Smith. A global optimisation method for robust affine registration of brain images. *Medical Image Analysis*, 5(2):143–156, 2001.

[33] Mark Jenkinson, Peter Bannister, Michael Brady, and Stephen Smith. Improved optimization for the robust and accurate linear registration and motion correction of brain images. *Neuroimage*, 17(2):825–841, 2002.

Chapter 7

Conclusion

7.1 Summary of Results

In this thesis, the effects of susceptibility on imaging were explored and exploited to provide additional contrast and quantitative information. Susceptibility values were measured from simulated and ferritin-doped agar cylinders, from post-mortem brain tissue and from in vivo cerebral blood vessels. Susceptibility was also used to enhance the delineation of the nuclei within the thalamus.

Simulations

The simulated phase from different arrangements of dipoles and a cylindrical perturber oriented perpendicular to the field, were investigated. The observed behaviour for a single dipole was as expected, as R_2* and the rate of change of the phase with TE, both increased linearly with the volume fraction, as predicted by the Yablonskiy analytical solution [1]. The gradients of these were approximately an order of magnitude larger for six dipoles compared to a single dipole. For the different arrangement of dipoles, the slope of the logarithm of the magnitude and the slope of the phase were approximately constant for dipoles randomly placed in the volume and was similar for dipoles randomly placed in the x-y plane. Both the slope of the logarithm of the magnitude and the slope of the phase increased, as the dipoles were restricted to a line parallel to the z axis and decreased for dipoles restricted to a line in the x-y plane, due to the overlap of the dipolar fields. For diffusion simulated around a single spherical perturber in a spherical volume, the logarithm of the signal magnitude agreed well with the Sukstanskii analytical solution [2], for both the short and long time limits. The simulated data from a cylinder oriented perpendicular to the applied magnetic field was used to test the fitting to the difference in phase between the inside and outside of the cylinder. This analysis was then applied to the ferritin phantom datasets, which showed that the susceptibility values of the ferritin-doped agar cylinders increased with the concentration of ferritin and correlated well between 3T and 7T measurements. The gradient of the 3T measurements was higher, suggesting that the samples had deteriorated slightly between the scanning sessions.

Post-mortem

A circulator was designed, built and tested to enable temperature-dependent scanning. The efficiency of the circulator was restricted by the rate of heat transfer to the centre of the sample which depended on the properties of the sample itself. It was noted that temperature gradients needed to be considered during temperature-controlled scanning. The effect of temperature on the MR parameters of a ferritin phantom and post-mortem brain were investigated. The magnetic susceptibility of the agar cylinder with the largest ferritin concentration was 12% higher at 5°C compared to 32°C. The R_1 and R_2* values changed much more significantly over this temperature range as R_2* increased and R_1 decreased. For the post-mortem tissue, the R_1, R_2* and susceptibility values all decreased with increasing temperature, due to the reduction in the susceptibility of iron dominating the effect from the increased diffusion of water. However, the post-mortem tissue seemed to have a lower susceptibility but longer R_1 and R_2* values. This could be due to agar having a more homogeneous consistency than brain tissue. The associated errors were larger due to temperature variations, and the low resolution of the data made it harder to identify the edges of each brain region. The effect of fixation and handling on post-mortem tissue was also investigated. During the longitudinal fixation of the post-mortem brain, the volume decreased by 2.9 ± 1.6 cm^3/month. R_2* initially increased in some regions but overall decreased. The susceptibility followed a similar trend. R_1 values increased overall and appeared to level off, towards the end of the fixation period. R_1 decreased sharply in a few regions, as the fixation front diffused though the tissue. Therefore, the temporal variation of the R_1 values was dependent on the distance from the edge of the tissue. Overall, broad comparisons of post-mortem MRI values with in vivo imaging are possible as long as the fixation time, temperature and other parameters are carefully considered.

Thalamus

The thalamic nuclei were identified in the histology and corresponding post-mortem MRI data by referencing to the Morel atlas [3]. This was verified with the use of k-means clustering, Canny edge detection and hierarchical clustering [4, 5, 6]. Groups of nuclei were consistently observed across the brains with different ages and conditions. The nuclei were delineated in the post-mortem MRI data with manual annotations with a high level of confidence by comparing the FLASH, QSM and FSE images. The contrast and signal to noise ratios of the post-mortem images were better than the optimised in vivo scans, due to the presence of blood flow and head movement in the in vivo data. The nuclei in the in vivo MRI data were also delineated manually with almost the same confidence as the post-mortem data. The outlines matched well with the hierarchical clusters, but the clustering on the in vivo data was relatively less well defined than for the post-mortem data. Hierarchical clustering with spatial information and multiple contrasts produced the best groupings.

Cerebral Vessels

A range of imaging sequences, including TOF and GE, were optimised to visualise the cerebral veins and arteries. These were segmented by high-pass filtering of the

phase and TOF data, to produce venous and arterial maps, respectively. The inverted phase masks from the SWI analysis allowed better segmentation than data that had been Frangi filtered. The artefacts in the phase masks from the grey-white matter boundaries were largely removed and the venous maps were registered to standard space. This process was largely limited by the poor quality of the brain extraction using the brain extraction tool in FSL. The sagittal sinus was challenging to segment due to its low signal intensity and proximity to the CSF. The venous and arterial maps were found to only overlap by a small fraction. A venous atlas was produced and contained greater detail within the deep grey matter structures, but had a smaller FOV compared to the manually-segmented Ward atlas [7]. Subsequently, the susceptibility values within the vein mask were used to infer the oxygenation of the venous blood. The calculated minimum oxygen fraction of 0.67 was consistent with the range of values reported in the literature [8]. The susceptibility values of large veins and those within the grey matter were higher than small veins and those within the white matter. However, these susceptibility values contained a great degree of variation. Finally, the susceptibility value of the veins were observed to vary with vessel radius, increasing up to a radius of 2 voxels (1mm) and then decreased.

7.2 Future Work

Simulations

Susceptibility maps provide information about chemical and physical composition from a combination of different components, such as iron and myelin. The iron distribution from Perls' stain data of post-mortem tissue could be used to model field perturbations, to simulate the expected MR signal and produce quantitative susceptibility maps. The QSM images could be compared between simulated and experimental MRI data. This could also be used to test different QSM algorithms and to determine fitting parameters to correlate susceptibility values to iron concentrations.

Post-mortem

The motivation for this project calls for the investigation and verification of the effects of fixation on the distribution of iron. This could be carried out for whole and sectioned brains biochemically which would then be correlated with MR measurements. For the longitudinal fixation study, scanning could be repeated more often during the first 6 months and samples could be taken from the other brain half, of cortical and deep grey and white matter. This would allow a comparison of the MR susceptibility values to a physical measurement of iron concentration, using inductively-coupled mass spectrometry (ICPMS). Fixed tissue could also be compared to fresh frozen tissue from another brain, by dividing, sectioning one half and following a similar scanning protocol as above. The other half would then be frozen for ICPMS analysis. In this way, a comparison of iron distribution could be made with fixation time, between fresh and frozen tissue and would allow comparison of MR imaging with histology and spectroscopy.

For the temperature dependent project, more time to equilibrate and more temperature probes could be used to measure the temperature of the tissue to obtain a better homogeneity. The measurements could be repeated during cooling to measure lag in the temperature change and if there is any hysteresis. The temperature could also be verified by using MR thermometry.

Thalamus

The quality of the in vivo images could be improved by reducing noise from movement and to further optimise the sequences to increase contrast. The post-mortem images could be used to create a thalamic atlas from the 5 post-mortem brain data. Additionally, a preliminary 3D map could be generated from the 7 histological sections to compare with the MR data to investigate the origins of the contrast in the thalamus. Finally, the halamic outlines could be used to correlate the anatomical structure with areas of activation in the thalamus, from fMRI measurements.

Cerebral Vessels

The masking and brain extraction could be improved to be more inclusive of the sagittal sinus in the venous maps. The brain extraction tool was not appropriate for the masking of the sagittal sinus so alternative methods would be investigated. The venous and arterial maps could be extended by increasing the FOV to cover the cerebellum. Additionally, vessel density maps could be calculated to quantify differences in vessel distributions between subjects or disease states.

Bibliography

[1] Dmitriy A Yablonskiy and E Mark Haacke. Theory of NMR signal behavior in magnetically inhomogeneous tissues: the static dephasing regime. *Magnetic Resonance in Medicine*, 32(6):749–763, 1994.

[2] Alexander L Sukstanskii and Dmitriy A Yablonskiy. Gaussian approximation in the theory of MR signal formation in the presence of structure-specific magnetic field inhomogeneities. effects of impermeable susceptibility inclusions. *Journal of Magnetic Resonance*, 167(1):56–67, 2004.

[3] Anne Morel, Michel Magnin, Daniel Jeanmonod, et al. Multiarchitectonic and stereotactic atlas of the human thalamus. *Journal of Comparative Neurology*, 387(4):588–630, 1997.

[4] John Canny. A computational approach to edge detection. In *Readings in Computer Vision*, pages 184–203. Elsevier, 1987.

[5] James MacQueen et al. Some methods for classification and analysis of multivariate observations. In *Proceedings of the Fifth Berkeley Symposium on Mathematical Statistics and Probability*, volume 1, pages 281–297. Oakland, CA, USA, 1967.

[6] Daniel Defays. An efficient algorithm for a complete link method. *The Computer Journal*, 20(4):364–366, 1977.

[7] Phillip GD Ward, Nicholas J Ferris, Parnesh Raniga, David L Dowe, Amanda CL Ng, David G Barnes, and Gary F Egan. Combining images and anatomical knowledge to improve automated vein segmentation in MRI. *NeuroImage*, 165:294–305, 2018.

[8] Audrey P Fan, Berkin Bilgic, Louis Gagnon, Thomas Witzel, Himanshu Bhat, Bruce R Rosen, and Elfar Adalsteinsson. Quantitative oxygenation venography from MRI phase. *Magnetic Resonance in Medicine*, 72(1):149–159, 2014.